

Next Generation Multifunctional Composites for Impact, Vibration and Electromagnetic Radiation Hazard Mitigation

Mehran Tehrani

Dissertation submitted to the faculty of the
Virginia Polytechnic Institute and State University
in partial fulfillment of the requirements for the degree of

Doctor of Philosophy

in

Engineering Mechanics

Marwan S. Al-Haik, Chair

Scott W. Case

Muhammad R. Hajj

Sunghwan Jung

Shane D. Ross

October 29, 2012

Blacksburg, Virginia

Keywords: multiscale composites, carbon nanotubes, mechanical characterization, finite element modeling, electromagnetic interference shielding

Copyright © 2012, Mehran Tehrani

Next Generation Multifunctional Composites for Impact, Vibration and Electromagnetic Radiation Hazard Mitigation

Mehran Tehrani

(ABSTRACT)

For many decades, fiber reinforced polymers (FRPs) have been extensively utilized in load-bearing structures. Their formability and superior in-plane mechanical properties have made them a viable replacement for conventional structural materials. A major drawback to FRPs is their weak interlaminar properties (e.g., interlaminar fracture toughness). The need for lightweight multifunctional structures has become vital for many applications and hence alleviating the out-of-plane mechanical (i.e., quasi-static, vibration, and impact) and electrical properties of FRPs while retaining minimal weight is the subject of many ongoing studies. The primary objective of this dissertation is to investigate the fundamental processes for developing hybrid, multifunctional composites based on surface grown carbon nanotubes (CNTs) on carbon fibers' yarns. This study embraces the development of a novel low temperature synthesis technique to grow CNTs on virtually any substrate. The developed method—graphitic structures by design (GSD)—offers the opportunity to place CNTs in advantageous areas of the composite (e.g., at the ply interface) where conventional fiber architectures are inadequate. The relatively low temperature of the GSD (i.e. 550 °C) suppresses the undesired damage to the substrate fibers. GSD carries the advantage of growing uniform and almost aligned CNTs at pre-designated locations and thus eliminates the agglomeration and dispersion problems associated with incorporating CNTs in polymeric composites. The temperature regime utilized in GSD is less

than those utilized by other synthesis techniques such as catalytic chemical vapor deposition (CCVD) where growing CNTs requires temperature not less than 700 °C.

It is of great importance to comprehend the reasons for and against using the methods involving mixing of the CNTs directly with the polymer matrix, to either fabricate nanocomposites or three-phase FRPs. Hence, chapter 2 is devoted to the characterization of CNTs-epoxy nanocomposites at different thermo-mechanical environments via the nanoindentation technique. Improvements in hardness and stiffness of the CNTs-reinforced epoxy are reported. Long duration (45 mins) nano creep tests were conducted to study the viscoelastic behavior of the CNT-nanocomposites. Finally, the energy absorption of these nanocomposites is measured via novel nanoimpact testing module.

Chapter 3 elucidates a study on the fabrication and characterization of a three phase CNT-epoxy system reinforced with woven carbon fibers. Tensile test, high velocity impact ($\sim 100 \text{ ms}^{-1}$), and dynamic mechanical analysis (DMA) were employed to examine the response of the hybrid composite and compare it with the reference CFRP with no CNTs. Quasi-static shear punch tests (QSSPTs) were also performed to determine the toughening and damage mechanisms of both the CNTs-modified and the reference CFRP composites during transverse impact loading.

The synthesis of CNTs at 550 °C via GSD is the focus of chapter 4. The GSD technique was adjusted to grow Palladium-catalyzed carbon filaments over carbon fibers. However, these filaments were revealed to be amorphous (turbostratic) carbon. Plasma sputtering was utilized to sputter nickel nano-films on the surface of the substrate carbon fibers. These films were later fragmented into nano-sized nickel islands from which CNTs were grown utilizing the GSD

technique. The structure and morphology of the CNTs are evaluated and compared to CNTs grown via catalytic chemical vapor deposition (CCVD) over the same carbon fibers.

Chapter 5 embodies the mechanical characterization of composites based on carbon fibers with various surface treatments including, but not limited to, surface grown CNTs. Fibers with and without sizing were subjected to different treatments such as heat treatment similar to those encountered during the GSD process, growing CNTs on fabrics via GSD and CCVD techniques, sputtering of the fibers with a thin thermal shield film of SiO₂ prior to CNT growth, selective growth of CNTs following checkerboard patterns, etc.

The effects of the various surface treatments (at the ply interfaces) on the on-axis and off-axis tensile properties of the corresponding composites are discussed in this chapter. In addition, the DMA and impact resistance of the hybrid CNT-CFRP composites are measured and compared to the values obtained for the reference CFRP samples. While the GSD grown CNTs accounted for only 0.05 wt% of the composites, the results of this chapter contrasts the advantages of the GSD technique over other methods that incorporate CNTs into a CFRP (i.e. direct growth via CCVD and mixing of CNTs with the matrix).

Understanding the behavior of the thin CFRPs under impact loadings and the ability to model their response under ballistic impact is essential for designing CFRP structures. A precise simulation of impact phenomenon should account for progressive damage and strain rate dependent behavior of the CFRPs. In chapter 6, a novel procedure to calibrate the state-of-the-art MAT162 material model of the LS-DYNA finite element simulation package is proposed. Quasi-static tensile, compression, through thickness tension, and in-plane Isopescu shear tests along with quasi-static shear punch tests (QSSPTs) employing flat cylindrical and spherical punches

were performed on the composite samples to find 28 input parameters of MAT162. Finally, the capability of this material model to simulate a transverse ballistic impact of a spherical impactor with the thin 5-layers CFRP is demonstrated.

It is hypothesized that the high electrical conductivities of CNTs will span the multifunctionality of the hybrid composites by facilitating electromagnetic interference (EMI) shielding. Chapter 6 is devoted to characterizing the electrical properties of hybrid CNT-fiberglass FRPs modified via GSD method. Using a slightly modified version of the GSD, denser and longer CNTs were grown on fiberglass fabrics. The EMI shielding performance of the composites based on these fabrics was shown to be superior to that for reference composites based on fiberglass and epoxy. To better apprehend the effect of the surface grown CNTs on the electrical properties of the resulting composites, the electrical resistivities of the hybrid and the reference composites were measured along different directions and some interesting results are highlighted herein.

The work outlined in this dissertation will enable significant advancement in protection methods against different hazards including impact, vibrations and EMI events.

Dedication

This dissertation is dedicated to my loving parents, Azar and Hossein, without whom the completion of this work would have been impossible.

Acknowledgements

I would like to thank my advisor, Professor Marwan Al-Haik, for his guidance, encouragement, and support over the course of my graduate career. I am highly grateful and proud to have worked under his supervision. He taught me how to be a good and productive researcher, well present my work and be a good teacher. He taught me a great deal besides science and engineering; mentorship, work ethics and patience. I would also like to thank my committee members for their participation and support. I would like to express my special thanks to Professor Scott Case for his helpful discussions and guidance. He has been an insightful and helpful committee member and teacher during my graduate career. I would like to thank Professor Hamid Garmestani at Georgia Tech for his constant guidance, help, and research collaboration. I would also like to thank Professor Ramesh Batra for equipping me with the fundamental understanding of the dynamic FEM.

I would like to thank all my group members, previous and present, for their help, advice, encouragement, discussions, time, and support including Caleb Hanson, Ayoub Y. Boroujeni, Tony Nelson, Thomas Haugh, Masoud Safdari, Amir A. Skandani, Nejib Masghouni, Ramez Hajj, Casey Dyck, and Daniel Garcia. I would also like to thank all my collaborators including Dr. Zohreh Razavi, Professor Claudia Luhrs and Professor Jonathan Phillips. I would like to express my gratitude to Professor Majid Manteghi at ECE department and Professor Zhixian Zhou at Wayne State University for their help and insight on the EMI and electrical conductivity measurements. I would like to thank Professor Mitsu Murayama of MSE department for his assistance with the high resolution TEM imaging. I would also like to extend my appreciation to Stephen McCartney of NCFL-ICTAS for the trainings and the insight he gave me on FESEM

and AFM. I would like to thank Dr. Mana Tamami for her help with training and performing of the TGA. I would also like to thank Tim Hartman and Guillaume Antoine for their insightful help with LS-DYNA simulation and also for Tim's help with the gas gun experiments. I would like to thank Pierce Umberger for his help and training of DMA and QSSPT. I would like to thank all ESM staffs and faculty members who have helped me with preparing and testing of my specimens and with ordering and delivering of my packages.

Finally, I am forever grateful to my family: Mohammad, Ghazal, Maziar, Niloofar, Amin, Azar and Hossein for their continued love and support in my life endeavors. I am deeply indebted to my father and mother for their endless and unconditional support and love. At the end, I cannot ever forget my parents' sacrifices to provide me encouragement and motivation to pursue my goals.

Table of Contents

Chapter 1. Introduction.....	1
1.1 <i>Fiber reinforced polymer composites</i>	1
1.2 <i>Nanocomposites</i>	2
1.3 <i>Evolution of hybrid composites</i>	4
1.4 <i>Objectives</i>	6
Chapter 2. Nanocharacterization of the Mechanical Behavior of Carbon Nanotubes Epoxy Nanocomposite	10
2.1 <i>Overview</i>	10
2.2 <i>Introduction</i>	11
2.3 <i>Nanoscale mechanical characterization of nanocomposites</i>	13
2.3.1 <i>Nanoindentation</i>	13
2.3.2 <i>Nanoindentation creep</i>	17
2.3.3 <i>Nano-impact</i>	18
2.4 <i>Experimental</i>	19
2.4.1 <i>Materials</i>	19
2.4.2 <i>Nanocomposite sample preparation for nanoindentation and nanocrep tests</i>	20
2.4.3 <i>Nanocomposite sample preparation for nanoimpact tests</i>	21
2.4.4 <i>Nanoindentation, nanocrep and nanoimpact tests</i>	24
2.5 <i>Results and discussion</i>	31
2.5.1 <i>Nanoindentation results</i>	31
2.5.2 <i>Nanocrep results</i>	34
2.5.3 <i>Nanoimpact results</i>	40
2.6 <i>Conclusions</i>	41
Chapter 3. Mechanical Characterization and Impact Damage Assessment of a Woven Carbon Fiber Reinforced Carbon Nanotube-Epoxy Composite	43
3.1 <i>Overview</i>	43

3.2	<i>Introduction</i>	44
3.3	<i>Material and methods</i>	48
3.4	<i>Results and discussion</i>	54
3.5	<i>Conclusions</i>	64
Chapter 4. Growing Carbon Nanotubes over Carbon Fibers.....		66
4.1	<i>Overview</i>	66
4.2	<i>Introduction</i>	67
4.3	<i>Experimental methods (utilizing Pd as catalyst)</i>	71
4.3.1	Sample preparation	71
4.3.2	Filament Generation.....	72
4.4	<i>Experimental methods utilizing Ni as catalyst</i>	73
4.4.1	Sample preparation	73
4.4.2	CNT growth	73
4.4.3	Sample characterization	75
4.5	<i>Results and discussion (Pd as catalyst)</i>	75
4.6	<i>Results and discussion (Ni as catalyst)</i>	78
4.6.1	Electron microscopy and Raman analysis	78
4.7	<i>Conclusions</i>	83
Chapter 5. Mechanical Characterization of a Hybrid Multiscale Composite based on Fabrics with Surface Grown CNTs		84
5.1	<i>Overview</i>	84
5.2	<i>Introduction</i>	85
5.3	<i>Experimental methods</i>	88
5.3.1	AS4 fibers with polymer sizing	88
5.3.2	De-sized IM7 fibers	90
5.4	<i>Results and discussion of composites based on sized AS4 fibers</i>	91
5.5	<i>Results and discussion of composites based on the de-sized IM7 fibers</i>	103
5.6	<i>Conclusions</i>	111

Chapter 6. Modeling of the Impact of Carbon Fiber Reinforced Panels Considering Impact Progressive Damage and Strain-Rate Effects.....	114
6.1 Overview	114
6.2 Introduction.....	115
6.3 Experimental Procedure	116
6.4 FEM modeling	120
6.5 MAT_COMPOSITE_MSC_DMG (MAT 162).....	127
6.6 Results and discussion	131
6.7 Conclusions.....	135
Chapter 7. Electromagnetic Interference (EMI) Shielding of Hybrid Fiberglass Reinforced Composites	136
7.1 Overview	136
7.2 Introduction.....	137
7.2.1 EMI Shielding Theory	138
7.2.2 Materials for EMI shielding.....	141
7.3 Experimental methods.....	144
7.4 Results and discussion	146
7.5 Conclusions.....	150
Chapter 8. Conclusions and Future Work.....	152
List of publications from the dissertation	155
References	156

List of Figures

Fig. 1.1. Schematic outline of the dissertation.....	8
Fig. 2.1. Loading and unloading in nanoindentation showing the indentation (a) loading and unloading curves (b) schematic of loading and unloading surfaces.	14
Fig. 2.2. TEM image of MWCNTs bundles. Inset: high resolution TEM image showing a MWCNT with an average diameter of 20 nm. The scale bar reads 10 nm.....	20
Fig. 2.3. a) SEM micrograph of the fracture surface of the MWCNTs-Aeropoxy composite sample. b) High resolution SEM of one of the agglomerations. Inset: The scale bar is 100 nm..	22
Fig. 2.4. SEM micrograph of the fracture surface of functionalized MWCNTs–epoxy sample..	24
Fig. 2.5. Schematic of the NanoTest 600 mechanical testing system.....	25
Fig. 2.6. Schematic of the NanoTest hot stage feature (Courtesy of Micro Materials Ltd.)	26
Fig. 2.7. Representative loading and unloading hysteresis for both neat epoxy and MWCNTs-epoxy composite samples at maximum loads of 1, 2 and 3 mN, respectively. Tests were performed at 25 °C.....	27
Fig. 2.8. Representative loading and unloading hysteresis for both neat epoxy and MWCNTs-epoxy composite samples at maximum loads of 1, 2 and 3 mN, respectively. Tests were performed at 55 °C.....	27
Fig. 2.9. Nanoindentation creep tests of both neat epoxy and nanocomposite samples. Creep was performed at maximum loads of 1, 2 and 3 mN, respectively, at 25 °C.....	29
Fig. 2.10. Nanoindentation creep tests of both neat epoxy and nanocomposite samples. Creep was performed at maximum loads of 1, 2 and 3 mN, respectively, at 40 °C.....	29
Fig. 2.11. Nanoindentation creep tests of both neat epoxy and nanocomposite samples. Creep was performed at maximum loads of 1, 2 and 3 mN, respectively, at 55 °C.....	30
Fig. 2.12. Representative Nanoimpact penetration depth versus time for the reference neat epoxy sample	31
Fig. 2.13. Contact creep compliance for neat epoxy and nanocomposite systems at 25 °C.	35
Fig. 2.14. Contact creep compliance for neat epoxy and nanocomposite systems at 40 °C.	36
Fig. 2.15. Contact creep compliance for neat epoxy and nanocomposite systems at 55 °C.	36
Fig. 3.1. Schematic of the gas gun setup	51

Fig. 3.2. The impactor captured at 30,000 frames per second rate a) before and b) after the impact. c) image processed cumulative images used for calculating the residual velocity	52
Fig. 3.3. Hemispherical (left) and flat cylindrical (right) punches used in the shear punch study (all measurements are in mm).....	53
Fig. 3.4. SEM micrographs for the fracture surface of MWCNTs–epoxy composite sample: (a) global dispersion and (b) local dispersion	55
Fig. 3.5. SEM micrographs for the cross section of the CFRP containing MWCNTs (a) and CFRP based on neat epoxy (b).....	55
Fig. 3.6. Representative stress-strain curves for the composites comprising neat epoxy and CNT-epoxy matrices.	56
Fig. 3.7. Tensile properties for the two composite systems.....	58
Fig. 3.8. Damping ($\tan\delta$) and storage modulus for the two composites based on neat epoxy and MWCNTs-epoxy matrices measured at various frequencies.....	59
Fig. 3.9. Impactor absorbed impact energies and absorbed energy of the shear punch tests using cylindrical and hemispherical punches for the composites based on neat epoxy and MWCNTs-epoxy matrices.	60
Fig. 3.10. Representative shear punch tests obtained for flat cylindrical (left) and hemispherical (right) punches	62
Fig. 3.11. X-ray radiographs of the impacted samples; (a) reference CFRP and (b) MWCNTs enriched CFRP	64
Fig. 4.1. Nickel catalyst layer (a) before and (b) after reduction under N_2-H_2 at 550 °C; nickel islands were formed. (c) CTNs grown utilizing GSD technique with nickel particles attached to their tips.	74
Fig. 4.2. SEM of Sub-micron Filaments. These samples were treated in a 1:1 mixture of $O_2:C_2H_4$ for 90 minutes at 550 °C. a) A ‘perspective’ view of several filaments that were pretreated PAN-based carbon fibers. b) A closer view reveals that the filaments are generally less than 100 nm in diameter, are not straight and tangle together to form mats. c) Note that there appear to be metal particles at the ‘head’ of many of the filaments.....	76
Fig. 4.3. Nano-scale Filaments. A) Relatively dense layer of filaments with an average diameter of ca. 10 nm forms on the surface of the fibers. The average height of this layer is less than 200 nm. B) The Pd particles that catalyze filament growth can clearly be seen. C) The dramatic difference in size of the two types of filaments can be observed in the figure. This sample was treated under GSD conditions for only 35 minutes. The metal loading weight was 0.5%.	76
Fig. 4.4. SEM of saturation loaded sample. To allow growth sufficient to observe with SEM, sample treated using standard protocol, but with 270 minutes of exposure to GSD conditions. (A)	

Clearly the fibers are not covered with sub-micron filaments. Contrast with Fig. 4.2. (B) The surface is virtually completely covered with nanofilaments..... 77

Fig. 4.5. (a-b) TEM micrograph of MWCNTs grown via GSD (c-d) TEM micrograph of MWCNTs grown via CCVD. 80

Fig. 4.6. TEM image of a nickel particle from which a CNT was grown (a) and the EDS of the same particle (b)..... 81

Fig. 4.7. Raman spectra of the surface of different processed carbon fibers. Specimens are based on raw PAN-based carbon fabric (Raw), SiO₂ sputter-coated fabric (Sp), heat treated fabric (HT), SiO₂ sputter-coated then heat treated fabric (Sp+HT), and the samples with CNTs grown on their surfaces via GSD (GSD) and CCVD (CCVD). 82

Fig. 5.1. Polyester mesh discs; a) thread size 400 μ, opening size 840 μ, and an open area of 46% and b) thread size 76 μ, opening size 140 μ, and an open area of 24%. Inset: mesh pattern showing the threads and open areas..... 91

Fig. 5.2. Cross-sectional micrograph of a carbon fiber grafted with surface grown CNTs utilizing the GSD technique 93

Fig. 5.3. polymer matrix penetration of the region adjacent to the CNTs for the composites based on GSD and CCVD methods. 94

Fig. 5.4. The cross sections of all fabricated composite samples were investigated under scanning electron microscopy (SEM). The cross sectional images of all samples as well as magnified images for the GSD and CCVD samples are shown below. The SEM micrographs show the same level of matrix penetration for all samples. 95

Fig. 5.5. The storage modulus for composites made out of Raw (reference raw fabric), HT (heat treated fabric), Sp (sputter-coated fabric), Sp+HT (sputter-coated and then heat treated fabric), GSD (sputter-coated sample with CNTs using the GSD method), and CCVD (sputter-coated sample with CNTs using the CCVD method)..... 100

Fig. 5.6. The loss tangent for composites made out of Raw (reference raw fabric), HT (heat treated fabric), Sp (sputter-coated fabric), Sp+HT (sputter-coated and then heat treated fabric), GSD (sputter-coated sample with CNTs using the GSD method), and CCVD (sputter-coated sample with CNTs using the CCVD method)..... 101

Fig. 5.7. Loss modulus measurements for composites made out of Raw (reference raw fabric), HT (heat treated fabric), Sp (sputter-coated fabric), Sp+HT (sputter-coated and then heat treated fabric), GSD (sputter-coated sample with CNTs using the GSD method), and CCVD (sputter-coated sample with CNTs using the CCVD method). 103

Fig. 5.8. SEM micrographs of GSD surface grown CNTs on (a) de-sized fibers, (b) sized fibers, (c) sized and SiO₂-coated fibers, and (d) de-size fibers..... 104

Fig. 5.9. Impregnation of surface fibers with the epoxy matrix for composites based on raw fibers (left) and fibers with surface grown CNTs (right).....	105
Fig. 5.10. On-axis tensile properties of the composites based on raw (R) and heat treated (HT) fibers, fibers with surface grown CNTs via GSD (GSD(Ni)), fibers with predeposited SiO ₂ coating and surface grown CNTs via GSD (GSD(sp+Ni)), fibers with a coarse mesh (pattern) surface grown CNTs via GSD (GSD(CP+Ni)), fibers with a fine mesh (pattern) surface grown CNTs via GSD (GSD(FP+Ni)), and fibers with surface grown CNTs via GSD that were grown for an hour compared to the half hour growth time utilized in all other configurations (2*GSD(Ni)).	109
Fig. 5.11. Off-axis tensile properties of the composites based on raw (R) and heat treated (HT) fibers as well as fibers with surface grown CNTs via GSD (GSD); no SiO ₂ was predeposited onto the fibers.	110
Fig. 6.1. Schematic of the test fixture [143] (left) and the sample dimensions (right) for double V-notched shear test. All dimensions are in mm.	118
Fig. 6.2. Combined load compression (CLC) test fixture; to measure the displacements an extensometer was mounted on the ultra-rigid fixture.	119
Fig. 6.3. The Circular hollow drill bit and the cut samples (left) and the through thickness fixture and the sample mounted on one of the aluminum cylinders.....	119
Fig. 6.4. FEM model for the Hertz contact verification problem.....	122
Fig. 6.5. Deviation of the numerical solution from the Hertz solution for the contact of a sphere with an elastic half-space	123
Fig. 6.6. FEM models for the a) cylindrical and b) spherical punches QSSPT and the c) transverse impact simulations.....	124
Fig. 6.7. Energy components evolution for the impact test; all energies are in joules.	126
Fig. 6.8. Four representative QSSPT load-displacement curves and the FEM simulation results	133
Fig. 7.1. Path of electromagnetic wave through a conductive shielding barrier	139
Fig. 7.2. The uniform aerial cover of the CNTs over the fiberglass at different magnifications	146
Fig. 7.3. EMI SE for different composite specimens	147
Fig. 7.4. In-plane electrical resistance versus the specimen length for the hybrid GRP-CNT composites.....	148
Fig. 7.5. Through thickness resistance versus the specimen length for the hybrid GRP-CNT composites.....	149

Fig. 7.6. Tensile mechanical properties of the samples based on raw (Raw), SiO₂ and Ni sputtered (Sp), SiO₂ and Ni sputtered and heat treated (Sp+HT), and surface grown CNTs (GSD) fabrics..... 150

List of Tables

Table 2.1. Properties of the Aeropoxy system	19
Table 2.2. Nanoindentation and creep nanoindentation results for the neat epoxy and the nanocomposite systems at different load-temperature environments.	33
Table 2.3. Impact penetration depths and crate volume changes for the neat epoxy and nanocomposites based on SWCNTs and MWCNTs	40
Table 3.1. Peak load and absorbed energy of shear punch tests using cylindrical and hemispherical punches	62
Table 5.1. Fiber volume fractions for the specimens based on raw PAN-based carbon fabric (Raw), SiO ₂ sputter-coated fabric (Sp), heat treated fabric (HT), SiO ₂ sputter-coated then heat treated fabric (Sp+HT), and the samples with CNTs grown on their surfaces via GSD (GSD) and CCVD (CCVD).....	93
Table 5.2. Tensile mechanical properties for the specimens based on raw PAN-based carbon fabric (Raw), SiO ₂ sputter-coated fabric (Sp), heat treated fabric (HT), SiO ₂ sputter-coated then heat treated fabric (Sp+HT), and the samples with CNTs grown on their surfaces via GSD (GSD) and CCVD (CCVD).....	97
Table 5.3. Fiber volume fractions for composites based on raw (R) and heat treated (HT) fibers, fibers with surface grown CNTs via GSD (GSD(Ni)), fibers with predeposited SiO ₂ coating and surface grown CNTs via GSD (GSD(Sp+Ni)), fibers with a coarse mesh (pattern) surface grown CNTs via GSD (GSD(CP+Ni)), fibers with a fine mesh (pattern) surface grown CNTs via GSD (GSD(FP+Ni)), and fibers with surface grown CNTs via GSD that were grown for an hour compared to the half hour growth time utilized in all other configurations (2*GSD(Ni))......	106
Table 5.4. Transverse impact incident and residual velocities and the calculated absorbed energy by the reference composite based on raw fabric and the hybrid composite based on fabric with surface grown CNTs via GSD (no SiO ₂ layer was applied)	111
Table 6.1. MAT162 input material properties for a plain weave CFRP	128
Table 6.2. The experimental and numerical peak loads of the QSSPTs and their corresponding errors	132
Table 6.3. Employed input values for MAT162	134

Chapter 1. Introduction

1.1 Fiber reinforced polymer composites

Fiber reinforced polymer plastics (FRPs) possess superior strength and elastic modulus to weight ratios. The relative ease of manufacturing, light weight components, wide range of physical properties, high corrosion resistance and fatigue life make FRPs very desirable for different applications [1, 2]. They are considered as alternative materials (replacing metals) for structural applications and nowadays are widely used in automotive, marine, and aircraft industries [1, 3]. Another key feature of FRPs is their manufacturing flexibility, which allows them to achieve material properties that are difficult to attain using single-phase materials. Depending on the specific application, different fibers (e.g. carbon, glass, and aramid) and polymer matrix (e.g. epoxy, vinyl ester, polyester, and thermosetting plastic) might be used to fabricate the FRPs. Compared to other fibers, carbon fibers are utilized when fatigue resistance, moderate strength, and electrical conductivity are needed and when weight savings are a major concern. Carbon fiber reinforced plastics (CFRPs) possess less than 2-3 % strain to failure and are available in standard, intermediate, and high modulus. However, due to their lower cost and excellent properties, fiberglass is the most commonly used fiber reinforcement. Fiberglass offers good thermal and electrical resistances.

While retaining various structural applications, the lack of the multifunctionality of FRPs has become a disqualifying factor for specific applications such as blast mitigation and electromagnetic interference (EMI) shielding. Moreover, despite their attractive in-plane mechanical properties most traditional FRP laminates suffer from relatively poor out-of-plane

performance. A fundamental weakness in existing FRPs is their limited deformability (ductility), and low interlaminar shear strength, and impact resistance. Their out-of-plane mechanical properties are limited by the inadequate properties of the matrix material and the weak adhesion strength of the fibers to the matrix. For example, mode I and mode II fracture toughness values change significantly with varying the fiber-matrix adhesion [4].

The incorporation of elastic fibers within viscoelastic matrix restricts the total energy absorption capability of the composite when exposed to blast or impact events. Furthermore, their vibration damping performance is often too low for many applications and specific modifications are usually required to overcome these shortcomings [5]. Although the CFRPs possess numerous outstanding properties, the modification of fibers and/or matrix can be implemented to enhance the CFRP and add extra functionality to it. These modifications could be achieved by surface treatment of the fiber or by adding an additional filler phase with enhanced properties to form a “hybrid” composite with multi-fillers.

1.2 Nanocomposites

Carbon nanotubes (CNTs) [6] represent a unique form of carbon visualized by considering a single graphene sheet (representing a lattice of carbon atoms distributed in a hexagonal pattern) rolled into a tube [7]. The attractive properties of CNTs, typically 1 to a few nm in diameter, are attributed to their unique and minimal defect nanostructure. Single wall carbon nanotubes (SWCNTs) possess exceptional mechanical, thermal, and electric properties compared to macroscale fibers such as graphite, Kevlar, SiC and alumina[8]. The extraordinary mechanical, electrical, and thermal properties of CNTs have attracted researches to utilize these nano-scale structures as a filler phase in composite materials in order to improve the properties of the host

matrix. A plethora of investigations have been accomplished since the discovery of the multiwall carbon nanotubes (MWCNTs) in 1991 on utilizing them for different applications including, but not limited to, structural, thermal, electromagnetic, electroacoustic, chemical, and electrical circuits [9]. The strength, stiffness and the fracture properties of CNTs are orders of magnitudes higher than most common structural materials used in civilian and military applications [10]. For example, an epoxy nanocomposite based on MWCNTs (~ 2% volume fraction) showed an increase in Young's modulus and yield strength by 100% and 200%, respectively and nine orders of magnitude improvement in the electrical conductivity compared to the neat epoxy [11]. Moreover, CNTs reinforcement increases the toughness of the composite to absorb impact energy due to their highly elastic behavior during loading.

Researchers have attempted to incorporate CNTs in polymer matrices and had met limited success due to the extreme difficulty in uniformly dispersing CNTs in polymeric matrices because of the large surface area of CNT [5]. The high-aspect ratio CNTs tend to entangle and form agglomerates when dispersed into a matrix (e.g., polymer). Rather intricate chemical and physical routes should be employed to moderately disentangle CNTs and disperse them into the matrix. These chemo-physical processes might affect the CNT structure by damaging its covalent bonds, or inducing undesired functionalizing to it and/or removing CNTs semispherical end caps. Sonication [6] and calendaring [7] have been used extensively to mitigate this problem, but are not effective beyond ~3.0 wt % CNT volume fraction due to the formation of aggregates [12]. A combination of dispersion and extrusion techniques have been reported in the literature for producing CNTs composites [12] with tailored microstructure, e.g. aligned CNTs. However, in both dispersion and extrusion techniques, producing uniform and well-dispersed CNTs

composite is difficult because of the small amount of solid ‘powder’ (carbon) compared with the large amount of liquid polymer (matrix) in early mixing stages. This often leads to phase separation due to the strong Van der Waals attractions amongst the CNTs bundle compared with that between the CNTs and the polymer matrix[13]. Furthermore, excessive sonication of SWCNTs toward better dispersion might result in breaking them into shorter tubes and thus reducing their aspect ratio [14] and, consequently, negatively affects their corresponding composites performance.

1.3 Evolution of hybrid composites

To capitalize on the remarkable properties of both CFRPs and CNTs, hybrid carbon fiber reinforced CNT-polymer were developed [15]. However, the inadequacies with the dispersion of CNTs into the matrix were present. Alternatively, to eliminate the need for dispersion and deagglomeration, CNTs can be controlled-grown on the surfaces where they are needed. CNTs can be grown on most substrates such as silicon, silica, and alumina [16]. However, there are fewer reports discussing the CNTs growth on carbon materials; in particular yarns and fabrics [17]. Two challenges in CNTs growth on carbon substrates are (i) transition metals (i.e. catalysts for CNTs’ synthesis) are easily diffused into the carbon substrates and, (ii) the different phases of carbon materials are able to form on the graphite substrates because the growth conditions are similar to the diamond or diamond-like carbon growth [18].

Catalytic chemical vapor deposition (CCVD) has been broadly utilized to grow carbon nanofilaments on the surface of carbon fiber yarns with the aid of catalysts such as nickel, iron, cobalt and palladium at temperatures ranging from 700 to 1100 °C [2, 7, 19-24]. However, the temperature needed for the growth of CNTs utilizing CCVD is rather high and is destructive to

the substrate carbon fiber strength itself [25, 26]. For example, Thostenson et al. [10] utilized CVD (at 700 °C) to grow CNTs on carbon fibers then fabricated a composite based on them. They reported that the exposure to growth conditions resulted in significant degradation of the fiber/matrix interface. Similarly, Zhang et al. [25], upon utilizing CVD (at 700-800 °C) to grow CNTs on PAN carbon fibers, reported that the strength of the T650 fiber was reduced by nearly 40% due to the exposure to elevated temperatures. While the fiber dominated properties of the CFRPs were shown to degrade due to the exposure to the high CCVD temperatures, the interlaminar properties (e.g. interlaminar shear strength) of the composites containing CCVD grown CNTs was reported to improve [27, 28].

Recently, a low-temperature technique, Graphitic Structure by Design (GSD), to grow MWCNTs on the surface of carbon fibers was proposed [24]. The fundamental difference between the GSD and alternative methods is that graphitic structures from carbon containing radicals are produced by homogenous reaction processes, whereas in all other methods (e.g. CVD) carbon structures are formed via thermal decomposition of a hydrocarbon species on the surface [19, 24, 29]. To better illustrate the significance of a method that enables placement of CNTs on fabrics with no degradation to the fiber substrate, a summary of the study conducted by Veedu et al. [30] is provided here. They grew CNTs utilizing CCVD method over SiC woven yarns. SiC is satisfactorily thermally resistant to the CCVD temperatures that were used in that study. Veedu et al. [30] fabricated composites based on the hybrid fabrics and compared the mechanical, electrical, and thermal properties of the hybrid multifunctional composites with the reference composite based on raw fibers (with no CNTs growth or any other preprocessing). They reported a 348% improvement in mode I fracture toughness, 140% enhancement of flexural

strength, 424% increase in flexural toughness. Furthermore, the damping capability of the hybrid composite was enhanced by 514% over the base composite. The CNTs/SiC composites' through-the-thickness thermal conductivity was increased by 51% over the base sample and finally the electrical conductivity peaked from 0.075×10^{-6} (S cm⁻¹) for the SiC base composite to 0.408 (S cm⁻¹) for the hybrid composite based on SiC/CNTs fibers

1.4 Objectives

The exponentially growing application of fiber reinforced polymeric composites in aerospace, automotive, and marine markets requires an active quest to overcome some of their shortcomings. While the light weight is the prime design factor in aerospace structures, methods that improve the properties of the composites with a minimal weight penalty are preferably sought. Integrating small fractions of nano-materials into polymeric systems have shown promise to significantly enhance some properties of the host matrix. A systematic approach is pursued throughout this dissertation to investigate the effect of adding CNTs to the conventional epoxies and FRPs via different routes on the resulting hybrid composite mechanical and, to a lesser extent, electrical properties. In particular the dissertation will utilize new schemes of processing hybrid composites that comprise two scales of fibers; micro and nano scales, and then test the mechanical performance of these hybrid composites under quasi-static, vibration and impact environments. In a complimentary study the simulation of the impact behavior of hybrid CFRPs is targeted herein. Finally, to address the multifunctionality of the hybrid composites, the electrical conductivity of hybrid composites based on CNTs and fiberglass and its implications on EMI shielding are investigated. Fig. 1.1 illustrates the dissertation outline.

The dissertation organization is as follows: Chapter 1 provides state-of-the-art review for FRPs and CNTs-based composites together with the significance of the hybrid composites based on FRPs/CNTs combinations. Chapter 2 illustrates the benefits of adding CNTs to a polymeric matrix through mechanical and ultrasonic mixing considering the scale of the reinforcement the mechanical characterizing of the CNT/epoxy composites are carried out utilizing the instrumented nanoindentation experiments which provide the stiffness and hardness of the nanocomposite, the nano creep for probing the viscoelastic properties, and the nanoimpact to illustrate the CNTs effect on the impact energy absorption performance of the nanocomposite. Upon establishing the effects of adding CNTs on the performance of a structural epoxy, chapter 3 expands the investigation to a hybrid composite based on carbon fibers and epoxy matrix enriched with CNTs.

One of the major contributions of this dissertation is developing novel methods to manufacture hybrid, multifunctional composites using surface grown CNTs on fibers' yarns. This contribution is detailed in chapter 4 where a novel technique that utilizes simple lab setup to grow CNTs at relatively low temperatures (~ 550 °C) is developed and successfully applied to grow CNTs over carbon fibers. Upon maturing the concept of carbon fibers with surface-grown CNTs, the mechanical performance (i.e. tensile, vibration, and impact) of the composites based on the surface grown CNTs is investigated in chapter 5.

In lieu of the costly impact experiments, in chapter 6 the transverse impact behavior of a thin CFRP using the state-of-the-art MAT162 material model in finite element (using the package LS-DYNA) is simulated. A systematic approach to calibrate the 32 input material parameters of MAT 162 form different mechanical tests is proposed. Finally to embrace the multifunctionality

beyond the mechanical performance, in chapter 7, fiberglass reinforced composites with surface grown CNTs are studied for enhanced electrical conductivity and consequently for electromagnetic interference (EMI) shielding. The choice of the fiberglass (rather than carbon fiber in this chapter was based on its poor electrical properties so that the effect of the surface grown CNTs is contrasted. Finally, chapter 8 summons up the different hybrid composites pros and cons together with proposed future work to further optimize the concept of hybrid composites.

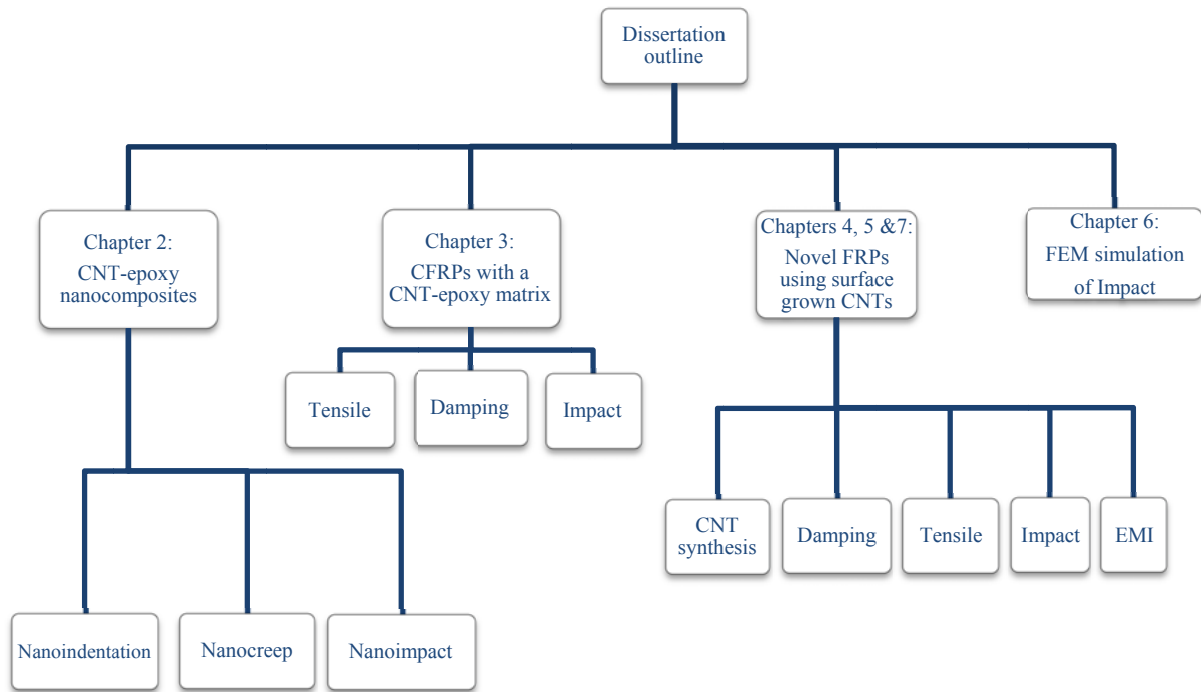


Fig. 1.1. Schematic outline of the dissertation

It is envisioned that effort carried out in this dissertation could pave the road for the next generation of multifunctional hybrid composites and that the findings of this research could enable significant advancement in protection methods against several structural hazards including impact/blast and unattenuated vibrations.

Chapter 2. Nanocharacterization of the Mechanical Behavior of Carbon Nanotubes Epoxy Nanocomposite

2.1 Overview

High-temperature instrumented indentation testing is utilized to evaluate the mechanical properties of multiwall carbon nanotubes (MWCNTs)/epoxy nanocomposite system. Reference neat epoxy samples are also tested and compared with the results obtained for the nanocomposite. To characterize the viscoelastic response of the nanocomposite and reference neat samples nanoindentation creep tests are utilized to provide the contact creep compliance and the time-dependent deformation under constant loads. Different thermo-mechanical conditions comprising three temperatures of 25, 40, and 55 °C and three loads of 1, 2 and 3 mN were utilized. The improvements in the properties were not as high as anticipated through the use of mixture rule, indicating insufficient dispersion of the CNTs. However, the variations in stiffness, hardness and creep rate obtained using nanoindentation showed quantifiable differences between the MWCNTs nanocomposite and neat epoxy specimens. The analysis of the contact creep compliance values clearly revealed that the addition of MWCNTs to a commercial epoxy reduced the creep rate. This reduction of the creep rate was observed particularly at thermal environments just below the glass transition temperature of the epoxy system.

To probe the changes in the energy absorption capabilities, repetitive nanoimpact of the neat reference sample along with the nanocomposites based on MWCNTs and single-wall carbon nanotubes (SWCNTs) were also carried out. The ability of the different samples to withstand

plastic deformation was measured as a gauge to determine their impact resistance. The measured nanoimpact strain energy density is comparable to those in macroscale high velocity impact tests.

2.2 Introduction

The fabrication of high performance nanotube-based composites is driven by the ability to create anisotropy at the molecular level in order to obtain optimal mechanical properties. The structural strength and toughness of polymers could be significantly increased using carbon nanotubes. For example, a cast composite film consisting of polystyrene and carbon nanotubes (5% volume fraction) exhibits a 100% increase in the modulus and 25% increase in the strength of the polystyrene [10].

The investigation of the mechanical behavior of polymeric composites based on CNTs is a topic of ongoing research. Several investigations have studied the elasticity [31, 32], damage [33], buckling [34, 35], tribology [36, 37] and toughness [38] of CNTs-based composites. Other groups have investigated the changes in the glass transition behavior of polymers as a result of adding carbon nanotubes [39, 40].

Recently, the viscoelastic and creep behavior of CNTs-based composites gained momentum toward using them for damping and impact applications. Zhou et al. [41], have utilized uniaxial tensile test to measure the loss factor of nanocomposites based on SWCNTs. Alternatively, Suhr et al. [42] utilized direct viscoelastic shear mode of CNTs-epoxy composite thin films to characterize the complex compliance and material loss factor. The investigators reported a 1400 % increase in loss factor (damping ratio) of the baseline epoxy by adding 50% CNTs by volume.

Long-term viscoelastic/viscoplastic behavior of CNTs-based composites was investigated by Zhang et al.[43] using uniaxial tensile tests. It was demonstrated that SWCNTs additives in low weight fractions (0.1-0.25%) are effective in limiting the load induced re-orientation of the epoxy chain; resulting in significant slowing of the creep response.

Efforts for modeling the viscoelastic properties of CNTs-based composites were carried out using both macroscale and microscale models. Plaseied and Fatemi [44] implemented a three-parameter Findley-type creep law [45] for predicting the creep compliance of a nanocomposite based on vinyl ester with 0.5%wt carbon nanofibers. Li et al. [46] developed a micromechanics model for predicting the linear viscoelastic properties of CNTs reinforced polymer composites. The authors extended a Mori-Tanaka method to the Carson domain. The inversion of creep compliance from the Carson (transformed) domain to the time (physical) domain was accomplished by numerical algorithms.

Aside from the previous mentioned investigations, there are not many studies that report the creep behavior of CNTs-based composites under accelerated creep environment (high loads and high temperatures). Moreover, despite the increasing use of instrumented nanoindentation, there are few investigations reporting the creep behavior of these composites via nanoindentation.

Moreover, CNTs toughen the host polymer matrix by polymer chain scissioning, immobilizing the polymer chains and inhibiting their flow and by frictional sliding at the CNTs/polymer interface [47]. Impact indentation can be used as an effective way of studying impact resistance and energy absorption of polymeric and soft materials [48, 49].

This chapter extends the use of high-temperature instrumented nanoindentation to MWCNTs-epoxy composite at different loads. Furthermore, these nanoindentation tests are utilized to provide the contact creep compliance and the time-dependent deformation during indentation at constant loads. In addition, via the nanoimpact module, energy absorption capabilities of MWCNTs and SWCNTs epoxy nanocomposites are measured and compared to that of a reference neat epoxy.

2.3 Nanoscale mechanical characterization of nanocomposites

2.3.1 Nanoindentation

Nanoindentation has been widely used for mechanical characterization of polymers, metals, soft tissues, and nanocomposites [48, 50]. Due to the ease of sample preparation, minimal size requirement of the test sample, and the invaluable information that nanoindentation provides on the microstructure of the material, it has gained a lot of momentum toward characterizing of nanocomposites of both SWCNTs and MWCNTs [47, 51, 52]. Stiffness and hardness, among many other key mechanical properties, can be extracted from a simple nanoindentation test [47].

A nanoindentation experiment consists of loading the specimen to a specific load (usually in the range of micro to milli Newtons), keeping the load constant to realize the material creep (if needed) and unloading the specimen leaving an indentation impression on the surface upon fully pulling out the nanoindenter tip. A schematic representation of the loading and unloading process and the parameters used in the analysis are shown in Fig. 2.1-a. The geometry of the indentation impression surface at loading and unloading using the Berkovich pyramid indenter are shown in

Fig. 2.1-b. The analysis of the load-indentation depth is typically carried out according to well-established contact mechanics; in this chapter using the Oliver-Pharr analysis [53].

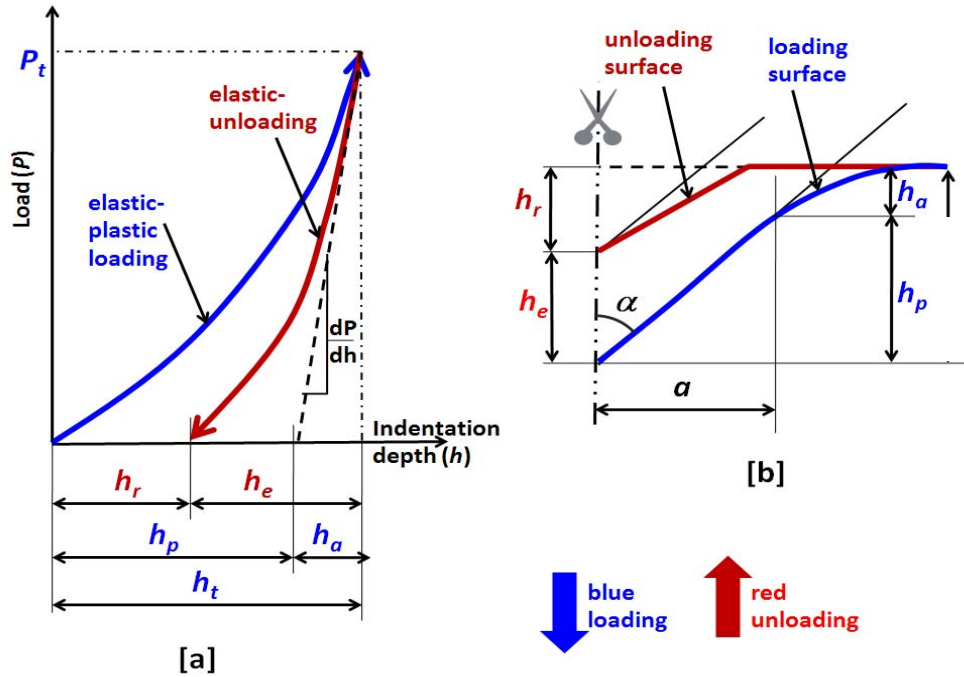


Fig. 2.1. Loading and unloading in nanoindentation showing the indentation (a) loading and unloading curves (b) schematic of loading and unloading surfaces.

Fig. 2.1 identifies the necessary parameters for the analysis; indentation depths: h_t , h_e , h_r for being total depth at load P_t , elastic depth rebound at unloading and residual impression depth, respectively. Here h_a is defined as the displacement of the surface at the perimeter and h_p the contact indentation depth. Following these definitions one can conclude that

$$h_t = h_a + h_p \tag{2.1}$$

The contact area of a perfect Berkovich indenter can be computed as a function of the contact indentation depth (h_p) as

$$A = 3\sqrt{3}h_p^2 \tan^2 65.3 = 24.5h_p^2 \quad (2.2)$$

Contact area measurements from indenting a fused silica reference sample at different depths revealed that for the Boron-Nitride indenter (BN is typically utilized for hot-stage nanoindentation rather than diamond) the contact area is

$$A = 6883h_p + 21.031h_p^2 \quad (2.3)$$

The hardness (H) can be computed at the maximum indentation load (P_t) as

$$H = \frac{P_t}{A} \quad (2.4)$$

By considering the unloading response, the reduced modulus of an isotropic specimen denoted, E_r , (representing the combined stiffness of sample and the indenter) can be directly related to the elastic modulus of sample E_s using

$$\frac{1}{E_r} = \frac{1-\nu_s^2}{E_s} + \frac{1-\nu_i^2}{E_i} \quad (2.5)$$

Where E_i and ν_i are the elastic modulus and Poisson's ratio of the indenter materials ($E_i = 800$ GPa and $\nu_i = 0.27$ for Boron Nitride) and ν_s is Poisson's ratio of the sample.

It is important to note that E_r can be used to represent our sample stiffness due to the very high stiffness of the indenter compared with epoxy. E_r can be computed from the unloading curve after Oliver-Pharr [46, 53]

$$E_r = \frac{1}{2\beta} \frac{dP}{dh} \sqrt{\frac{\pi}{A}} \quad (2.6)$$

Where dp/dh is the slope of the first 60 % span of the unloading curves as shown in Fig. 2.1-a and A is the contact area of the indentation from Eq.(2.3). The coefficient β is reported to be equal to 1.034 for the Berkovich indenter [50].

While the loading portion of the nanoindentation curve represents both the elastic and plastic deformations, the unloading portion mainly represents the elastic behavior, and thus the unloading result is what is needed to calculate the elastic modulus. It is well known that to improve the accuracy and compatibility of hardness and modulus results from nanoindentation experiments in polymeric materials on evolution of short term creep test is required. Upon reaching the maximum indentation load and holding it constant for few seconds, further depth increase arises due to viscoelastic nature of the epoxy. This creep behavior influences the maximum depth and slope of the upper portion of the unloading load which is used for calculating the contact stiffness and modulus. Therefore, this creep if not accounted for will influence the results. This depends on both the loading/unloading rates and the creep duration [54].

2.3.2 Nanoindentation creep

A useful method to analyze the nanoindentation creep relies on utilizing the creep compliance derived from creep data. The relation between strain and creep compliance can be described as

$$\varepsilon(t) = \sigma_0 J(t) \quad (2.7)$$

Where σ_0 is a constant stress and $J(t)$ is the creep compliance. Although conventional measurements for $J(t)$ include macroscale tensile or simple shear stress tests, researchers have increasingly interpreted an analogous creep compliance using instrumented nanoindentation creep. For nanoindentation creep test the load is maintained constant and $J(t)$ should measure the relation between the displacement and time. Since

$$\varepsilon(t) = \frac{h(t)}{h_{in}} \quad \text{and} \quad \sigma_0 = \frac{P_0}{A_0} \quad (2.8)$$

Then, Eq. (2.7) can be rewritten as

$$J(t) = \frac{A_0}{P_0 h_{in}} h(t) \quad (2.9)$$

It is worth emphasizing that the representation of creep compliance using Eq. (2.9) does not account for the nonlinearities in materials behavior and contact mechanics, rather, it assumes particular linear viscoelastic models to predict the creep response.

The viscoelastic contact problem has been solved elsewhere for different indenter shapes [55-59]. Unlike macroscale tensile creep tests, during nanoindentation creep, the penetration depth and hence the contact area increases with time such that the stress is not constant, but rather decreases with time. Nevertheless despite this difference, the viscoelastic contact models have been applied to the nanoindentation creep to yield the contact creep compliance [60]. In particular, although deformations on the apex of the sharp indenter are not fully categorized as small strain viscoelastic deformations, the constant indentation load is assumed to produce a constant stress by the virtue of self-similar geometry [56].

For a canonical indenter of semi-apex angle θ , using a constant force P_0 the contact creep compliance $J(t)$ is defined by [55, 58]

$$J(t) = \frac{A(t)}{(1-\nu)P_0 \tan \theta} \quad (2.10)$$

The effective cone angle for a Berkovich indenter is 70.3° and the Poisson's ratio ν is assumed to be 0.35. The contact area evolution with time is calculated from Eq. (2.3)

2.3.3 Nano-impact

Nano-impact test enables repetitive impacts of energized diamond probe into the material surface at regular time intervals at the same location with precisely controlled force, using a solenoid and timed relay. A magnetic solenoid pulls the pendulum away from the sample surface and while a predefined indentation load is applied to the pendulum, it is released to accelerate and impact the surface of the material. Then, the impact energy absorption of the material is measured as the

ability of the material to undergo less plastic deformation under repetitive impact [49, 61]. While the nano-impact speed is in mm/s range, its strain energy density is from few to hundreds of kJ/m^3 and hence comparable to the macroscale impact (velocity usually varies between 3-1000 m/s) strain energy densities [48].

2.4 Experimental

2.4.1 Materials

The matrix material used in this study is Aeropoxy™ manufactured by PTM&W Industries, Inc. It is a medium viscosity, unfilled, light amber laminating resin that is designed for structural production applications. This resin, brand name PR2032, laminates very easily and wets out fiberglass, carbon and aramid fibers readily. PR2032 mixed with PH3665 hardener, cures at room temperature within 24 hrs. This epoxy system was used to manufacture both FRPs [62, 63] and nanocomposites based on SWCNTs [13]. The typical properties of this epoxy system are listed in Table 2.1.

Table 2.1. Properties of the Aeropoxy system

Component	PR2032 Epoxy resin	PH3660 Curing agent
Viscosity of the mix	0.90-0.95 N.s/m ²	
Mix ratio by weight	100 : 27	
Density of the mix	11.09 kg/L	
Tensile strength	67.76 MPa	
Tensile modulus	2.885 GPa	

The carbon nanotubes used in this investigation are high purity (>95 %) MWCNTs and SWCNTs, Cheap Tubes Inc., 0.5-2 μ in length, with an outer diameter average of 20 nm and 1-2 nm, respectively. The purchased CNTs are heavily entangled as can be seen in the TEM image provided in Fig. 2.2.

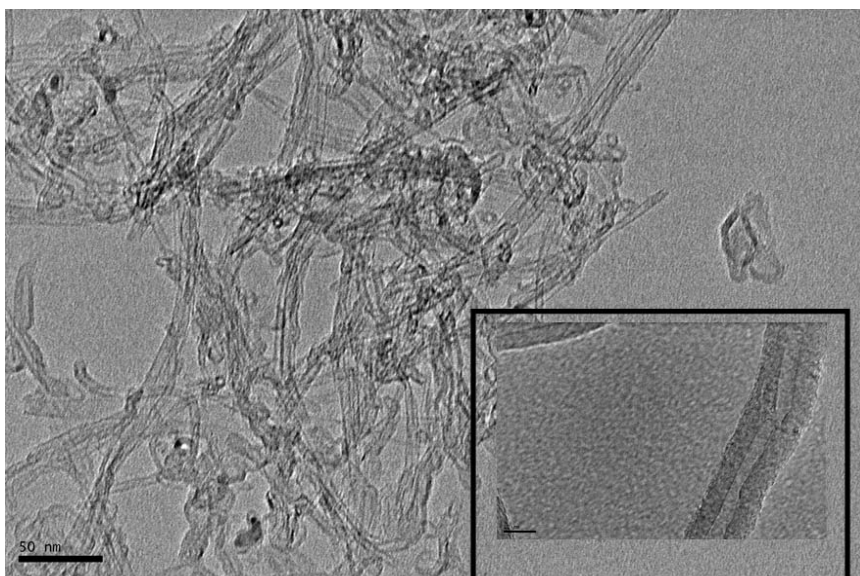


Fig. 2.2. TEM image of MWCNTs bundles. Inset: high resolution TEM image showing a MWCNT with an average diameter of 20 nm. The scale bar reads 10 nm.

2.4.2 Nanocomposite sample preparation for nanoindentation and nanocreep tests

Due to a high aspect ratios and intrinsic van der Waals attraction, CNTs form agglomerated bundles and ropes. Ultrasonication has been shown to be an effective way for moderately dispersing CNTs in some low viscosity solvents. A 1:10 by weight of MWCNTs to ethanol was sonicated for two hours using an ultrasonic cleaner at 40 kHz and 700 Watts power. The suspension was then added to the hardener and sonicated for one more hour. Subsequently, it

was vacuumed until the whole alcohol content was evaporated. The MWCNTs/hardener suspension was added to the resin. Further mixing and dispersion of nanotubes were performed with simultaneously using a mechanical stirrer and sonicator for a short period of time. The short gelling time of the epoxy is a limiting factor for longer dispersing of the nanotubes. Therefore, the samples were degaussed few minutes after the resin was added, to prevent any air bubbles from getting trapped in the nanocomposite. The produced nanocomposite contained 3 wt% nanotubes following the percolation limit. The neat epoxy sample was made using the same procedure stated above with the exception that no MWCNTs were added. The samples were left to cure for 24 hours at room temperature. When cured, the samples can be easily taken out of the container and a very smooth surface is attained.

A fracture surface of the nanocomposite was coated with gold and investigated under SEM. As shown in Fig. 2.3-a, MWCNTs were globally dispersed in a satisfactory manner in the polymer matrix at small scale of 10 μ (Fig. 2.3-b), with apparent agglomeration at larger scales.

2.4.3 Nanocomposite sample preparation for nanoimpact tests

In order to achieve a better quality dispersion of the CNTs in the polymer matrix, as received MWCNTs and SWCNTs they were treated with a nitric acid (HNO₃) solution. The solution was prepared by diluting 15.8 (N) HNO₃ with deionized water at a volume ratio of 1:4 acids to DI water. The CNTs were added to this solution and subjected to bath ultrasonication for 3 hours at a temperature of ~39°C. Single and multi-walled CNTs with a length of less than 2 μ m and an outer diameter of 1-2 nm and less than 8 nm respectively were used.

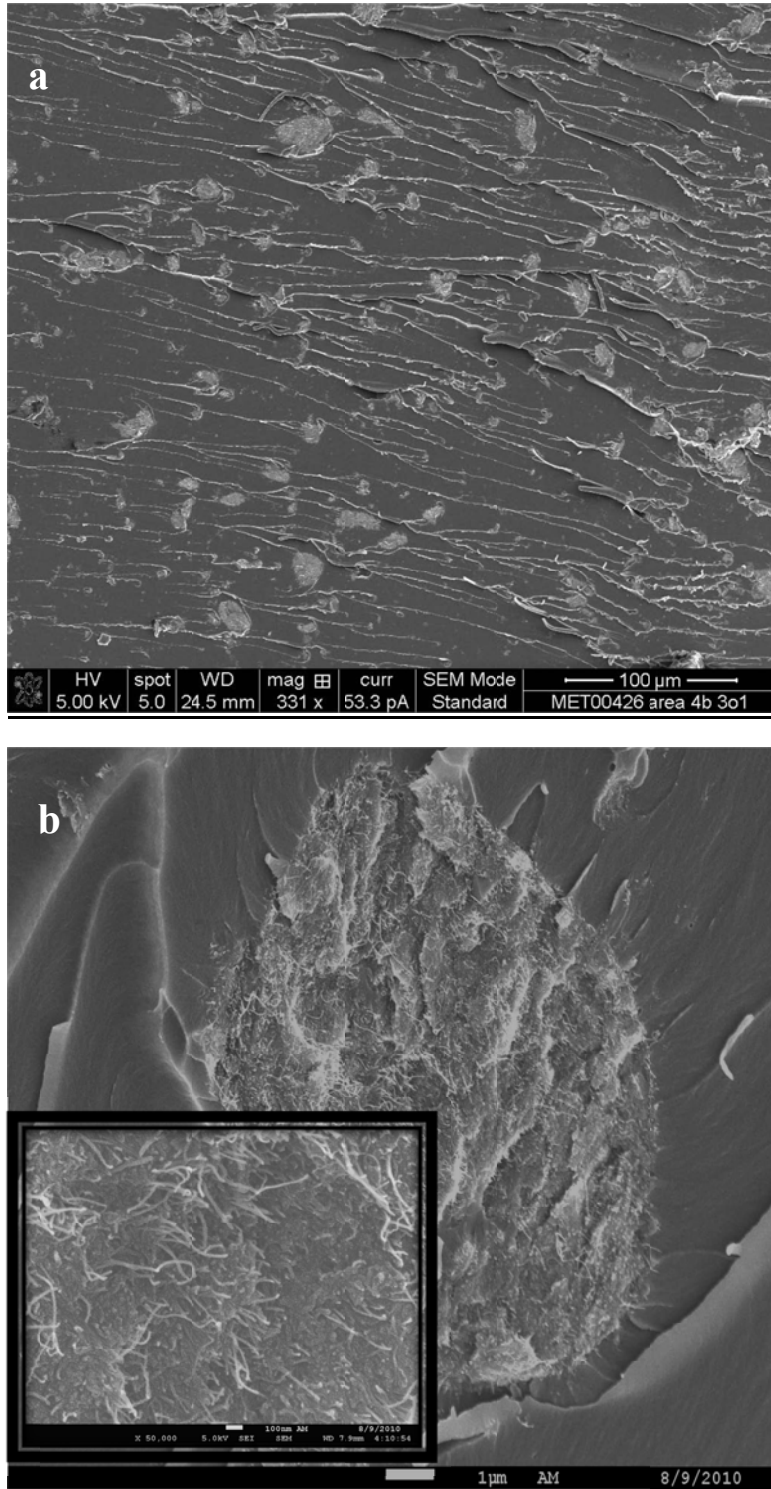


Fig. 2.3. a) SEM micrograph of the fracture surface of the MWCNTs-Aeropoxy composite sample. b) High resolution SEM of one of the agglomerations. Inset: The scale bar is 100 nm.

Following ultrasonication, the CNT-HNO₃ solution was neutralized. The solution was placed in a micro-centrifuge for 2 minutes at 14,000 rpm. The supernatant was decanted and replaced with deionized water. The solution was then placed in a bath ultrasonicator for 5 minutes. This centrifugation and neutralization process was repeated 4 times until a neutral PH was achieved. Finally, the solution was placed in an oven set to 80°C overnight to allow the water to completely evaporate.

The CNTs that were subjected to the acid treatment described above were used to prepare composite samples of which the CNTs accounted for 2% of the total weight. Prior to dispersion, the CNTs were ground with a mortar and pestle as the acid treatment – following evaporation of the water – produced agglomerated chunks of CNTs. The CNTs were then dispersed in Aeropoxy brand PH3665 epoxy hardener by an IKA Ultra-Turrax T-18 Basic shear mixer/dispersion unit. The unit was set to the maximum speed (24000 rpm) and run for 10 minutes at a time for a total of 30 minutes with 2 minute rest periods in between to allow for the cooling bath to be replaced. Next, the CNTs-hardener mixture was then homogenized utilizing a Vibra-Cell VCX 500 tip ultrasonic processor for a total of 30 minutes at amplitude of 40% and a 2 second on/off pulse (the elapsed time was 1 hour). A cooling bath was again employed and changed at 10 minute intervals. Aeropoxy brand PR2032 epoxy resin was then added to the mixture which was briefly stirred by hand. The composite was mixed for 1 minute with the dispersing unit followed by 1 minute of mixing with the ultrasonic processor. All other settings remained the same as before. The composite was then placed under vacuum to remove any air bubbles and allowed to cure overnight. Once cured, the composite samples were post-cured in an oven at 55°C for 18 hours. Nanocomposites of short MWCNTs and SWCNTs were fabricated employing the procedure

described above. Without introducing the CNTs, the hardener and resin were subjected to the same procedure from which the reference neat epoxy samples were fabricated.

A fracture surface of the nanocomposite was coated with gold thin film (4 nm) and investigated under SEM. As shown in Fig. 2.4, MWCNTs were globally dispersed in a satisfactory manner in the polymer matrix with very little amount of agglomeration.

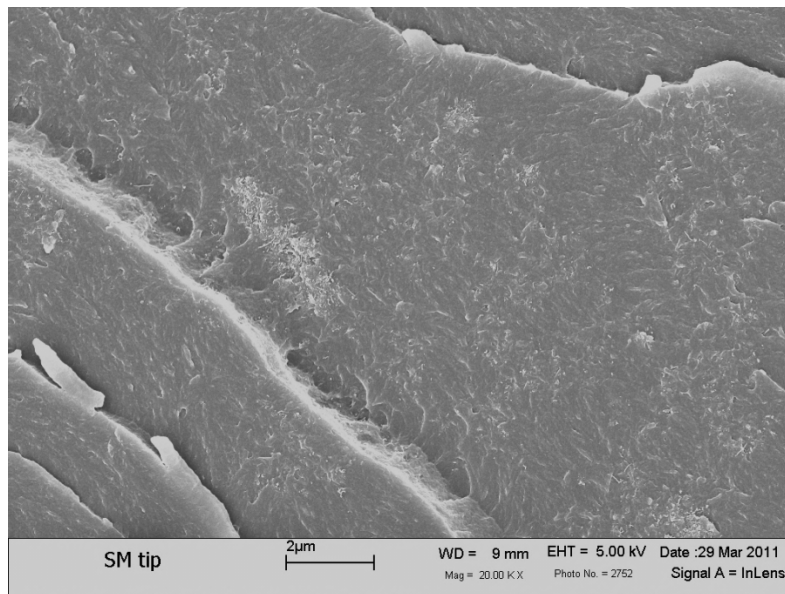


Fig. 2.4. SEM micrograph of the fracture surface of functionalized MWCNTs–epoxy sample

2.4.4 Nanoindentation, nanocreep and nanoimpact tests

A schematic representation of the nanoindenter (NanoTest[®]) that we used is shown in Fig. 2.5. The loading is performed by sending an electrical current to the coil causing the pendulum to rotate about its frictionless pivot so that the indenter penetrates the sample surface. The indenter tip displacement (penetration) is measured during the loading and unloading with a parallel plate capacitor that has sub nanometer theoretical resolution. It should be noted that, the nanoindentation data was corrected for both frame compliance and thermal drift.

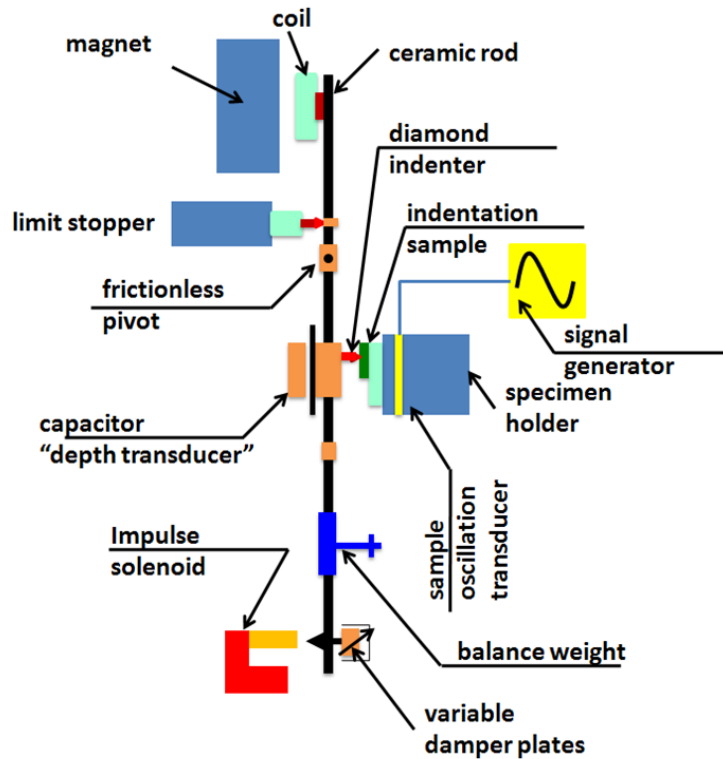


Fig. 2.5. Schematic of the NanoTest 600 mechanical testing system.

The pre-tests on neat epoxy samples revealed that using a 0.08 mN/s loading/unloading rate, and allowing the sample to creep for either 60 seconds or longer times at the maximum indentation load would result in almost the same reduced modulus, whereas having shorter time creeps would drastically change the measured properties. Having a near-linear unloading curve even at high temperatures, where the viscous behavior of the system is more pronounced, manifests the proper choice of dwell time. Moreover, keeping the creep time constant, another set of indentations utilizing different loading/unloading rates were performed. Loading rates slower and faster than 0.08 mN/s caused a non-linear unloading curve and an underestimation of the modulus, respectively.

The NanoTest 600 is equipped with a hot stage indentation module which allows reliable measurements at temperatures as high as 750° C [64, 65]. This module is attainable due to the fact that indentation is performed horizontally and thus allowing the installation of a thermal shield, shown in Fig. 2.6.

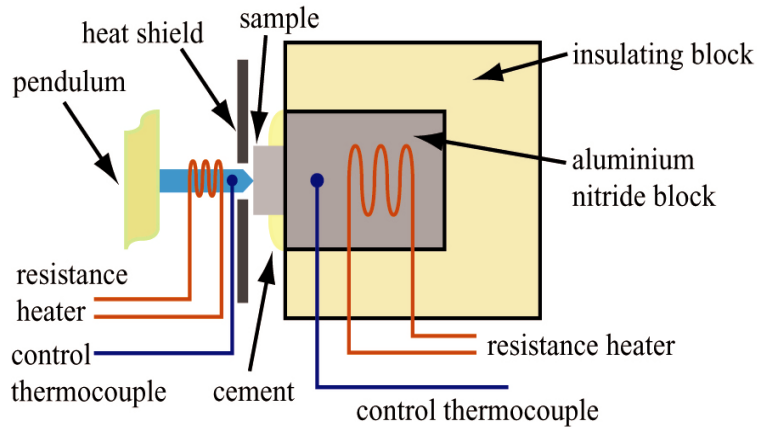


Fig. 2.6. Schematic of the NanoTest hot stage feature (Courtesy of Micro Materials Ltd.)

The heating element only has localized effects so that minimal heat flow and thermal drift occur during indentation at high temperatures. As shown in Fig. 2.6, an aluminum thin shield is placed in front of the pendulum to prevent any thermal interference with the electronics and depth sensing equipment. The indenter and its heater are passed through the thermal shield. The sample is mounted on a ceramic thermal insulator and the heater is embedded inside the thermal insulator block.

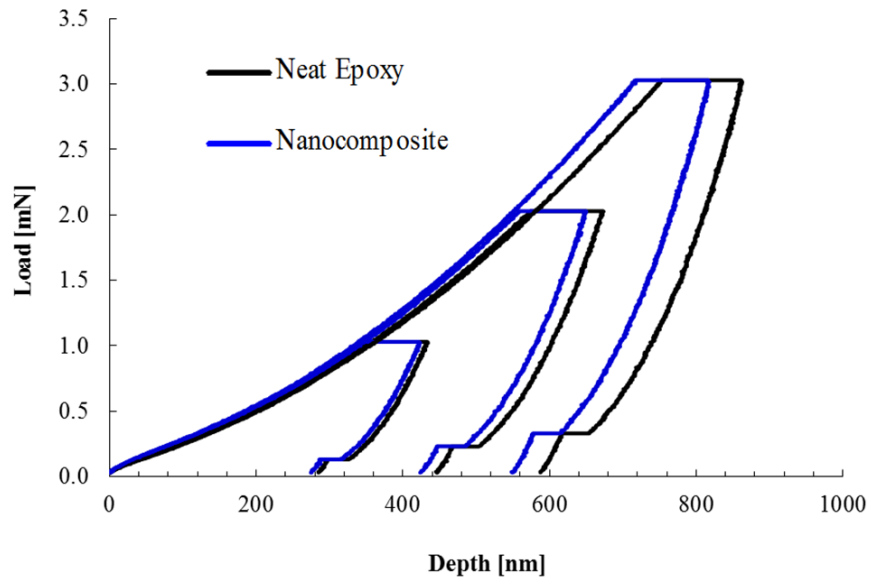


Fig. 2.7. Representative loading and unloading hysteresis for both neat epoxy and MWCNTs-epoxy composite samples at maximum loads of 1, 2 and 3 mN, respectively. Tests were performed at 25 °C.

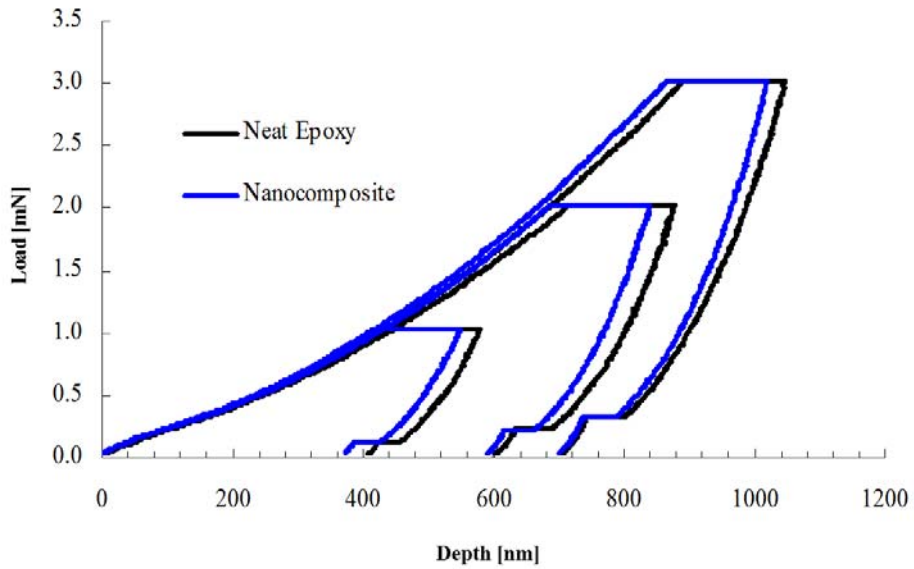


Fig. 2.8. Representative loading and unloading hysteresis for both neat epoxy and MWCNTs-epoxy composite samples at maximum loads of 1, 2 and 3 mN, respectively. Tests were performed at 55 °C.

Two millimeters thick samples were prepared for the elevated temperatures indentation. The glass transition temperature, T_g , of the Aeropoxy was measured in a previous investigation [66] via DMA analysis to be 75.6 °C and upon adding 3% MWCNTs T_g was found to be 70.8 °C. In an elevated temperature indentation both indenter and sample are heated to the preferred temperature then an indentation in conventional way was performed. The samples were tested at 25, 40 and 55°C. Fig. 2.7 and Fig. 2.8 show some representative indentation hysteresis that were performed at 25 and 55 °C at 1, 2 and 3 mN, respectively. Each indentation test was repeated five times and the averaged values of the modulus and hardness were calculated. Although the samples were cured at ambient temperature, they exhibited further curing upon applying the heat. Therefore they were allowed to cure for 4 hours at each elevated temperature prior to any measurement.

Using boron nitride Berkovich tip indentation creep tests for duration of 1800s were carried out at loading rate of 0.08 mN/s and different maximum loads of 1, 2 and 3 mN as shown in Fig. 2.9 and Fig. 2.10 . The Nanoindentation creep tests were performed using the hot stage module under 25, 40 and 55 °C thermal environments. Three nanoindentation creep tests were performed at each load-temperature combination.

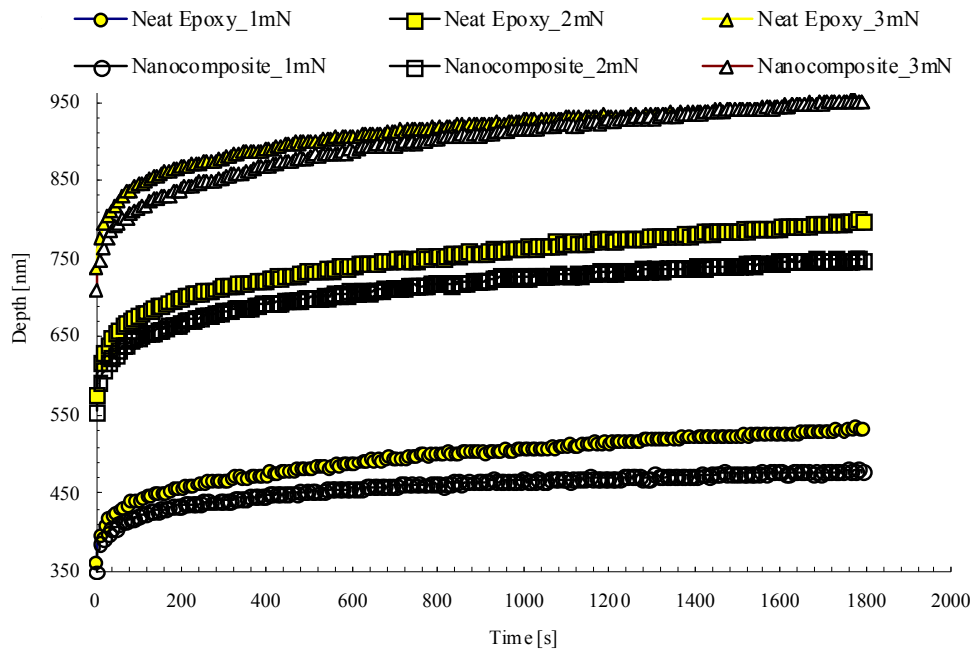


Fig. 2.9. Nanoindentation creep tests of both neat epoxy and nanocomposite samples. Creep was performed at maximum loads of 1, 2 and 3 mN, respectively, at 25 °C.

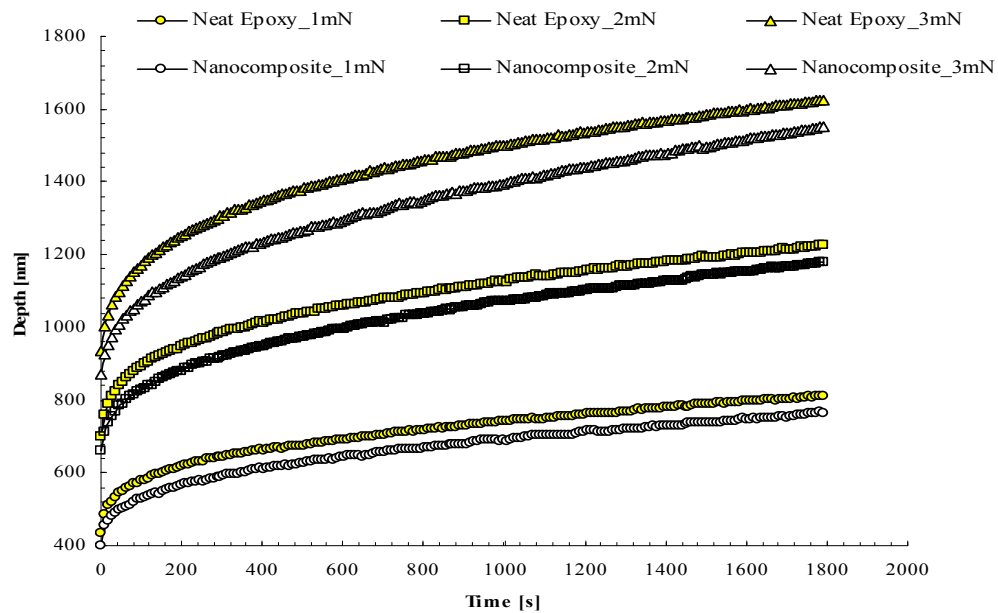


Fig. 2.10. Nanoindentation creep tests of both neat epoxy and nanocomposite samples. Creep was performed at maximum loads of 1, 2 and 3 mN, respectively, at 40 °C.

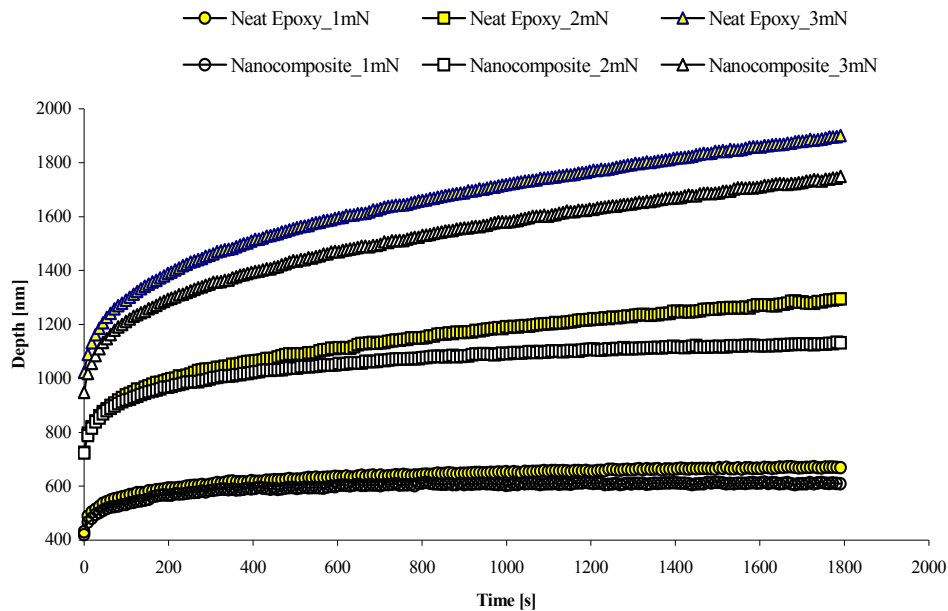


Fig. 2.11. Nanoindentation creep tests of both neat epoxy and nanocomposite samples. Creep was performed at maximum loads of 1, 2 and 3 mN, respectively, at 55 °C.

Nanoimpact tests were performed using a 5 microns radius spherical diamond tip. The tip is accelerated in less than a hundredth of a second from a distance of almost 12 microns to the surface of the sample to produce a load of 5mN. The repetitive impact was performed 45 times in each spot with the diamond probe being two seconds in contact and two seconds off the surface. Measuring the volume change due to initial impact and between the first and last strikes is used as a qualitative metric for energy absorption of different samples. While it is assumed that every impact of the probe into the sample delivers a certain amount of energy, the resistance of the samples to plastically deform under the impact is reported herein as an inverse merit of energy absorption capability of the materials. A total of 10 repetitive nano-impulse tests were carried out on each sample. A representative nanoimpact curve on the surface of the reference sample is

shown in Fig. 2.12. While the first impact only penetrates by almost 1 μm , in a decaying exponential manner consecutive impacts caused an increased penetration depth of up to 6 μm .

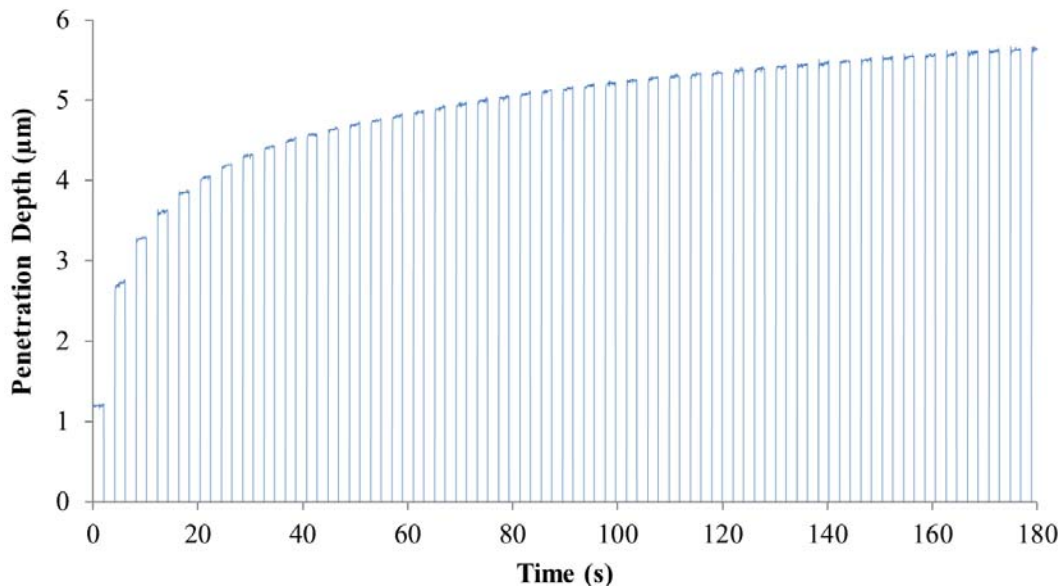


Fig. 2.12. Representative Nanoimpact penetration depth versus time for the reference neat epoxy sample

2.5 Results and discussion

2.5.1 Nanoindentation results

While the Oliver- Pharr method presented by Eqs. (2.4) and (2.6) is robust and directly applicable to elasto-plastic materials, measurements of the mechanical properties for time dependent materials should be carried out with caution. The method tends to overestimate the Young's modulus for polymers. This anomaly usually takes place during the unloading while the displacement does not follow the decaying pace of the load (as seen in metals for example). Rather, due to the time-dependent polymer behavior, the displacement sometimes increases during the initial stages of unloading causing a higher unloading slope and sometimes a negative

slope leading to a higher modulus than the actual value. To relief any excess loading the nano creep test is performed prior to unloading. This test is manifested by the horizontal constant load period (Fig. 2.7 and Fig. 2.8), followed by unloading. The shape of the unloading curves also indicates no negative slopes and thus the possibility of overestimating the modulus is minimal.

The nanoindentation hardness and reduced modulus values together with the data uncertainty analysis are presented in Table 2.2. The coefficient of variability (CV) for each property is mainly the standard deviation divided by the mean value of the property calculated for the results of 5 tests at each load/temperature configuration. One would think of the CV as the normalized measure of dispersion of the data distribution. The table shows that the CV values for the MWCNTS composite are in general higher than those for the neat epoxy which again indicates the non-homogeneous dispersion of the MWCNTs within the epoxy matrix. Also, it might indicate easier elastic recovery for the neat epoxy.

Various materials related effects can cause errors in the estimation of the modulus and hardness such as the pile up of epoxy which might lead the indenter to penetrate less compared to the case where there is no pile up. It is unlikely that the surface inclination or roughness would result in misleading or erroneous results as a great deal of care were taken during the cutting and mounting stages of the samples.

Table 2.2 results indicate that both the hardness and modulus for the neat epoxy and nanocomposite samples are more or less load independent; the variations are within 7%. The slight increase in the modulus at smaller loads (1 mN) is consistent with previous observations that the modulus of polymeric materials increases as the indentation depths reduces [67, 68].

Such behavior can be understood in terms of the induced confined mobility of the interfacial region adjacent to the indenter.

Table 2.2. Nanoindentation and creep nanoindentation results for the neat epoxy and the nanocomposite systems at different load-temperature environments.

	Load (mN)	H(GPa)	%CV	E(GPa)	%CV
Temperature = 25 °C					
Neat Epoxy	1	0.183±0.003	2	4.527±0.044	1
	2	0.178±0.003	2	4.286±0.045	1
	3	0.180±0.002	1	4.265±0.026	0.6
MWCNTs Composite	1	0.193±0.001	1	4.729±0.058	1.2
	2	0.191±0.008	4	4.614±0.309	6.7
	3	0.188±0.001	1	4.463±0.052	1.2
Temperature = 40 °C					
Neat Epoxy	1	0.122±0.002	2	3.443±0.080	2.3
	2	0.120±0.001	1	3.362±0.060	1.8
	3	0.121±0.001	1	3.455±0.083	2.4
MWCNTs Composite	1	0.140±0.005	4	3.94±0.179	4.5
	2	0.137±0.002	2	3.725±0.097	2.6
	3	0.141±0.003	2	3.749±0.108	2.9
Temperature = 55 °C					
Neat Epoxy	1	0.117±0.004	3	3.128±0.048	1.5
	2	0.116±0.003	3	2.950±0.091	3.1
	3	0.118±0.006	5	2.922±0.085	2.9
MWCNTs Composite	1	0.122±0.003	3	3.307±0.082	3.7
	2	0.122±0.006	5	3.378±0.074	2.2
	3	0.131±0.003	2	3.316±0.099	3

The improvements of the modulus and hardness upon adding 3 wt% MWCNTs to the neat epoxy at room temperature are within 5%. The global agglomeration of MWCNTs observed in Fig. 2.3 can be attributed to these moderate improvements. It is not uncommon that the addition of CNTs to epoxy will not follow the mixture rule in terms of improving the properties due to agglomeration and poor dispersion [43, 52]. The minute variations of the properties with the indentation loads (and thus the indentation depths) indicate local homogeneity in the samples.

It is clear that both materials systems show significant degradations in the mechanical properties at elevated temperatures. For example, at 55 °C the neat epoxy tested at 1 mN undergoes a 30% reduction in modulus and 36% reduction in its hardness compared to the room temperature results. The reductions in the modulus and hardness under the elevated temperatures for the nanocomposite system with 3 wt% MWCNTs are similar to those of epoxy results. However, it is evident that adding 3 wt% MWCNTs to the epoxy system increased both the hardness and modulus even at higher temperatures. For example at 40 °C the improvements in hardness and modulus are as high as 15% compared to the neat epoxy values.

Fig. 2.7 and Fig. 2.8 further illustrate the effect of elevated temperatures on the nanoindentation behavior of the two materials systems. The indentation response changed dramatically between 25 and 55 °C for both the neat epoxy and the nanocomposite samples. Both samples encountered softening at 55°C evident by the increased total and the contact depths.

2.5.2 *Nanocreep results*

Using Eq. (2.10) the creep compliances for 30 minutes creep tests were calculated and the results are shown in Fig. 2.13 and Fig. 2.15. As anticipated, for both the neat epoxy and the

nanocomposite systems, the contact creep compliance increased at higher nanoindentation maximum loads. Fig. 2.13 shows the typical variation of $J(t)$ with P_0 values of 1 and 3 mN, respectively, at 25°C. By tripling the value of the maximum load, from 1 to 3 mN, creep compliance for the neat epoxy sample increased by 15% by the end of the 30 minutes creep duration. Adding the MWCNTs to the epoxy system suppressed such increase in the creep compliance as suggested by Fig. 2.13. Increasing the P_0 from 1 mN to 3 mN only yielded 5% increase in the creep compliance of the nanocomposite system after 30 minutes of creep.

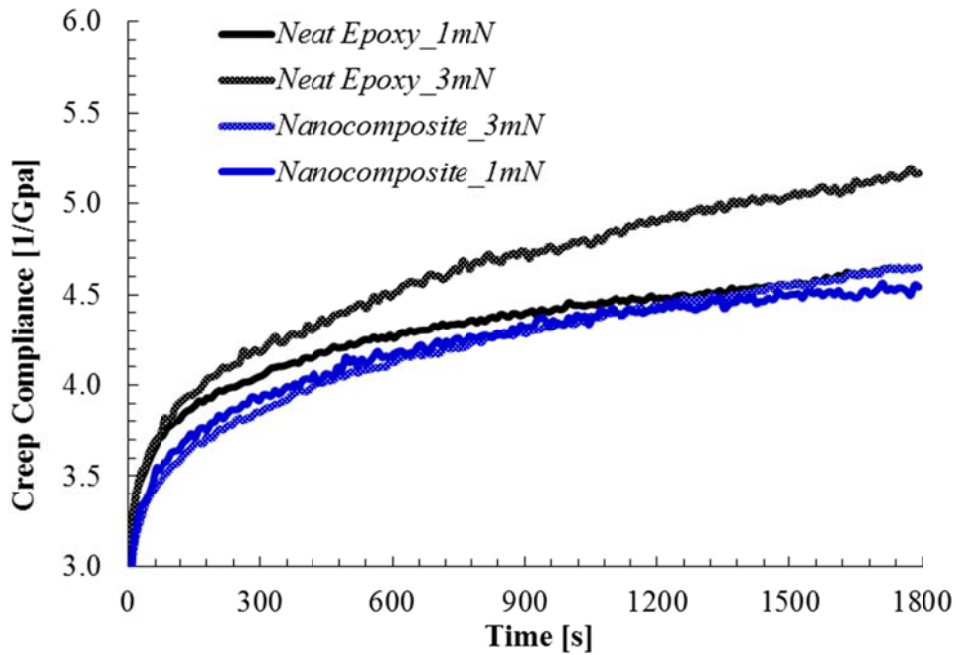


Fig. 2.13. Contact creep compliance for neat epoxy and nanocomposite systems at 25 °C.

At 40 °C, the epoxy starts to exhibit significant increase in $J(t)$ as shown in Fig. 2.14. In comparison to the 25 °C results, the values of the creep compliance by the end of the creep test increased almost by more than 100% for the neat epoxy system regardless of the maximum load

at which the creep was conducted. This trend was observed as well for the nanocomposite system however the nanocomposite systems maintained a lower compliance compared to the neat epoxy.

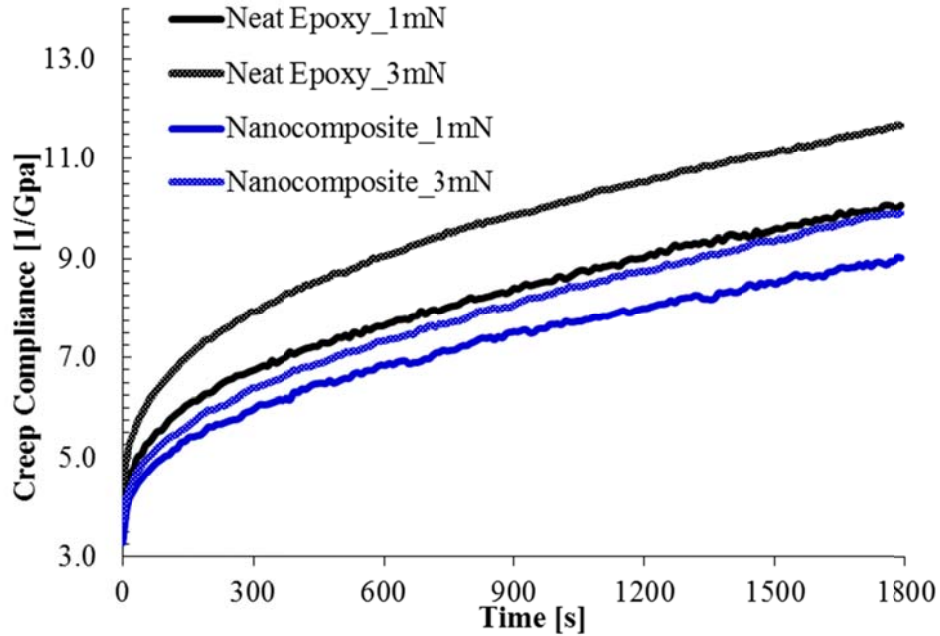


Fig. 2.14. Contact creep compliance for neat epoxy and nanocomposite systems at 40 °C.

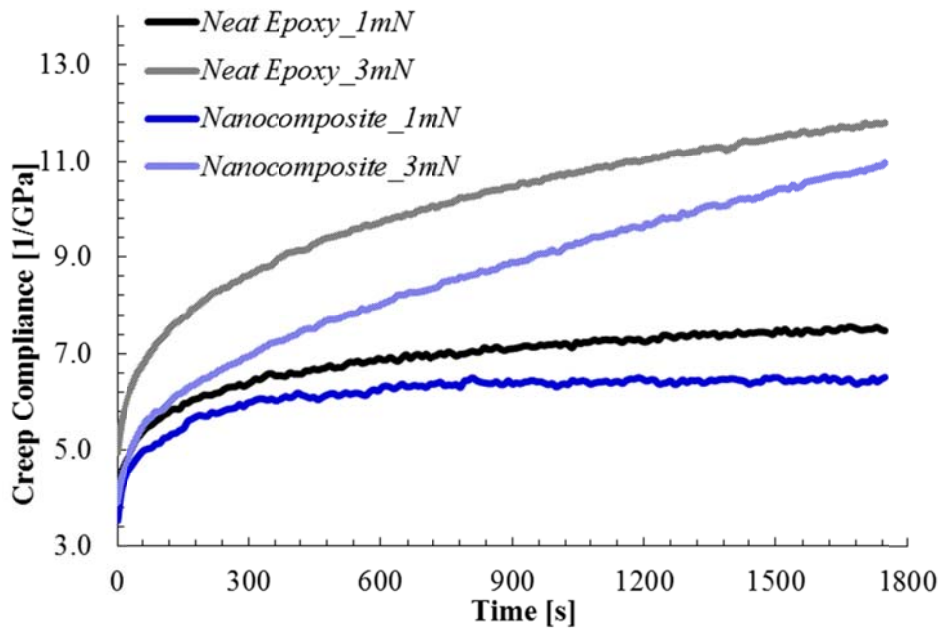


Fig. 2.15. Contact creep compliance for neat epoxy and nanocomposite systems at 55 °C.

At 55 °C both the neat epoxy and nanocomposite exhibited much higher degree of time-dependent behavior under 3 mN constant creep loading as compared to their compliances at 25 °C. This shift in behavior occurs below the measured T_g of both materials systems, indicating softening. However, at a lower load of 1 mN, $J(t)$ for the nanocomposite and the neat epoxy are still higher than that measured at 25 °C, but lower than the compliances measured at 40 °C. This behavior might suggest that the molecular mobility of the neat epoxy and the matrix epoxy in the nanocomposite near the surface is not as pronounced as for larger volumes (depths). At temperatures near T_g the degree of anisotropy increases within constrained areas of the epoxy and nanocomposite networks.

Despite the fact that the linear viscoelastic relation might not be applicable for the Berkovich indenters, they were used by different research groups at both small values of loads, 0.5 mN, [57] and higher loads of 20 mN [58]. In the current investigation the tips available for hot stage indentation are made of Boron Nitride which is very difficult to be shaped into a spherical tip, therefore, a Berkovich tip was used instead.

Furthermore, adding 3 wt% MWCNTs, regardless of the creep maximum load, always resulted in a smaller contact creep compliance compared to that for the neat epoxy samples. The influence of MWCNTs can be inferred in terms of adding a degree of crystallinity to an amorphous epoxy. The presence of MWCNTs in the epoxy matrix could catalyze chain scission, resulting in reduction of average chain length and thus a decrease in both creep rate and glass transition temperature [66].

The ability of the MWCNTs additives to increase creep resistance, manifested by the creep life time prolongation and creep rate reduction, can be attributed to several factors. The confinement effect of the highly elastic MWCNTs nanofillers has prevented the deformation of the epoxy network. The CNTs act as sites, blocking the movement of the epoxy chains when subjected to an external indentation force, hence, they restrict the viscous flow of the amorphous epoxy. Regardless of the nature of the loading (tensile, shear, etc.), it is well known that ensuring a good load transfer between the epoxy matrix and the MWCNTs will give rise to good creep resistance of the nanocomposite as a whole.

The enhancement in creep resistance can also be related to several nano effects of the MWCNTs such as their high aspect ratio (25-100 for the current MWCNTs) and large interfacial area which contributes to significant interface adhesion between the CNTs and the epoxy matrix and thus improves the load transfer [69]. This explanation holds at low creep load levels (1 mN) at which the interfacial bonding between the MWCNTs and the epoxy chains holds and the nanotubes form an infiltrating network of cross linking elements. This network interconnects the epoxy chains, thus increases the cross linking density and restricts the mobility of the epoxy chains under nanoindentation mechanical loading. At higher load levels (3 mN) the nanotubes/epoxy interface is likely to fail and consequently the nanotubes ability to slow the chains motion is negated [43]. Similar observations were reported by other investigators [70].

The higher temperature environments increased the contact creep compliance for both epoxy and composite systems, Moreover, the contact creep compliance curves of Fig. 2.13, Fig. 2.14, and Fig. 2.15 strongly suggest that there is a correlation between the temperature, approaching the glass transition (75.6 °C for neat epoxy and 70.8 °C for the nanocomposite), and the increase in

creep rate. In general, the epoxy and nanocomposite samples that were allowed to creep at a temperature closer to T_g showed more pronounced power law behavior.

At elevated temperatures the chains mobility of the matrix will predominates the creep of the nanocomposite. The presence of MWCNTs will initiate Van der Waals bonding leading to polymer chains entanglement around the CNTs. This phenomenon limits the chains mobility at higher temperatures (e.g. 40 and 55 °C). Furthermore, MWCNTs possess an inherent ability to reduce the thermal expansion coefficient of the nanocomposite due to their large heat capacity. Therefore, the application of external thermal energy and the heat absorption by the MWCNTs will determine the level of activation energy necessary to facilitate the epoxy chains mobility in the nanocomposite. In the present investigation the glass transition temperature drops from 75.6 to 70.8 °C upon adding 3 wt% MWCNTs to the neat epoxy. The T_g reduction indicates that the activation energy needed for the chains mobility is increased in the case of the nanocomposite as the MWCNTs will absorb part of the applied heat due to their exceptional thermal conductivity; 2000 W. m⁻¹.k⁻¹ at room temperature [70].

MWCNTs ability to reduce the creep is observed even under high temperature conditions. However, the increase in the creep compliance for the nanocomposites at higher temperatures indicates that the MWCNTs-epoxy interfaces are weakened significantly by increasing the temperature. Consequently, the ability of MWCNTs cross linking to limit the epoxy chains deformation is adversely affected by temperature.

2.5.3 Nanoimpact results

The results for the high strain density energy nanoimpact tests on neat, MWCNTs, and SWCNTs epoxy systems are tabulated in Table 2.3. The crate volume is the permanently deformed volume of the sample under the indenter. The crate volume change due to the first impact and also the crate volume change as a result of repetitive impacts (first impact crate volume subtracted from the final crate volume) are both stated in Table 2.3. According to the nanoimpact measurements, both nanocomposite systems retain almost identical impact energy absorption values. The improvements in the crate volume change due to the first impact and the repetitive impact of the nanocomposites compared to the neat sample are 18.5% and 41%, respectively. The impact energy dissipation mechanisms are frictional sliding of the nanotube/epoxy interface, CNT pulling-out, and deformation the toughened matrix. The capability of the CNTs to toughen the matrix is significant noting that the CNTs only account for 2 wt% of the nanocomposites.

Table 2.3. Impact penetration depths and crate volume changes for the neat epoxy and nanocomposites based on SWCNTs and MWCNTs

	First impact depth (μm)	Final repetitive impact Depth (μm)	First impact crate volume change (μm^3)	Repetitive impact crate volume change (μm^3)
Neat epoxy	1.12 \pm 0.05	5.52 \pm 0.11	135 \pm 6	746 \pm 20
MWCNTs nanocomposite	0.97 \pm 0.05	3.70 \pm 0.06	116 \pm 6	433 \pm 13
SWCNTs nanocomposite	0.91 \pm 0.06	3.73 \pm 0.12	106 \pm 8	449 \pm 18
Average improvement of the nanocomposites With respect to the Neat epoxy (%)			18.5	41

2.6 Conclusions

Instrumented nanoindentation is a valuable tool to evaluate both the mechanical and time-dependent properties for epoxies and their nanocomposites made using MWCNTs. The addition of 3 wt% MWCNTs improved both the modulus and the hardness of the neat epoxy. The improvements in the properties were not as high as anticipated through the use of mixture rule, indicating insufficient dispersion. The slight change of properties with load (depth) also emphasizes the homogeneity of the samples. While both the neat epoxy and the nanocomposite systems were undergone degradation in their properties at elevated temperatures, the nanocomposite sample retained better mechanical properties compared to the neat epoxy.

The comparison of the time-displacement data under constant indentation creep load indicates that the addition of MWCNTs results in a noticeable decrease in creep rate, particularly under the conditions of elevated temperature and high nanoindentation creep load. For larger nanoindentation creep load (3mN) the creep resistance induced by the addition of MWCNTs is reduced. This behavior might indicate a failure of the epoxy-MWCNTs interface at high load levels. However, increasing the temperature to a near glass transition did not impact the ability of the MWCNTs to reduce the creep response of the nanocomposites compared to neat epoxy samples.

Furthermore, the energy absorption capability of the nanocomposites was significantly enhanced due to the presence and CNTs and their interaction with the surrounding cross-linked polymer. The nanoimpact produces strain energy densities similar to those encountered in high velocity macro-scale impact tests and hence is a very dependable technique for characterizing nanocomposites impact performance.

Based on the finding of this chapter one would hypothesize that FRPs based on carbon fibers and epoxy matrix enriched with CNTs would inherit some of the improvements in the mechanical properties for the mere presence of the CNTs. The next chapter is focused on fabricating and characterizing hybrid composites based on carbon fibers/epoxy/CNTs toward validating this hypothesis.

Chapter 3. Mechanical Characterization and Impact Damage Assessment of a Woven Carbon Fiber Reinforced Carbon Nanotube-Epoxy Composite

3.1 Overview

Carbon nanotubes carry the promise of enhancing the poor out-of-plane mechanical performance of fiber reinforced polymer composites (FRPs). This part of the dissertation is aimed to investigate the effect of adding multi-walled carbon nanotubes (MWCNTs) to the epoxy matrix of a carbon fiber reinforced composite (CFRP) on the composites damping performance, impact resistance and impact damage progression. Two sets of CFRPs with their corresponding matrices comprising MWCNTs-epoxy and neat epoxy, respectively, were fabricated and mechanically tested under tensile, shear punch, vibration and intermediate velocity impact (IVI) environments. Dynamic mechanical analysis (DMA) was employed to measure the damping performance of the two composite systems. The samples were subjected to out-of-plane impact (at $\sim 100 \text{ ms}^{-1}$) from which the energy dissipation capacity of the composites was evaluated. The shear punch test provided invaluable information on the damage mechanics of the ballistic impact of the composite panels. It also contrasted the effect of high-strain-rate on the impact test. The consequences of adding MWCNTs to the matrix of CFRPs on the impact progressive damage and energy absorption is discussed in terms of the damage mechanisms and the dynamic damping behavior of the composites. To better comprehend the effect of adding CNTs on the impact damage mechanisms, X-ray radiography of the impacted panels is performed.

3.2 Introduction

A great body of research has been devoted to improving the through-thickness properties of FRPs [71, 72]. Improvements in the interlaminar properties of FRPs was achieved via different approaches such as stitching [71], braiding [73], fiber surface treatment [74] and interleaving with toughened polymers [75]. However, these enhancements are achieved at the cost of inadequate in-plane mechanical properties. On the other hand, utilizing nanomaterials as nanoscale reinforcements [76, 77] offers the opportunity to enrich the fiber-matrix interface and matrix dependent properties of FRPs with minimal weight penalty.

The extraordinary mechanical, electrical, and thermal properties of carbon nanotubes (CNTs) have motivated researches to utilize them as a filler phase in composite materials in order to improve the properties of the host matrix. The strength, elastic modulus and the fracture properties of CNTs are orders of magnitudes higher than most common composites used in civilian and military applications [10]. Moreover, CNTs reinforcements increase the toughness of polymer matrices enabling them to absorb higher impact energies.

To benefit from the remarkable properties of both CFRPs and CNTs, multiscale three-phase carbon fiber-carbon nanotube reinforced polymer composites were established by several research groups [3, 72]. Several methodologies for integrating CNTs into FRPs have been investigated; grafting, attachment or growth of CNTs on the fibers [19], spraying of CNTs on prepregs [78], electrophoretic deposition of CNTs on fabrics [79], addition of CNTs to the polymer sizing formulation of fibers [80], and dispersing the CNTs in the polymer matrix. Among all these approaches, mixing CNTs with the matrix in a composite is, to date, the most facile and economically-compatible route.

Much interest has been directed to examining the impact strength of hybrid CNTs-FRP composites. Soliman et al. [15, 81] incorporated pristine and functionalized CNTs by dispersing them into the matrix polymer of a CFRP and showed improvement in the matrix-dominated properties such as the interlaminar shear strength (ILSS) and low-velocity transverse impact resistance. Functionalized CNTs have been shown to produce even higher ILSS and impact resistance than pristine CNTs due to stronger interfacial bonding between the CNTs and the matrix. In an experimental study by Inam et al. [82], the addition of 0.1 wt% CNTs to the matrix of a glass fiber reinforced composite improved the absorbed impact energy by 6% and the Mode-I interlaminar toughness was reduced by 23%. The effect of a higher loading of CNTs (i.e., 0.5 wt%) on the impact properties of a CFRP was studied by Kostopoulos et al. [83]. They showed for low impact energies of 2-8 Joules, no significant effects on energy absorption and the delamination area were observed. However, at higher impact energies of 12-20 Joules moderate improvement on the absorbed energy was reported. Moreover, the delamination area for the CNTs reinforced FRPs was less than that for composites with no CNTs. Safdari and Al-Haik [84] showed—computationally—that the addition of CNTs to the polymer matrix of a laminated FRP can significantly increase the impact resistance of the composite. Grujicic et al. [85, 86] reported improvement on the impact resistance of CNTs-epoxy matrix composite reinforced with E-glass fiber mats as a result of adding a multi-walled carbon nanotubes (MWCNTs) layer sandwiched in-between the lamina. Improvements in the out-of plane mechanical properties of the CNTs comprising FRPs could be attributed to (i) the additional energy required for pulling-out or rupturing of the CNTs, (ii) CNT toughened matrix, and (iii) stronger fiber-matrix adhesion as a result of the CNTs addition.

Vibration attenuation of FRPs is another active field of research targeting FRPs with enhanced damping for various applications such as impact energy dissipation. Impact energy can be dissipated through damping provided by the viscoelastic constituents of the CFRP as well as by the frictional sliding at the interface of filler-matrix [87]. Therefore, incorporating CNTs into FRPs can significantly improve their damping performance. Koratkar et al [88] reported a 1150% increase in the damping of the composites based on 2.0 wt% oxidized single-walled carbon nanotubes (SWCNTs) compared to the neat polycarbonate matrix. In a recent study, Venkatanarayanan et al. [89] characterized the non-ballistic intermediate velocity impact energy absorption and vibration damping response of a glass fiber reinforced hybrid composite based on MWCNTs-epoxy matrix. They concluded that the addition of 0.1 wt% MWCNTs significantly increases the shock wave damping characteristics of the panels. In another study, Khan et al. [90] showed that the damping ratio of both nanocomposites and CFRPs based on MWCNTs increases with increasing the CNTs content. They concluded that the vibration damping is attributed to sliding at the CNTs-matrix interfaces and the enhanced damping of the CFRP-MWCNTs composite is mainly due to the CNTs toughened matrix. The vibration energy dissipation in composites comprising CNTs arises from the weak bonding and interfacial friction of the nanotubes with the matrix [38, 91]. Due to the high surface area of CNTs, the interfacial sliding has a significant impact on the total damping performance of the composite.

Designing composite structures with high impact resistance requires knowledge of both damping characteristics and progressive damage mechanics during an impact phenomenon. While the damping performance can be simply assessed via dynamic mechanical analysis (DMA), one widely utilized technique to predict the impact progressive damage mechanisms of composites is

the shear punch test. This test can be thought of as the quasi-static analogy of a ballistic impact where the impactor punctures the composite panel. It is argued that the damage mechanisms due to ballistic impact and shear punch tests are identical [92]. Several investigations attempted to predict the impact resistances of thick composite panels from quasi-static shear punch tests (QSSPTs) [92-94].

In general, the dominant failure mechanisms in composite laminates subjected to impact loading are a complex combination of energy absorption mechanisms such as delamination predominantly caused by mode II shear, matrix cracking caused by transverse shear, and translaminar fracture due to fiber fracture and kinking [95]. The mechanical properties of the fiber and matrix, particularly the failure strains, interface properties, fiber configuration and stacking sequence in angle-ply laminates play important roles in determining the impact damage resistance of composites [96, 97]. During an impact or shear punch test, the major energy dissipation mechanisms of FRPs are fiber breakage, delamination, and matrix cracking. While the fiber endurance to fracture is mostly controlled by the fiber properties, the delamination and matrix cracking that are matrix dominated properties can be enhanced by adding CNTs to the matrix.

This chapter delineates, experimentally, the mechanical behavior of CFRP-MWCNTs composites as well as reference neat CFRPs under tension, QSSPT, DMA, and intermediate velocity impact environments. The findings of this chapter elucidate the quasi-static and dynamical behavior as well as impact mitigation performance of hybrid CFRPs containing 2.0 wt% of MWCNTs. In addition, the impact damage progression in CFRPs with and without CNTs is discussed in light of the shear punch tests. The study also attempts to correlate the quasi-static

and the DMA test results to the impact energy absorption of CFRPs based on the MWCNT-epoxy matrix.

3.3 Material and methods

Commercial high strength Polyacrylonitrile (PAN)-based plain-woven carbon fabric in 3,000 filament count tows (HexTow AS2C supplied by HEXCEL Inc.) was utilized as the prime reinforcement. The chosen matrix material was Aeropoxy™ manufactured by PTM&W Industries, Inc. Aeropoxy is a medium viscosity, unfilled, light amber laminating resin that is designed for structural production applications. This resin, brand name PR2032, laminates very easily and wets out fiberglass, carbon and aramid fibers readily. As recommended by the manufacturer, PR2032 mixed with PH3665 hardener cures at 65 °C in 4 hours. The authors have used this epoxy system to manufacture both FRPs [62, 63] and nanocomposites based on SWCNT [13] and MWCNT [47].

Short MWCNTs (0.5-2.0 microns) from Cheaptubes, Inc., with a purity of 95 wt% and an average diameter of 8 nm were utilized as the nanofillers. The MWCNTs accounted for 2.0% of the total weight of the matrix. The CNTs were dispersed in the PH3665 epoxy hardener by an IKA Ultra-Turrax T-18 basic shear mixer-dispersion unit. The unit was set to the maximum speed (24,000 rpm) and run for 30 minutes. Next, the CNTs-hardener mixture was homogenized via a Vibra-Cell VCX 500 tip ultrasonic processor for a total of 30 minutes at amplitude of 40% and a two second on-off pulse (the elapsed time was 1 hour). The PR2032 epoxy resin was then added to the mixture and was briefly stirred manually. The slurry was mixed for 1 minute with the dispersing unit followed by 1 minute of mixing with the ultrasonic processor. This mixture constituted the matrix used to fabricate CFRPs with CNTs-enhanced epoxy matrix. Without

introducing the CNTs, the hardener and resin were subjected to the same procedure from which the reference samples with neat epoxy matrix were produced. To assess the degree of CNTs dispersion, small amount of the hardener-MWCNT-resin mixture was poured into a plastic container and cured overnight at room temperature.

For the purpose of mechanical testing, a set of flat five-layer laminates of 12.5×12.5 cm were manufactured using vacuum and press-assisted hand lay-up process. After 4 hours curing at 65 °C the composites panels were removed out of the mold and were left at room temperature overnight for full curing. The specimens were prepared following the ASTM standards for DMA (D4065, D790) and tension (D3039, D3039M-08) tests. For DMA, strips of approximately 4.0×1.0 cm with a thickness of 0.5 mm were cut from the FRP panels and were tested using a 2.00 cm span three-point bending clamp. Abraded G-10 tabs were bonded to the ends of the tensile specimens using the same resin (i.e. Aeropoxy). The tensile test coupons of 12.5cm×1.3 cm were cut using a saw. Without any further tailoring, other panels were subjected to impact testing, whereas cut squares of 4.0×4.0 cm² were used for the shear punch test.

DMA tests were performed using a DMA Q800 (TA Instruments, Inc.) at ambient temperature. A frequency sweep over the range of 1-52 Hz was carried out from which the loss tangent and storage modulus values were extracted. The DMA measurements were performed at a low constant strain level of 0.1%. The DMA tests were performed on six samples from the two different FRPs configuration. The tensile strength, Young's modulus, and the strain to failure for the specimens were measured from the tension tests utilizing an Instron® 4400R frame. The tensile tests were performed under constant cross head speed of 2.00 mm/min until failure

occurred. Strains up to the failure were recorded via an extensometer. To determine the tensile properties, a total of ten samples for each configuration were tested.

To conduct the impact tests, an in-house designed small single stage gas gun capable of projecting a 17 g impactor at speeds up to 500 ms^{-1} was utilized [98]. Each composite panel was impacted using a 1.27 cm alloyed steel ball-bearing with a weight of approximately 8.4 grams. A 1.30 cm drill-bit was used to create holes in a polycarbonate sabot, in which the impactor was placed. As schemed in Fig. 3.1, purified nitrogen gas (A) fills a reservoir (C) through a hand-operated needle valve (B) to a desired pressure. Once the trigger mechanism (D) is opened, the projectile is pushed through the barrel (E), and the sabot is stripped off via a stripper plate at the muzzle. The impactor impacts the specimen (F), and stops inside a steel containment trap (G).

The trajectory of the projectile was captured through a high-speed camera. The trigger for the camera was activated using a laser-photodiode pair. The output of the photodiode is connected to an operational amplifier, then a voltage comparator so that the photodiode output is converted into a digital signal. The high-speed camera equipped with a wide lens was operated at 30,000 frames per second and a shutter speed of $9.6 \mu\text{s}$. The images captured by the camera were subsequently analyzed to calculate the incident and residual velocities of the impactor.

While extending the boundaries of the sample away from the center of the impact lessens the role of the boundary condition in the test, a large specimen size is required. However, for testing stiff composite panels at high impact velocity of 100 m.s^{-1} , it was observed that the perforation and damage are very local phenomena and are almost not affected by the far field boundary conditions. Square panels with edge length of 12.5 cm were sandwiched within a frame fixture

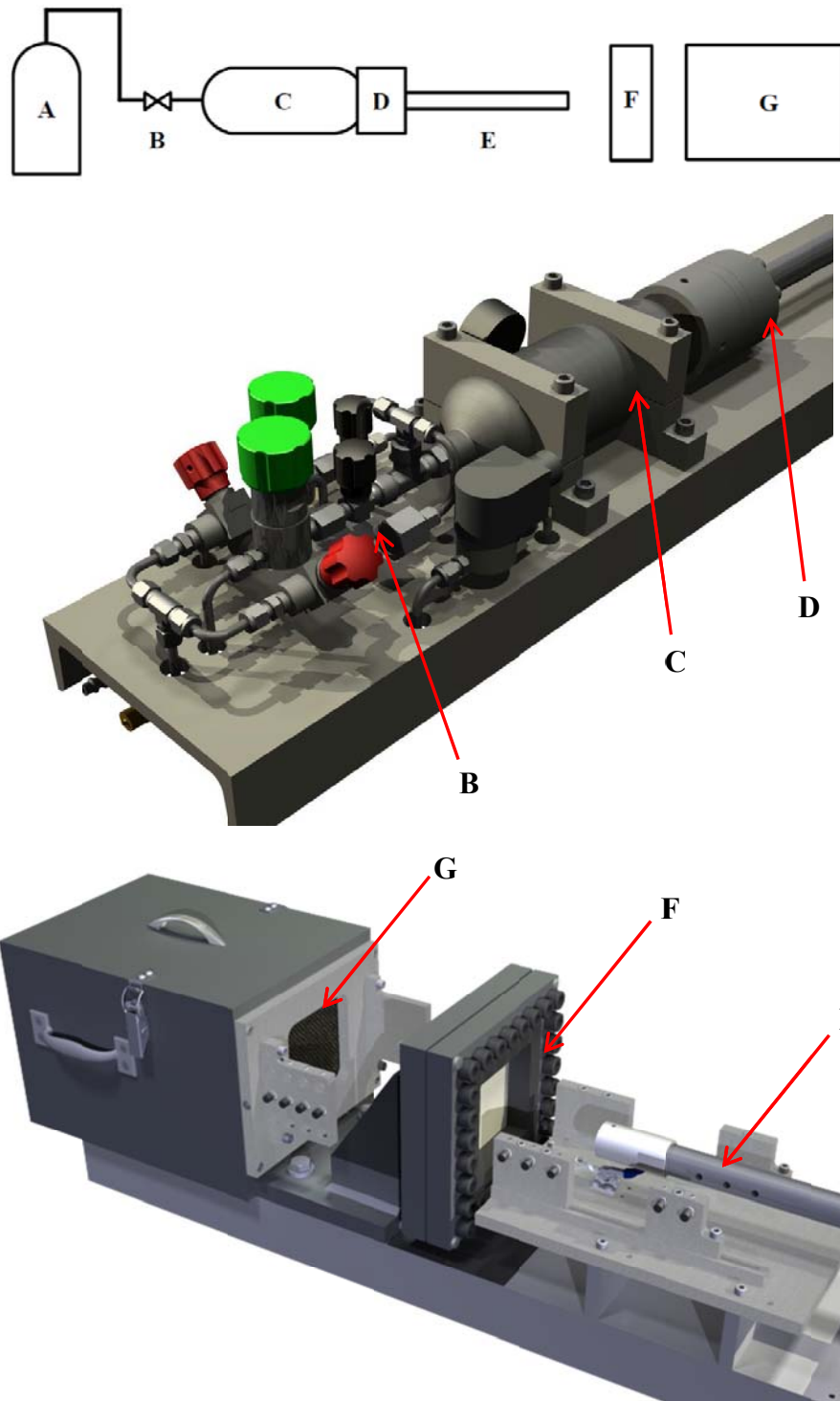


Fig. 3.1. Schematic of the gas gun setup

made of two 2.54 cm thick steel plates. Using simple bolt calculations and a bolt torque of 80 N.m, a clamping pressure of approximately 37.0 MPa was applied to the panel edges.

The samples were shot with impactors at velocities ranging from 90-110 m.s⁻¹ and the absorbed kinetic energy during the impact was calculated from the incident and residual velocities. An image processing code was developed in MATLAB® to track the centroid of the impactor during the impact experiment. The image processing allowed for measuring the impactor speed with a high accuracy. As shown in Fig. 3.2, the impactor images acquired at 30,000 frames per second are well-defined and the image processing allowed for accurate tracking of the centroid of the spherical impactor. Four samples for each FRP configuration were tested for the impact energy absorption measurements.



Fig. 3.2. The impactor captured at 30,000 frames per second rate a) before and b) after the impact. c) image processed cumulative images used for calculating the residual velocity

To better apprehend the damage progression and the energy absorption mechanisms of the ballistic impact, the quasi-static shear punch tests were also carried out. The test fixture was installed horizontally in a screw- driven tensile testing machine. Shear punch test embraces clamping the specimen along its edges while a punch transversely penetrates the panel. A hardened flat head steel punch (19.00 mm diameter) and a hemispherical punch of diameter

12.70 mm (identical to the spherical impactor used during the impact tests) were utilized to punch the samples (see Fig. 3.3). The punch was positioned in the center hole of a jig that clamps down $4.0 \times 4.0 \text{ cm}^2$ samples. A soft steel plate that clamps to the testing machine crosshead exerts force to the punch. The punch then is driven vertically downward through the specimen while the crosshead position and load on the impactor are measured in-situ via a data acquisition system. The fixture exposed an unclamped 19.05 mm diameter circular area of the sample for the punch to shear, while the edges were firmly clamped under a pressure of 30 MPa to avoid any slippage.

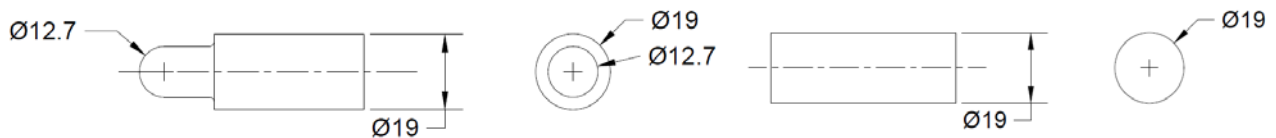


Fig. 3.3. Hemispherical (left) and flat cylindrical (right) punches used in the shear punch study (all measurements are in mm)

X-ray radiography was employed to evaluate the matrix cracking and delamination in the impacted panels. The panels were immersed for 10 minutes in a radio opaque chemical (50 gr Sodium Iodide, 10 mL Ethanol, 10 mL Kodak Photo-Flo 200, and 10 mL distilled water). The solution penetrated through the matrix cracks and the delaminated interfaces. The excess chemical was wiped off the panels' surfaces and the samples were exposed to X-rays (Shimadzu YSF-12 X-ray system). Radiations passing through the sample were recorded on a standard X-ray film.

A fractured surface of the cast MWCNTs-nanocomposite was investigated under field emission scanning electron microscope (FESEM). Since the MWCNTs-epoxy slurry attains high viscosity, it is crucial to ensure the matrix is impregnated in between the tows. Hence, thin slices were cut

from both the hybrid and the reference CFRP samples using a diamond saw and the cut cross-sections were gold-coated and examined under the FESEM.

A LEO (Zeiss) 1550 FESEM operated at 5 kV was utilized to examine the fractured surface of the nanocomposite and the cross sections of the composite samples.

3.4 Results and discussion

Dispersion and homogenization of the MWCNTs through extensive shear mixing and sonication, respectively, resulted in a satisfactory global dispersion, whilst slight local agglomerations were observed (see Fig. 3.4-a and b). The fractured surface shown in Fig. 3.4-b reveals the individualization of MWCNTs bundles.

Cross sectional micrographs of the CFRPs with and without the MWCNTs are shown in Fig. 3.5. It is observed that the matrix entirely infused in between the fibers and impregnated them. However, compared to the reference neat epoxy sample, few voids exist in the MWCNTs enriched matrix. This is due to the high MWCNTs loadings (i.e., more than 2.0 wt%) that lead to an excessively viscous mixture that does not wet and/or impregnate the fibers and, hence, when subjecting the composite to in-plane displacements, stresses will not be effectively transferred to the fibers and the overall structural performance of the composite will be compromised.

As shown in Fig. 3.6, both composite systems demonstrated a brittle tensile behavior and did not undergo significant plastic deformation. The tensile curve for the composite comprising MWCNTs deviates from the elastic behavior and exhibits a nonlinear deformation. This effect can be attributed to the failure of the MWCNTs-polymer interface and the pull-out and rupture of the MWCNTs due to extensive shear stresses exerted on the MWCNTs by the matrix.

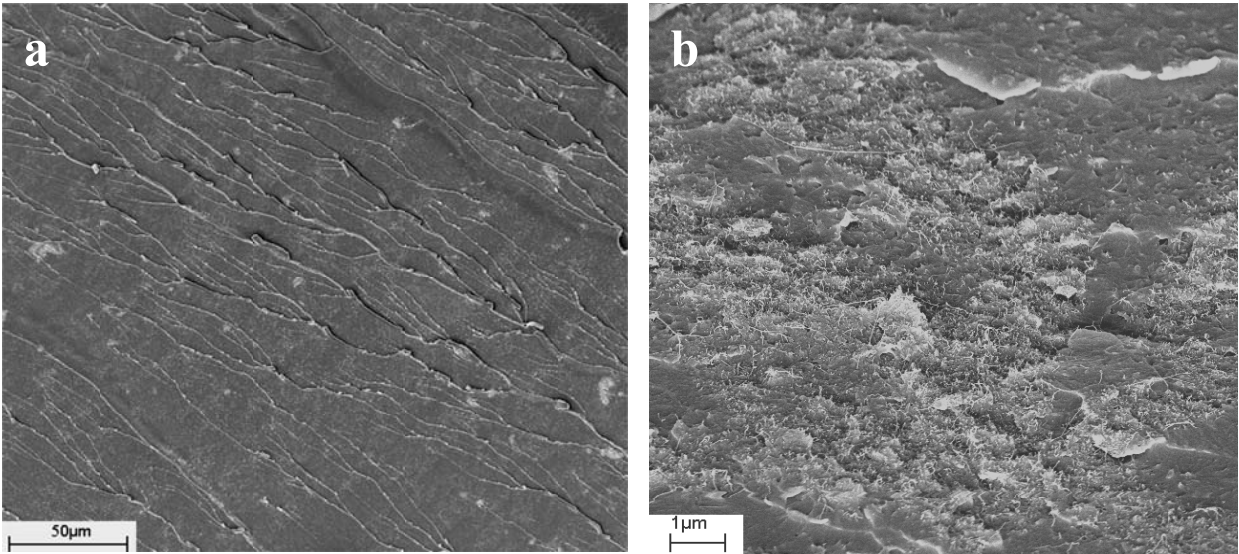


Fig. 3.4. SEM micrographs for the fracture surface of MWCNTs–epoxy composite sample: (a) global dispersion and (b) local dispersion

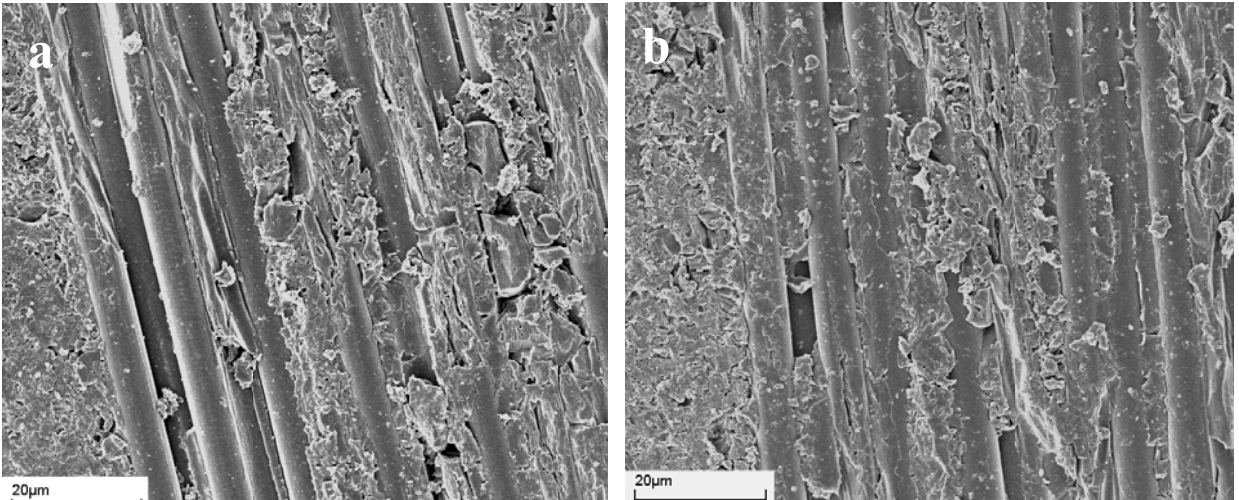


Fig. 3.5. SEM micrographs for the cross section of the CFRP containing MWCNTs (a) and CFRP based on neat epoxy (b)

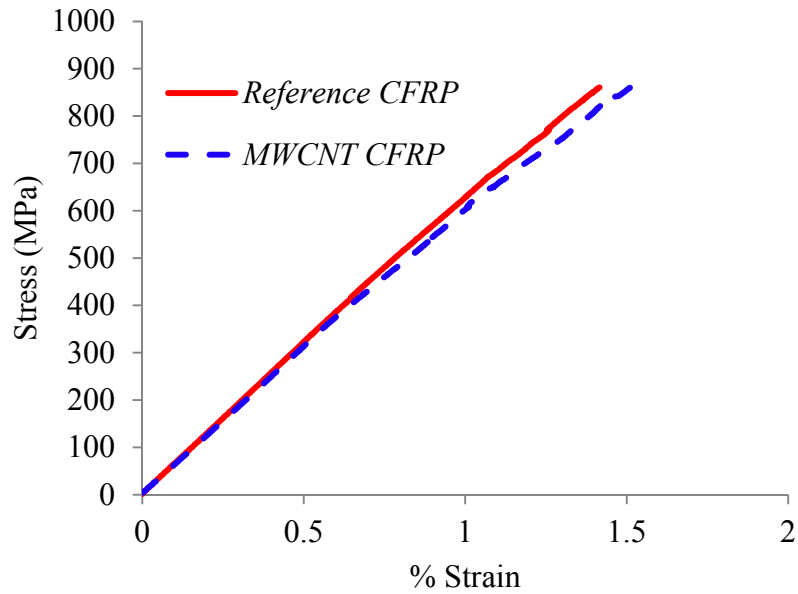


Fig. 3.6. Representative stress-strain curves for the composites comprising neat epoxy and CNT-epoxy matrices.

Tensile properties of the composite samples based on neat epoxy and MWCNT-epoxy are plotted in Fig. 3.7. While a very slight increase in the Young's modulus and the strength were achieved, the strain to failure was improved by 12%. The tensile modulus and strength of the CFRPs are dominated by their fiber phase properties and hence the improvements in the stiffness and strength of the matrix slightly affect the overall tensile properties.

The CNTs act as stiff barriers that inhibit cracks within the matrix from progressing and thus the matrix can carry loads even after cracks are initiated. In addition, the enhanced fiber-matrix bonding promotes the load transfer to the fibers and leads to an impeded fiber-matrix interface failure and, hence, a higher strain to failure is achieved. The enhanced adhesion between the fiber and the matrix was owed to the relief of stress concentrations at the fiber-matrix interface due to the existence of CNTs. While the strain to failure for the single dry fibers is reported by

the manufacturer to be 1.9 %, the reference composite exhibited a 1.38 % strain to failure. This value was increased to 1.55 % for the samples based on the CNTs-epoxy matrix.

Since both constituents of CFRPs are brittle, a high strength generally entails good fiber-matrix adhesion. However, strong interfacial bonding may lead to low fracture energy absorption. If the bonding is too strong, the tensile strength may decrease as a result of cracks propagating transversely and cutting through fibers and matrix. Therefore, it is imperative to achieve a suitable combination of strength and impact toughness. This can be obtained by both altering the fiber-matrix interface and fracture toughening of the matrix (e.g. via addition of CNTs).

Based on the loss tangent measurements, Fig. 3.8, the addition of CNTs promoted the mechanism by which the composite dissipates energy. The matrix volume fraction for the both fabricated configurations was about 40%. Due to its inherent viscoelastic nature, the matrix material contributes more than the fibers to the overall damping of the composite. Meanwhile, the addition of low amounts of high surface area CNTs (i.e. 2.0 %wt.) engenders significant nanotube-epoxy interactions and energy dissipation. Compared to the reference sample, the loss tangent of the composites based on MWCNTs-epoxy matrix increased by an average of 25.8 % over the 1-52 Hz frequency range. Although, the loss tangent presents a nonlinear frequency dependent behavior, the same frequency dependent pattern is observed for both samples. Evident by Fig. 3.8, the flexural mode storage modulus of the composites exhibited a frequency independent behavior and similar to tensile test findings the storage modulus was marginally changed for the CFRP incorporating CNTs.

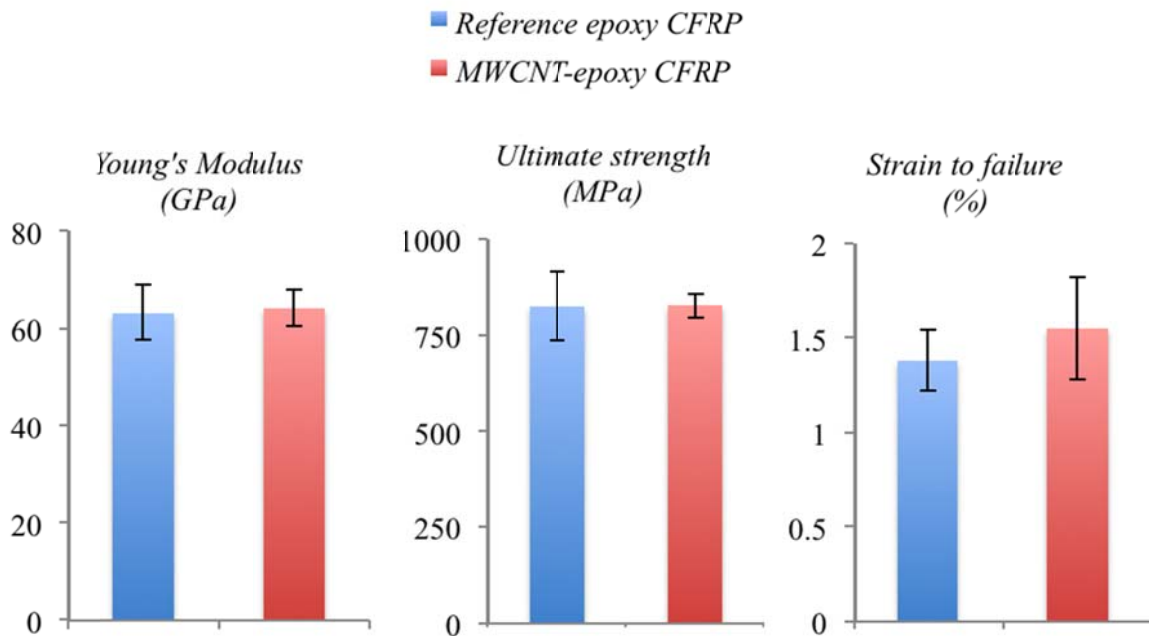


Fig. 3.7. Tensile properties for the two composite systems.

The kinetic energy of the steel impactor was calculated before and after it perforated the composite panels. The average absorbed energies are plotted in Fig. 3.9. These averaged values suggest that the incorporation of MWCNTs in the matrix of a CFRP enhances the energy absorption capacity of the composites by almost 21.3 %. This enhanced impact resistance can be attributed to the increased interlaminar fracture toughness and delamination resistance that alleviates the crushing/buckling strength of the fibers.

In addition, the presence of the MWCNTs delays the delamination of the plies and prevents the expansion of micro-cracks. Due to the high surface area of the MWCNTs, failure of the MWCNT-epoxy interphases and MWCNTs pull-out dissipate considerable amount of energy.

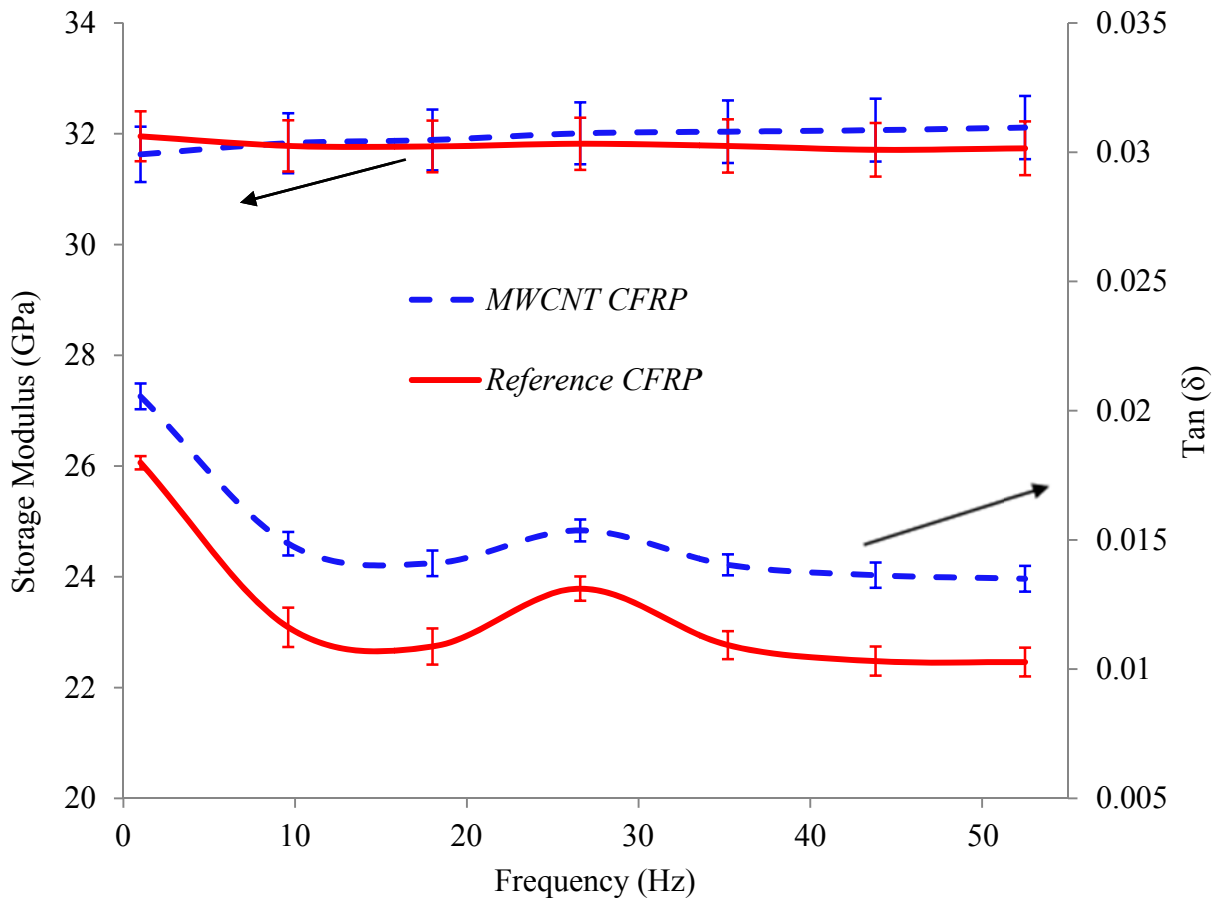


Fig. 3.8. Damping ($\tan\delta$) and storage modulus for the two composites based on neat epoxy and MWCNTs-epoxy matrices measured at various frequencies

Upon establishing the contact of the high velocity impactor with the composite panel, stress waves propagate through the panel. The amplitude of these waves changes due to the anisotropy and inhomogeneity of the composite at macro, micro, and nano scales. These waves get attenuated when passing through volumes with a high damping property. Impact involves the frictional interactions of different constituents of the composite that generate considerable amounts of heat which does not conduct in time scales of the impact (micro seconds in our case). This accumulated heat causes local temperature raise and gives rise to the viscous response from the constituents of the composite (especially polymer matrix). In addition, the high temperatures

can activate the sliding nanotube-matrix energy dissipation mechanisms. Therefore, CNTs promote the attenuation of stress waves and dissipation of energy.

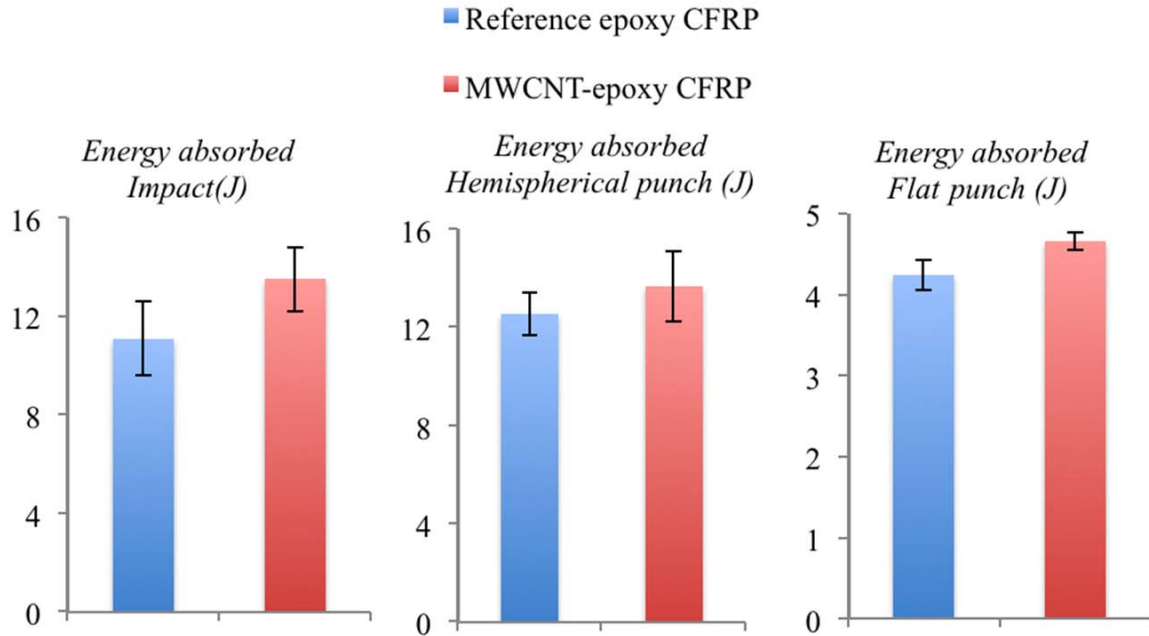


Fig. 3.9. Impactor absorbed impact energies and absorbed energy of the shear punch tests using cylindrical and hemispherical punches for the composites based on neat epoxy and MWCNTs-epoxy matrices.

Assessing the damage during an impact test is very costly if not impractical. However, the damage mechanisms can be predicted via the shear punch tests. While the flat cylindrical punch plunging is predominantly controlled by through thickness shear forces, the hemispherical punch plunging is caused by a combination of delamination and fiber breakage due to shear and tension forces. The state of the stress for both cylindrical and hemispherical punches is a complex combination of through thickness shear, compression and tension. Representative load-displacement curves for both punch geometries are shown in Fig. 3.10. The load-displacement curves using both punches were reproducible. For the flat cylindrical punch, a decrease in the

slope of the load-displacement curve (near the peak load) indicating that matrix cracking took place. Subsequently, via intensive through-thickness shear and compressive forces, the flat punch shears the panel at the periphery of the punch head. The hemispherical punch indents the panel, causes delamination (evident by the abrupt drop of the load) and progressively breaks the fiber tows while puncturing through the specimen. Compared to the reference sample with neat epoxy matrix, the CFRP comprising MWCNTs exhibited an earlier minor delamination followed by an impeded major delamination. In addition, lesser fiber breakage for the samples containing MWCNT renders a higher penetration load at the very late stages of the punch perforation. These effects can be attributed to a better fiber-matrix load transfer, increased strain to failure, and enhanced through-thickness shear strength of the MWCNTs containing composites.

The shear punch peak loads as well as puncture energies of samples utilizing both punch geometries are summarized in Table 3.1. Evident by the cylindrical shear punch results, adding the MWCNTs to the matrix of the CFRP improved the through-thickness shear strength of the panels as well as the energy needed to perforate the samples. For the cylindrical punch these energy levels are far below that of the impact absorbed energies. However, the hemispherical punch perforation energy levels are analogous to those in the impact tests. In the hemispherical punch test, the multistage delamination and perforation of the CNTs containing composites resulted in a lesser value of maximum punch load for the hybrid composites compared to the ones based on neat epoxy matrix.

Table 3.1. Peak load and absorbed energy of shear punch tests using cylindrical and hemispherical punches

		Peak Load (KN)	Energy absorbed (J)
Flat cylinder punch	Reference	12.46±0.23	4.24±0.19
	CNT	14.04±0.27	4.66±0.11
	% improvement	12.7	10.1
Hemispherical punch	Reference	4.32±0.35	12.55±0.87
	CNT	4.21±0.25	13.68±1.42
	% improvement	-2.3	9.0

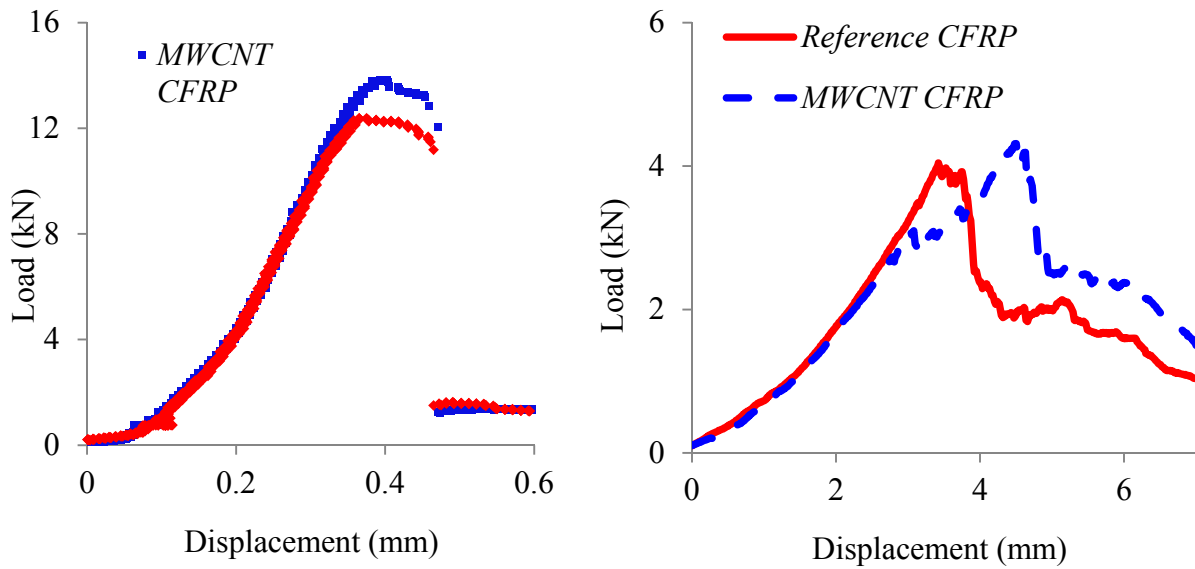


Fig. 3.10. Representative shear punch tests obtained for flat cylindrical (left) and hemispherical (right) punches

The absorbed energy of the hemispherical shear punch tests is calculated only up to the point that the hemisphere head of the punch punctures the specimen. In an impact test, after the first half of the spherical impactor is passed, some energy is dissipated through the frictional interaction of the impactor and the broken tows. Although the energies for the hemispherical punch and impact perforations are identical (less than 2% difference) for the MWCNTs-CFRP specimens, the shear punch test overestimated the impact energy of the reference sample with neat matrix. It is worth noting that while the boundary conditions play a major role in a quasi-static shear punch test, they are far less influential in an impact test.

An improved fiber-matrix adhesion results in a more uniform stress distribution, higher strain to failure, and the toughening of the composite. On the other hand, CNTs prevent transverse matrix cracking and thus the MWCNTs reinforced matrix requires higher energies to be cracked. Since the fibers in the studied samples were identical, the increase in the absorbed impact energy of the MWCNTs containing CFRP composite compared to the reference samples is solely influenced by the matrix dominated properties and the altered interphase between the fibers and matrix.

In addition to shear punch tests, valuable information on composites' damage can be acquired from X-ray radiography. As shown in Fig. 3.11, the size of the damaged area for both specimens was similar to the impactor size (i.e. 1.27 cm) and slight delamination was observed only on the periphery of the perforated zone. Therefore, the impact energy absorption due to the delamination was limited to the immediate vicinity below the impact spot.

The improved impact resistance of the CNTs-CFRP composite is owed primarily to its increased damping due to the presence of CNTs. It can be speculated that the other factors contributing to this improvement are the enhanced matrix fracture toughness, increased delamination resistance

and interlaminar mechanical properties and increased buckling strength of the fibers against the high compressive stresses generated during an impact perforation. It can be perceived that the major energy absorption mechanisms of the thin composite panels of this study were matrix cracking, fiber breakage, fiber pull-out, and local indentation.

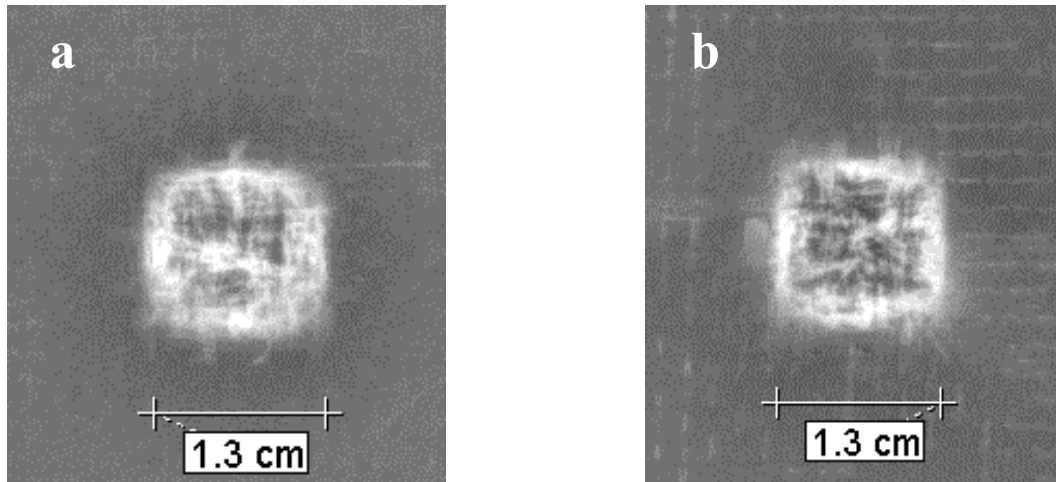


Fig. 3.11. X-ray radiographs of the impacted samples; (a) reference CFRP and (b) MWCNTs enriched CFRP

3.5 Conclusions

It was shown that the quasi-static tensile properties (stiffness and strength) do not change along the axial directions of the fibers in a CFRP with incorporated MWCNTs. The only improvement observed from the on-axis tensile tests is the strain to failure. Compared to the reference CFRPs, the MWCNTs enriched CFRP exhibited a higher damping and through-thickness shear strength. In addition, under high strain rate (i.e., impact) loading, the absorbed energy of the CFRP reinforced with MWCNTs is superior to that of the reference CFRP. The progressive damage was assessed through performing shear punch tests utilizing the same shaped punch as the

impactor used in the impact test. The damage mechanisms were different for the CFRPs based on neat and MWCNTs enriched epoxy matrices. While the MWCNTs-CFRP exhibited a multiple stage delamination and lesser amount of tow failure, the CFRP with neat matrix delaminated abruptly and consumed less energy to be punctured. It was concluded that, these enhancements were owed to the improved fiber-matrix adhesion and CNT-matrix interactions. Evident by the X-ray radiographs of the impacted composites, among the different energy dissipation mechanisms, the impact energy absorption is to a lesser extent controlled by delamination and matrix cracking.

Shear punch tests were shown to provide valuable information on different energy absorption modes as well as impact damage progression in FRPs. Furthermore, the absorbed impact energies can be roughly estimated by shear punch tests. However, in order to predict the composites' impact behavior, it is crucial to take into account their strain-rate-dependent behavior; stress wave accumulation. The work outlined in this chapter suggests that if a moderately good dispersion of the MWCNTs in the polymer matrix is attained, the mechanical properties of the CFRP improve both under quasi-static and dynamic loading environments. This enhancement occurs virtually at no weight increase, locally generated heat, and damping capability of the composite.

Chapter 4. Growing Carbon Nanotubes over Carbon Fibers

4.1 Overview

There is a growing need for multifunctional advanced materials for a wide variety of applications. In this regard, carbon nanotubes (CNTs) have shown promise for enhancing properties of fiber reinforced composites (FRPs) and imparting multi-functionalities to them. While mixing of CNTs with the polymer phase in FRPs has several drawbacks (as described in previous chapters), high volume fractions of uniformly dispersed CNTs can be directly grown on fiber surfaces. However, it is necessitated to develop novel methods to grow carbon nanostructures on carbon fiber yarns where minimal thermal degradation to the fiber (substrate) takes place.

This part of the dissertation demonstrates a unique ability to create carbon nanostructures on the surface of carbon fibers. Specifically, this chapter details a relatively new synthesis method, in which carbon structures are grown from fuel rich combustion mixtures using palladium and nickel particles as catalyst. Of significance of the new technique, graphitic structures by design (GSD), is proven feasible to grow nano-scale diameter filament structures -from ethylene mixtures at 550 °C- on commercial PAN-based carbon fibers. The grown filaments geometry is shown to be highly dependent on the catalyst particle size. Incipient wetness and physical vapor deposition are utilized to deposit nanometer sized catalyst particles on carbon fibers. X-ray diffraction, Raman spectroscopy and electron microscopy are employed to characterize the grown carbon species. A protocol is developed such that only CNTs could be produced. This

fiber structure potentially can enhance composite material strength, ductility and energy absorption characteristics. For comparison purposes, catalytic chemical vapor deposition (CCVD) technique was also utilized to grow CNTs on carbon fiber yarns. Furthermore, to lessen the undesirable effect of CNT formation temperatures on carbon fibers the developed CNT growth procedure was applied to identical fibers that were thermally shielded with a thin layer of SiO₂.

4.2 Introduction

Fiber reinforced polymer composite (FRP) failure under high-energy loading, i.e. impact, can be traced to the limited bond strength between the matrix and the fibers [13, 99, 100]. Multi-scale fiber systems that include high surface area nano components will have increased surface area, hence possibly increased shear strength. The most common approach to creating a multiscale system is simply to physically mix carbon nanotubes into a more traditional composite consisting of epoxy with embedded micro scale fibers, as outlined in chapter 2. The inclusion of carbon nanotubes (CNTs) clearly toughens different matrices [101, 102]. Depositing CNTs in a brittle matrix increases stiffness by orders of magnitude [103]. This approach to create multiscale composites is limited due to the difficulty of dispersing significant amounts of nanotubes [12, 104] and it has repeatedly been reported that phase separation occurs above relatively low weight percent loading (i.e. 3%) due to the strong Van der Waals forces between the CNTs compared with that between the CNTs and the polymer matrix. Hence, the nanotubes tend to segregate and form inclusions.

One means to prevent nanotubes or nanofilaments agglomeration is to anchor one end of the nanostructure, thereby creating a stable multiscale structure. This is most readily done by literally

growing the CNTs directly on micron scale fibers. CNTs can be controlled-grown on surfaces where they are needed. CNTs have been grown on most substrates such as silicon, silica, and alumina [16]. However, there are fewer reports discussing CNT growth on carbon materials; in particular yarns and fabrics [17]. Two challenges in CNT growth on carbon substrates are: (i) transition metals that catalyze the CNT growth are easily diffused into the carbon substrates and (ii) different phases of carbon materials are able to form on the graphite substrates because the CNT growth conditions are similar to the diamond or diamond-like carbon growth [18].

Recently, CNT were grown on carbon fibers, both polyacrylonitrile- (PAN-) and pitch-based, by hot filament chemical vapor deposition (HFCVD) using H_2 and CH_4 as precursors. Nickel clusters were electrodeposited on the fiber surfaces to catalyze the growth and uniform CNTs coatings were obtained on both the PAN- and pitch-based carbon fibers. Multi-walled CNTs with smooth walls and low impurity content were grown [105]. Carbon nanofibers were also grown on a carbon fiber cloth using plasma enhanced chemical vapor deposition (PECVD) from a mixture of acetylene and ammonia. In this case, a cobalt colloid was used to achieve a good coverage of nanofibers on carbon fibers in the cloth [21]. The caveats to CNTs growth via CVD include damage in the carbon fiber surface due to high-temperatures (>800 °C) [18, 105]. Qu et al. [106] reported a new method for uniform deposition of CNTs on carbon fibers. However, this method requires processing at 1100 °C in the presence of oxygen and such high temperature is anticipated to deepen the damage in the carbon fibers.

In this chapter carbon nano-filaments were created utilizing a low temperature (i.e. 550 °C) alternative to CVD growth of CNTs where catalytic (Pd or Ni particles) growth occurs from a fuel rich combustion environment at atmospheric pressure. This atmospheric pressure process

[29, 107], derived from the process called Graphitic Structures by Design (GSD), is rapid, the temperature is low enough (i.e. 550 °C) to avoid structural damage, and the process is inexpensive and readily scalable. The GSD process does not require any toxic hydrocarbons or catalysts (e.g. xylene and metallocene) such as those employed in CCVD for CNT synthesis [25]. The GSD would offer the opportunity to place CNTs in pre-designated locations (where the catalyst is pre-deposited) whereas utilizing the CCVD technique, CNTs get deposited everywhere.

A similar mean to generate carbon fibers on a parent structure was published by Downs et al. [108, 109], who used hydrocarbon/H₂ mixtures produce carbon filaments on commercial PAN-based fibers at 650 °C although employing diverse Cu-Ni alloys as catalyst. Such work relies on the use of a different catalyst, reducing atmospheres and slightly higher temperatures than the ones reported here.

The fundamental difference between the GSD method and all alternative methods (such as CCVD) is that in GSD a reactive gas mixture is employed and graphitic structures form from carbon containing radicals produced by homogenous reaction processes. In all other methods, the carbon structures are formed via thermal decomposition of a hydrocarbon species on the surface where there is no oxygen and hence no gas phase reactive process occurs. GSD can grow graphitic filaments at low temperatures with the presence of oxygen -as low as 400 °C [19] and at relatively higher temperatures -550 °C- where no oxygen is used. Moreover, Feih et al. [110] showed that upon the exposure to temperatures higher than ~500 °C at the presence of Oxygen, both the stiffness and the strength of the T-700 carbon fibers dropped. In addition, the damage of the surface of the fibers was shown to be in the form of ~100 nm flaws. Therefore, to prevent

any mechanical properties loss due to the GSD, it is essential to keep the temperature low (i.e. 550 °C) and eliminate Oxygen from the reaction environment. Removal of Oxygen can be achieved by vacuuming the reaction chamber and flushing it with N₂ before the furnace is set to the desired temperature.

The advantages of the GSD technique are significant. First, films can be formed that precisely match the underlying metal template, even at the nano-scale. Second, for planar graphitic structures, as contrasted to fibers and nanotubes, the temperature of formation is about 1500 °C lower than any available alternative [29]. Third, it permits the growth of filaments directly on a pre-formed graphite template; the first graphitic layers act as self-catalyst and the need for the metal catalyst is diminished. Fourth, a graphite to filament transformation results simply from changing temperatures; the nature of the structures is a function of the temperature only, for constant conditions of flow and stoichiometry. Hence, by changing temperature one can switch the nature of the growth. Finally, utilizing the GSD method filamentous forms of carbon, of a variety of shapes can be created [29].

This chapter reports an effort to grow CNTs over carbon fibers at 550 °C utilizing two different routes. The first modified GSD route involves using of Pd catalyst deposited via incipient wetness and employs C₂H₄, O₂, H₂, and N₂ as reaction gasses. While this method yields nanofilaments of carbon over carbon fibers, the grown species were found to be non-graphitic. Therefore, the outcomes and experimental details of this method are briefly discussed. The second modified GSD route entails deposition of nickel via physical vapor deposition (i.e. plasma assisted) and does not make use of O₂. This route enabled a uniformly growth of graphitic CNTs. Hence, this chapter particularly emphasizes the findings of the second method.

4.3 Experimental methods (utilizing Pd as catalyst)

4.3.1 Sample preparation

The process employed for the nanofilament synthesis involves three main steps; a sizing burn-off/activation process of the commercial filaments, wet impregnation to create well dispersed nano-scale metal catalyst particles and actual nano-scale filament growth via exposure to a low temperature fuel rich combustion environment. The details of the filament growth procedure can be found in [19] and are summarized below.

The process employed for the nanofilament synthesis involves three main steps; a sizing burn-off/activation process of the commercial filaments, wet impregnation to create well dispersed nano-scale metal catalyst particles and actual nano-scale filament growth via exposure to a low temperature fuel rich combustion environment.

Commercial PAN carbon fibers (~7.5 μm diameter, Toho Tenax America, Inc.) were used as the micron scale support, on top of which nanostructures were to be generated. Fibers were chopped to 3 and 6 mm lengths. In order to remove the sizing, the carbon fibers were treated in a tubular furnace at 525 $^{\circ}\text{C}$ in O_2 (100 sccm flow) for 10 minutes. The treated fibers were removed, rinsed in ethyl alcohol and dried in air at 100 $^{\circ}\text{C}$ for 1 hour. In order to ‘activate’ the carbon, the fibers were then ‘burned’ (O_2 , 100 sccm, 525 $^{\circ}\text{C}$, and 20 minutes). These two processes resulted in a net weight loss between 10 and 15%.

The catalyst was prepared by incipient wetness impregnation using $\text{Pd}(\text{NO}_3)_2 \cdot 6\text{H}_2\text{O}$ (99.9%, Sigma Aldrich) as precursor with the pretreated micron carbon fibers as support. The amount of precursor salt, Pd (II) nitrate hydrate, required for a final metal loading of 0.05, 0.5, 1, 5, 10 and

100 wt % was dissolved in de-ionized water. Once the carbon fibers were impregnated by the solution (just enough to 'wet' all fiber surfaces) they were left to dry for 12 hours in air at 100 °C.

4.3.2 *Filament generation*

After the drying step, fibers were placed in a sintered alumina combustion boat located at the center of a controlled atmosphere quartz tube (1 in. diameter) set in a 24 in. Lindburgh tube furnace. To assure that the catalyst precursor salts were decomposed and the metal was in a reduced state, the fibers were treated in three stages. These processes, and all other processes, were conducted at ambient pressure (no pump). The first step required calcining in inert gas at ~150 sccm at 250 °C for 4 hours. In the second step, the temperature was increased to 550 °C and a reducing gas mixture, 93%/7% introduced for 1 hour. Finally, at the same temperature, the system was flushed with N₂ gas (600 sccm) for 1 hour. This completed the pretreatments intended to produce highly dispersed and reduced Pd particles on the fiber. The 'GSD process' (carbon deposition from a fuel rich combustion mixture) was initiated immediately after the reduction process. A (fuel rich) mixture of N₂ (300 sccm), oxygen (15 sccm) and ethylene (15 sccm) was introduced while maintaining the temperature at 550 °C. This last step was performed at five different growth duration times: 1, 5, 35, 90 and 270 minutes for different specimens. Once the GSD process concluded, the heating elements were turned off and the reactor was flushed with nitrogen and then cooled. The initial flow (~2 minutes) was high (1000 sccm for two minutes), but reduced to low (50 sccm of N₂) for most of the cooling process.

4.4 Experimental methods utilizing Ni as catalyst

4.4.1 *Sample preparation*

Commercial high strength PAN-based plain-woven carbon fabric (AS4 supplied by HEXCEL Inc.) was utilized as the substrate to grow carbon nanotubes. Samples of $13 \times 13 \text{ cm}^2$ were cut from the raw fabric, some of which were reserved intact for the next step as reference samples. To shield the carbon yarn against the elevated temperatures encountered during the growth procedures and to prevent undesired carbon diffusion, thin films of thermal coating (75 nm thick SiO_2) were sputtered on the fabric upper and lower surfaces [26]. The catalyst in the form of a 2 nm thick film of nickel was sputtered on top of the SiO_2 layers. A magnetron sputtering system (ATC Orion high vacuum sputtering system, AJA International Inc.) was employed to sputter both the SiO_2 and nickel films on the PAN-based carbon fiber fabrics. The sputtering process was carried out with argon gas flow at 300 Watts power from an RF source (to deposit the 75 nm SiO_2 film on the surface of the carbon fibers) and a DC source (to deposit the 2 nm nickel film on top of the SiO_2 film) both at 3 millitorr vacuum.

Graphitic structures by design (GSD)

4.4.2 *CNT growth*

In order to grow carbon nanotubes on the fabrics coated with SiO_2 and nickel films, a tube furnace reactor was utilized. The furnace comprised a 7.62 cm diameter quartz tube and a 45.72 cm heating zone. First step of the growth process involves flushing the tube with nitrogen and vacuuming it with a mechanical pump while the nitrogen was flown at 3000 sccm. This step ensures the elimination of oxygen inside the reaction tube.

Based on previous experiences, the nickel film should be fragmented into particles to grow CNTs via GSD, otherwise it might lead to the growth of either graphene or graphite [24]. A reduction step at 550 °C under N₂-H₂ environment was carried out for 2 hours under atmospheric pressure to break the nickel film into nanometer-sized particles and to remove any nickel oxides (see **Fig. 4.1-a and b**).

The CNT growth was initiated as a mixture of N₂/H₂/C₂H₄: 750/15/60 sccm was introduced while maintaining the temperature at 550 °C. The growth time was set to one hour. The hydrocarbon (Ethylene) undergoes a homogeneous reaction over the nickel catalyst in the presence of H₂ and the carbon radicals get deposited in the form of nanotubes [19, 24, 111]. The furnace was cooled down to ambient temperature under an inert nitrogen environment. **Fig. 4.1-c** shows the grown CNTs utilizing GSD along with the nickel particles attached to their tips.

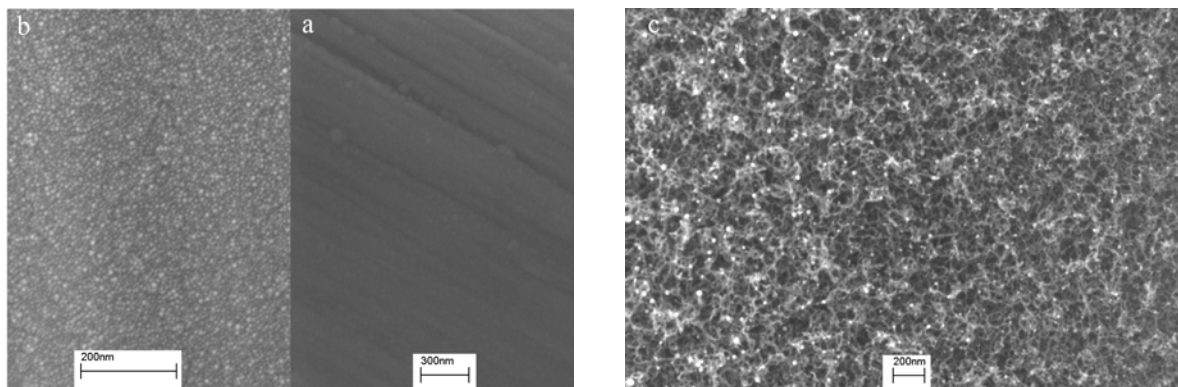


Fig. 4.1. Nickel catalyst layer (a) before and (b) after reduction under N₂-H₂ at 550 °C; nickel islands were formed. (c) CNTs grown utilizing GSD technique with nickel particles attached to their tips.

4.4.3 *Sample characterization*

A 5200 Hitachi SEM and a FEI-Titan 300 TEM operated at 5 and 300 keV, respectively, were utilized to examine the synthesized MWCNTs. Raman spectra were obtained utilizing a ProSeek Raman system from Raman System, Inc. These spectra were obtained with a confocal Raman microscope, using a 5 mW, 785 nm excitation wavelength laser beam focused on the sample with a 50X objective. Spectra were obtained as the sum of 30 s integration time.

4.5 Results and discussion (Pd as catalyst)

The burn-off process created ‘active sites’ which served as nucleation centers for metal catalyst particle formation. The distribution of filament diameters reflected the distribution of diameters of the catalyst particles. Indeed, for very low Pd loadings (i.e. 0.05%) only filaments with diameters averaging around 10 nm grew, suggesting only nanoscale catalyst particles were present. At higher metal loadings (i.e. <1.0%) bimodal fiber distributions were found, suggesting a bimodal size distribution of catalyst particles were present. In all cases, the filaments apparently grew from radicals generated in the combustion environment, with a diameter roughly equal to the size of the catalytic particle.

Comparison between SEM (Fig. 4.2) and TEM (Fig. 4.3) of samples with metal loading beyond the saturation point (more below), and treated in the GSD process (550 °C, 1:1 O₂:C₂H₄, 35 minutes), provides clear visual evidence of a complex ‘two layer’ and ‘multi-scale’ filament growth pattern. It is important to note in examining the SEM and TEM pictures that attention to only one type of microscopy leads to a misunderstanding of the structure. For example, the filament structure is composed of ‘slow’ growing filaments with a mean diameter of about 5 nm,

and ‘fast’ growing filaments that have a less dense layer of larger diameter (i.e. 50 to 150 nm) compared to the first group of filaments. A helpful analogy: there is a layer of ‘trees’ clearly not tightly packed, and below that, at ground level, a dense layer of ‘grass’.

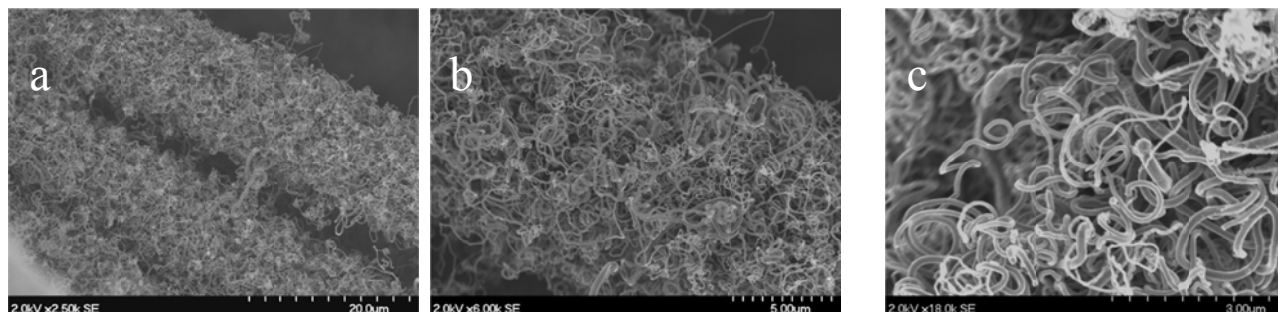


Fig. 4.2. SEM of Sub-micron Filaments. These samples were treated in a 1:1 mixture of $O_2:C_2H_4$ for 90 minutes at 550 °C. a) A ‘perspective’ view of several filaments that were pretreated PAN-based carbon fibers. b) A closer view reveals that the filaments are generally less than 100 nm in diameter, are not straight and tangle together to form mats. c) Note that there appear to be metal particles at the ‘head’ of many of the filaments.

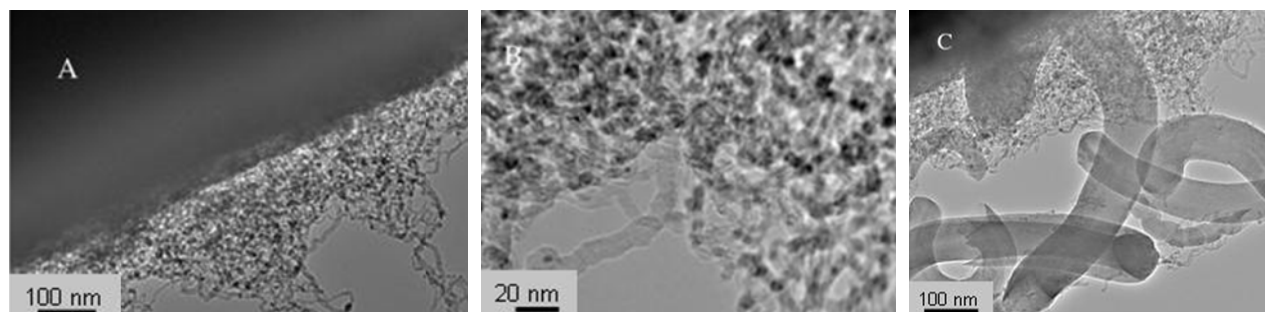


Fig. 4.3. Nano-scale Filaments. A) Relatively dense layer of filaments with an average diameter of ca. 10 nm forms on the surface of the fibers. The average height of this layer is less than 200 nm. B) The Pd particles that catalyze filament growth can clearly be seen. C) The dramatic difference in size of the two types of filaments can be observed in the figure. This sample was treated under GSD conditions for only 35 minutes. The metal loading weight was 0.5%.

In the cases where the metal loading was kept to relatively a very low level, the observed morphology was much simpler (Fig. 4.4). A sample loaded with only 0.05% metal and treated to the standard GSD treatment (550 °C, 1:1 $O_2:C_2H_4$) but for an extended time, 270 minutes, grew

primarily the ‘grass’ layer, that is the filaments have a mean diameter of about 5 nm and the net length, <0.5 micron, is consistent with ‘slow’ growth. Some of the larger fibers are also present, but clearly far fewer than observed at metal weight loadings of 0.5% and higher. TEM images not shown here but are similar to those shown in Fig. 4.3-A and B.

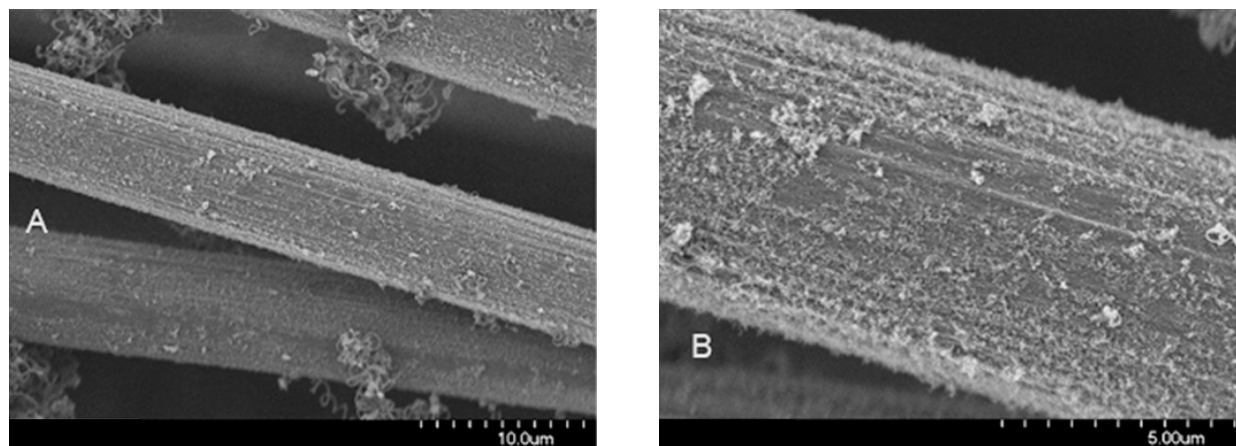


Fig. 4.4. SEM of saturation loaded sample. To allow growth sufficient to observe with SEM, sample treated using standard protocol, but with 270 minutes of exposure to GSD conditions. (A) Clearly the fibers are not covered with sub-micron filaments. Contrast with Fig. 4.2. (B) The surface is virtually completely covered with nanofilaments.

Every effort was made to characterize the structure of the filaments, in particular their degree of graphitization. The methods employed were X-ray diffraction (XRD), TEM, temperature-programmed oxidation (TPO) and Raman spectroscopy. XRD analysis revealed only a weak and rather broad peak for all samples near $25.5^\circ 2\theta$ indicating an amorphous or turbostratic structure.

The Raman data was inconclusive (not shown). Pure PAN fibers with sizing removed and fibers with filaments produced indistinguishable Raman spectra. Moreover, in all cases, the G (graphite) and D (disorder) peaks were of nearly identical relative magnitude. The only method

that appeared to yield a distinct signal was TEM. As shown in Fig. 4.3-B, all TEM data are consistent with the interpretation that most of the filament growth is amorphous in character.

All filaments grew from Pd catalyst particles deposited on the commercial PAN fiber surfaces. It is presumed, given the low temperature employed and the phenomenological similarity with earlier studies [29, 107], that the source of carbon for filament growth was radicals generated homogeneously (e.g. CH_2). These react on the metal catalyst particles, decomposing readily to deposit carbon atoms (e.g. $\text{CH}_2 \rightarrow \text{C} + \text{H}_2$). Carbon atoms deposited at the catalyst particle surface, driven by a chemical potential gradient, transport through the catalyst particle, or around its periphery, to 'add' to the solid carbon forming behind the particle. In fact, this same mechanism, the so-called 'root' mechanism, is used to explain the growth of carbon nanotubes.

All characterization methods, particularly TEM, suggest that the filaments are not crystalline. That is, only short range order is evident, consistent with the growth of turbostratic carbon. In contrast, on nickel under the same conditions, graphitic carbon growth has been found [29].

4.6 Results and discussion (Ni as catalyst)

4.6.1 Electron microscopy and Raman analysis

The SEM images in Fig 4.5.a-b show a uniform growth of CNTs utilizing GSD and CCVD techniques, respectively, on the surface of PAN-based carbon fibers where the nickel catalytic particles were deposited (for the case of GSD). Both fibers were shielded by 75 nm thick films of SiO_2 . In the GSD method, CNTs apparently grew from radicals generated in the C_2H_4 , H_2 , and N_2 atmosphere, with a diameter roughly equal to the size of the catalytic particle as observed in Fig. 4.5-a.

Unlike other methods for deposition of metal catalysts on the fabric, physical vapor deposition (PVD) ensures a uniform deposition of an ultra-thin film of nickel. The capability to uniformly sputter a 2 nm thick nickel film reflects in the persistent diameter of the CNTs grown via GSD compared to those grown using CCVD, and results in a small variation in the diameter of the grown CNTs; compare Fig. 4.5-a and c. The structure of the MWCNTs along with their parallel side walls are shown in the TEM images, Fig. 4.5 (c-d). The GSD synthesized nanotubes have a diameter of less than 20 nm whereas the CCVD yielded CNTs with variable diameters (see Fig. 4.5-c).

Since the samples containing surface grown CNTs were exposed to high temperatures (i.e. 550 °C and 680 °C), reference samples of raw fabric and SiO₂ sputter-coated fabric were exposed to similar thermal treatments as in GSD (except for the introduction of the hydrocarbon gas) for later comparison. These samples are referred to “heat treated” throughout this dissertation. The Raman spectra were measured for the raw PAN-based carbon fabric, SiO₂ sputter-coated fabric, heat treated fabric, heat-treated SiO₂ sputter-coated fabric and the samples with CNTs grown on their surfaces via GSD and CCVD methods.

While the as sputtered nickel thin film is amorphous, evident by the ordered fringe patterns of Fig. 4.6-a, upon fragmentation and reduction the nickel particles become crystalline. As shown in Fig. 4.6-b the energy-dispersive X-ray spectroscopy (EDS) of the same particle exhibits the peaks for the crystalline nickel. The copper peaks are from the background copper TEM grid.

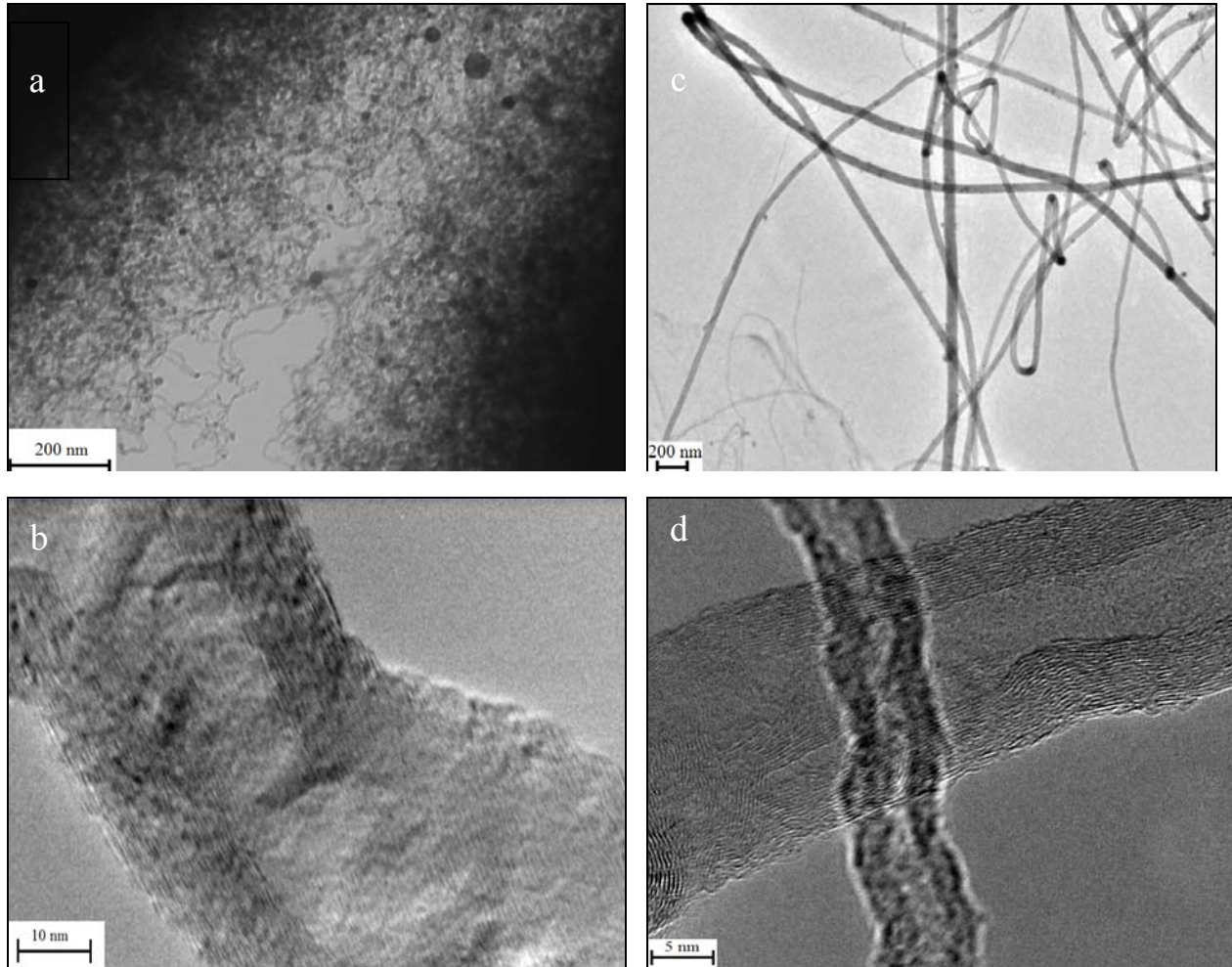


Fig. 4.5. (a-b) TEM micrograph of MWCNTs grown via GSD (c-d) TEM micrograph of MWCNTs grown via CCVD.

For carbonaceous materials the Raman spectra exhibit two distinguished bands, the disorder-induced D band at 1354.7 cm^{-1} in MWCNT spectra and between 1330 and 1390 cm^{-1} in SWCNT. The tangential mode G band, related to the ordered graphitic structure, appears at 1581.2 cm^{-1} for the MWCNT, and between 1595 cm^{-1} and 1605 cm^{-1} for the SWCNT [112]. Raman peaks, Fig. 4.7, for all of the samples without CNTs are very weak and do not exhibit presence of significant crystalline form of carbon. The raw carbon fibers did not show significant peaks. It is well known that PAN-based carbon fibers do not exhibit the G band (unlike graphitic pitch-based

fibers), rather they exhibit spectroscopic appearance of the D line, which corresponds to the structural disorder caused by the existence of the sp^3 bonds [113]. Sputtering the fibers with nanoscale nickel and SiO_2 films assisted in contrasting the G band for the fibers. Furthermore, heat treating the samples with the deposited films made the D and G bands more distinguishable. The CNTs grown on the surfaces of the PAN based carbon fiber fabric via GSD or CCVD demonstrate the D-band center value at 1350 cm^{-1} and the G-band at 1595 cm^{-1} , respectively. Although these peaks are also observed for graphite [114] it is evident from the SEM and TEM images of the uniformly distributed filaments that the Raman peaks cannot be from graphite.

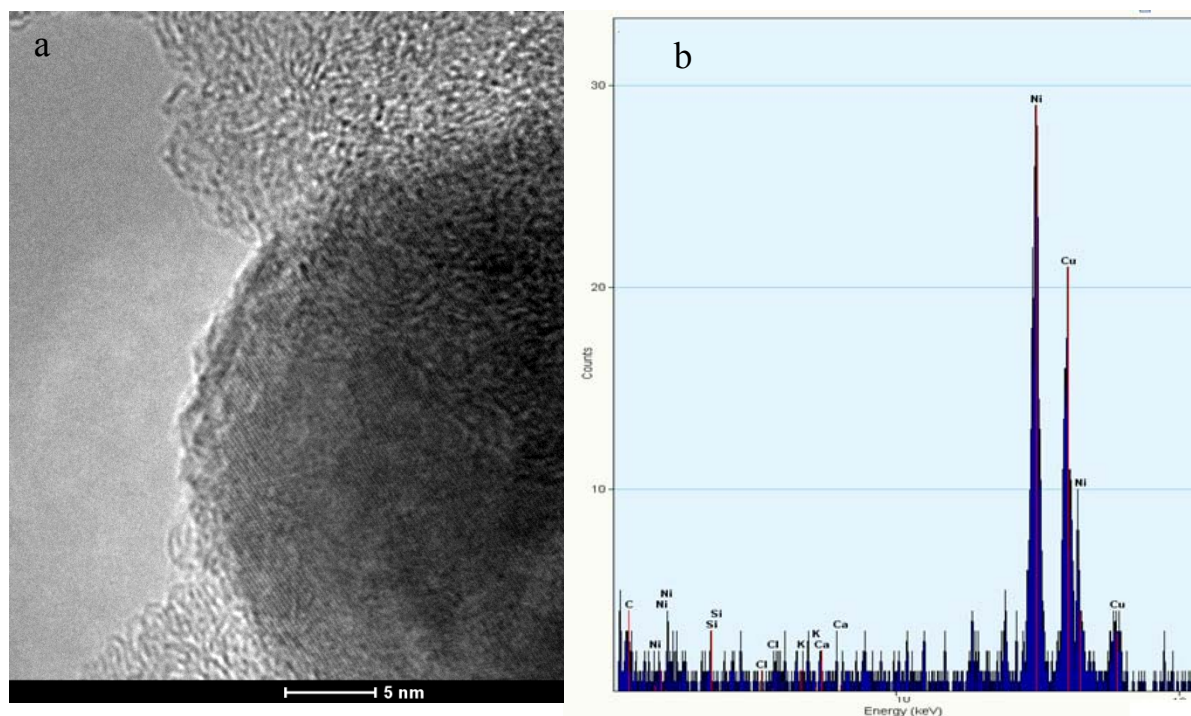


Fig. 4.6. TEM image of a nickel particle from which a CNT was grown (a) and the EDS of the same particle (b)

The intensity ratio of the two bands (I_D/I_G) can be conceded as a quantitative measure of the amount of structurally ordered graphite crystallite in the carbonaceous material. From Fig. 4.7,

the decrease in the intensity ratio (I_D/I_G) was more noticeable for the carbon fibers with MWCNTs grown by CCVD. This reveals that the degree of crystalline perfection of the MWCNTs grown using CCVD is higher than that of MWCNTs grown using GSD. Moreover, the width of the D peak for the CCVD sample is narrower than that for the sample prepared via GSD. This is an indication of a higher degree of order in the MWCNTs prepared via CCVD compared to those grown via GSD, which was observed in the TEM images, Fig. 4.5-c and d.

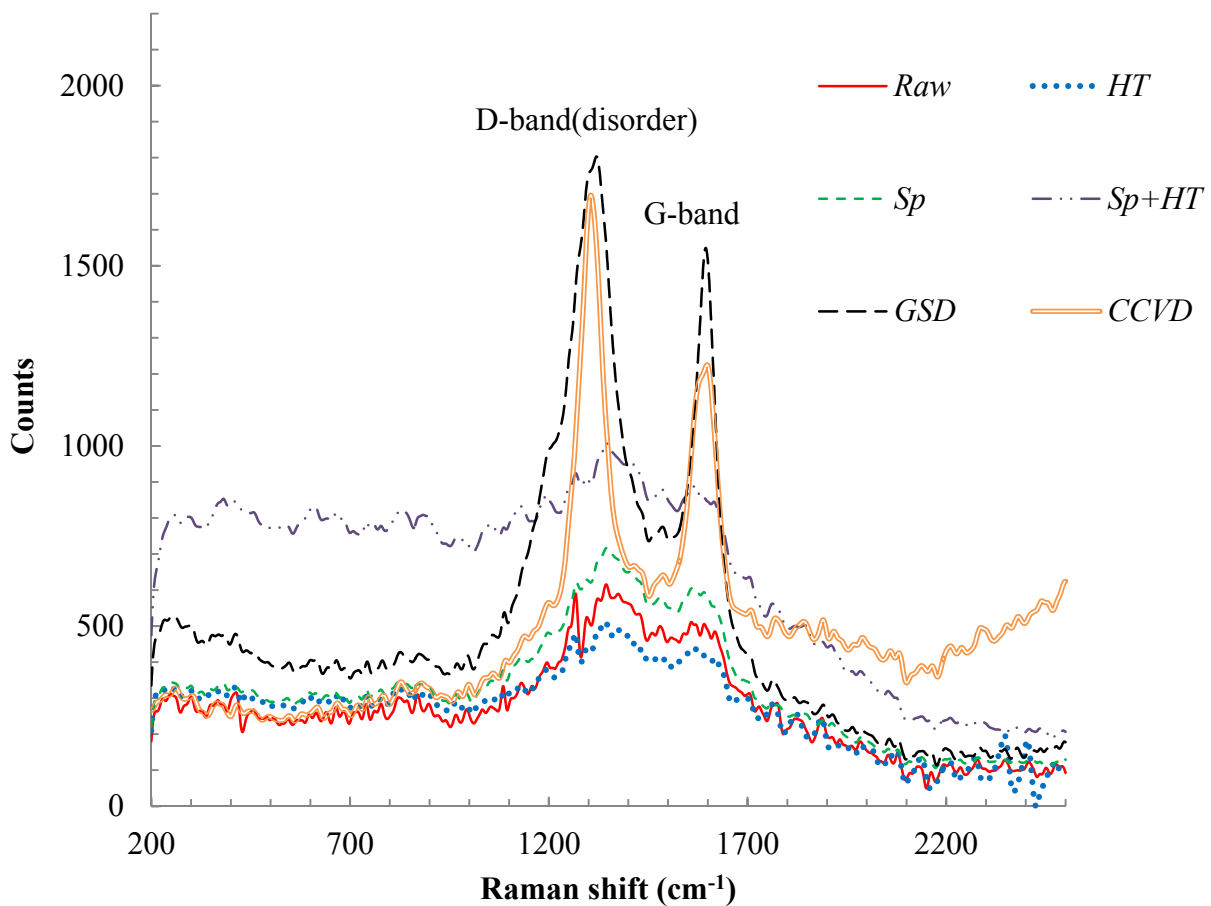


Fig. 4.7. Raman spectra of the surface of different processed carbon fibers. Specimens are based on raw PAN-based carbon fabric (Raw), SiO₂ sputter-coated fabric (Sp), heat treated fabric (HT), SiO₂ sputter-coated then heat treated fabric (Sp+HT), and the samples with CNTs grown on their surfaces via GSD (GSD) and CCVD (CCVD).

4.7 Conclusions

Multi-scale carbon structures grew catalytically from palladium particle impregnated PAN-based fibers exposed to ethylene/oxygen mixtures at 550 °C. As filament size roughly corresponds to catalyst particle size, this led to the formation of a bimodal size distribution of filaments. Relatively short, densely spaced nanofilaments (i.e. 10 nm diameter), and a slightly less dense layer of larger (i.e. 100 nm diameter) faster growing fibers (i.e. 10 microns/hr) were found to co-exist to create a unique multi-scale structure. At metal loadings less than saturation only the nanometer sized palladium particles were present, hence only nanometer scale filaments formed. All analytical techniques employed indicated poor crystallinity of the filaments based on Pd as the catalyst. On the contrary, graphitic MWCNTs grew on carbon fibers sheathed with nickel nanoparticles from ethylene/hydrogen mixtures at 550 °C. These findings indicate that GSD technique is capable of growing MWCNTs on graphite fibers at temperatures lower than utilized in the CCVD.

The work presented in this chapter demonstrates a unique ability to create a truly 'multiscale' carbon structure on the surface of carbon fibers. Potentially multi-scale structures like those produced here could enhance composite material strength, ductility and energy absorption characteristics. The mechanical performance of these multiscale carbon materials will be discussed in the next chapter.

Chapter 5. Mechanical Characterization of a Hybrid Multiscale Composite based on Fabrics with Surface Grown CNTs

5.1 Overview

A relatively low temperature technique to grow multi-walled carbon nanotubes (MWCNTs) over carbon fiber yarns was introduced in the previous chapter. This chapter details the mechanical characterization of composites with modified interfaces using surface grown CNTs. A thin polymer sizing is applied to the fibers at the time of fiber manufacturing for fiber protection and aid in handling. However, this sizing is speculated to interact with the surface grown CNTs. The first study presented in this chapter was performed using AS4 sized fibers, whereas the second one utilized desized IM7 fibers. The first study comprises dynamic mechanical analysis (DMA) and in plane tension tests of the hybrid CNT-AS4 carbon fiber reinforced epoxy composite. The fibers were sputtered with a thin protective ceramic film prior to deposition of CNTs. Mechanical testing confirmed that the degradations in the ultimate strength as a result of the GSD process are far less than those encountered through using an alternative common technique (CCVD). Despite the minimal degradation in the storage modulus, the loss tangent for the hybrid composites utilizing GSD grown-MWCNTs improved by 56% compared to the reference samples over the frequency range 1-60 Hz. These results indicated that the energy dissipation in the GSD-grown MWCNTs composite can be attributed to the frictional sliding at the nanotube/epoxy interface and to a lesser extent to the stiff thermal shielding SiO₂ film on the fiber/matrix interface. Composites based on de-sized IM7 fibers with surface grown CNTs (second study) were tested for on-axis and off-axis tension and transverse intermediate velocity impact (IVI) resistance.

5.2 Introduction

This chapter is mainly targeted toward innovatively modified CFRPs for damping and impact resistance applications. Supplementary introductory material on enhancing inter-laminar and intra-laminar properties of CFRPs was provided earlier in chapter 3.

Random unattenuated vibrations can compromise the FRPs' structural stability and durability. Damping is essential where dynamic stability is required. It is also crucial to fatigue life and impact resistance [115]. Vibration suppression can be attained by increasing the product of the storage modulus (given by the stiffness E) and the damping capacity (given by loss tangent; $\tan\delta$). The product of these two quantities is basically the loss modulus which can be treated as a figure of merit for vibration attenuation ability [74]. Several investigations [116-119] have predicted the damping coefficients of fiber-reinforced composites considering the dissipation of energy due to fiber and matrix elastic and viscoelastic behaviors.

Vibration damping in FRPs can be enhanced by embedding a viscoelastic layer between the laminates [77]. However, the mere addition of viscoelastic polymer may lower the strength and stiffness of the composite. Therefore, further tailoring of the fiber would be necessary such that the fiber itself contributes to damping. Several approaches have been carried out to improve the FRPs' damping capabilities such as fiber surface treatment [74], interlaminar interface improvement by adding nanofillers to the matrix [76, 77, 90, 120-123], and through the addition of viscoelastic polymer particles [124]. In general, an additive or filler that is either viscoelastic or small in size is attractive for vibrations attenuation [74]. Vibration energy is dissipated through slippage and frictional interactions between the fillers and the matrix [38, 91]. The small size

fillers yield large filler-matrix interface, thereby enhancing the energy dissipation due to slippage at the interface during vibration.

Kim et al. [122] reported vibration damping enhancement of carbon fiber reinforced polymer composites when the ply interfaces were enhanced by 6.0 %wt lead zirconate titanate (PZT) particles. When plain PZT particles were distributed in the ply interfaces the loss tangent increased by almost 80%. However, the amount of improvement suddenly dropped to less than 20% with increasing of the particle loading, following a threshold effect. Han and Chung [120] investigated the effect of adding different fillers in between the lamina on the vibration damping of continuous carbon fiber composites. Exfoliated graphite as a sole filler was found to be more effective than carbon nanotube, halloysite nanotube (HNT), or nanoclay as sole fillers in enhancing the loss tangent. The MWCNT, SiC whisker, and HNT as sole fillers are effective for increasing the storage modulus. However, the combined use of a storage modulus-enhancing filler (CNT, SiC whisker, or HNT) and a loss tangent-enhancing filler (EG or nanoclay) gave the best overall mechanical performance.

The extraordinary mechanical, electrical, and thermal properties of carbon nanotubes (CNTs) have motivated researches to utilize them as a filler phase in composite materials in order to improve the properties of the host matrix. Experiments and numerical studies revealed that high aspect ratio nanofillers (e.g. carbon nanotubes (CNTs)) are more effective in dissipating energy when integrated in a composite [38, 125].

The CNTs are capable of dissipating energy when dispersed properly in a polymeric matrix [38, 42, 91]. Suhr et al. [42] conducted dynamic shear testing of epoxy thin films containing 50% volume fraction of multi-walled carbon nanotubes (MWCNTs) and reported 1400% increase in

damping ratio over the baseline epoxy resin. Koratkar et al [88] showed 1150% increase in the damping of the composites based on 2.0 wt% oxidized single-walled carbon nanotubes (SWCNTs) compared to the neat polycarbonate matrix. SWCNT composites of both stiff epoxies [125, 126] and epoxy elastomers [127] have shown to exhibit extremely high damping capacity. The energy dissipation arises from the weak bonding and interfacial friction of the nanotubes with the matrix [38, 91]. Nanotube-nanotube interactions and nanotube-matrix frictional “stick-slip” phenomenon are the dominating mechanisms for the high energy dissipation in CNT composites [2, 42, 88, 91, 125]. The damping is more pronounced when the CNT loading is near or above the mechanical percolation threshold of the composite. It is also affected by the high strain values and temperatures at which frictional sliding at the nanotube-polymer interface is activated [91, 128]. Due to the CNT high surface area, the interface sliding has a significant impact on the total damping performance of the composite. Molecular dynamics (MD) simulations have been carried out to measure the dissipated energy during the “stick-slip” motion [129]. Yap et al. [130] showed that MWCNTs exhibit negative stiffness behavior under compressive loading and are capable of significantly damping vibrations.

Thostenson et al. [10] characterized both randomly oriented and highly aligned composites containing 5.0 wt% MWCNTs in polystyrene and found almost no improvement in the loss modulus of the composite compared to the neat polystyrene matrix at room temperature. On the contrary, Rajoria et al. [128] observed a 700% increase in the damping ratio of composites based on MWCNTs compared to the neat epoxy. Such contradicting findings can be attributed to poor dispersion and deagglomeration of the CNTs in epoxy matrices.

Vibration attenuation of FRPs is another active field of research targeting FRPs with enhanced damping for various applications such as impact energy dissipation. Impact energy can be dissipated through damping provided by the viscoelastic constituents of the CFRP as well as by the frictional sliding at the interface of filler-matrix. Therefore, incorporating CNTs into FRPs can significantly improve their damping performance.

In this study, the effect of the different fiber surface treatments generated from surface coating, heat treatment, and surface grown MWCNTs on the viscoelastic properties for different composite configurations is probed. The CNTs were grown on the surface of sized and de-sized structural PAN-based carbon fiber fabrics. The mechanical performance of the CNT-carbon fiber epoxy composites was examined and its results are discussed comprehensively herein. To probe the effect of the growth temperature and technique on the mechanical properties of the composite, a separate set of samples containing surface grown CNTs was prepared using catalytic chemical vapor deposition (CCVD). On-axis and off-axis tensile, dynamic mechanical analysis (DMA), and transverse impact tests were employed to investigate the mechanical performance of the different composites samples.

5.3 Experimental methods

5.3.1 AS4 fibers with polymer sizing

Information on the AS4 fibers and fabric can be found in the previous chapter under the experimental section. A detailed description of the CNT growth procedure can also be found in chapter 4. A set of composites based on fabrics with surface grown CNTs via the CCVD technique described in chapter 4 was also prepared.

For the purpose of mechanical testing, a set of flat two-layer composite lamina of $12.5 \times 12.5 \text{ cm}^2$ were manufactured using vacuum and press-assisted hand lay-up process. The lay-up stack comprised a vacuum bag, peel ply release fabric, stacked carbon fabrics impregnated with the epoxy, another peel ply film, perforated release film, and breather cloth, sequentially. The lay-up set was vacuum bagged while a pressure of 5 kN via a dead weight was applied to it. Simultaneous use of the vacuum and dead weight assured degassing and curing of the resin while the carbon fabrics stack was kept intact under high pressure. The composite was left to cure under room temperature for 24 hours. The matrix material was Aeropoxy™ manufactured by PTM&W Industries, Inc. This epoxy system was used to manufacture both FRPs [62, 63] and composites based on SWCNT [13] and MWCNT [47]. The specimens were removed from the mold and prepared for DMA following the ASTM D4065 and D790 and for tensile following the ASTM D3039/ D3039M-08 standards. Stripes of approximately $4.0 \times 1.0 \text{ cm}^2$ with a thickness of 0.5 mm were cut from the panels and were tested using a 2.00 cm span 3-point bending clamp. Abraded G-10 tabs were attached utilizing the Aeropoxy to the ends of the tensile specimens. Tensile test coupons of $12.5 \times 1.25 \text{ cm}^2$ were cut using a saw.

DMA tests were performed using a DMA Q800 (TA Instruments, Inc.) at ambient temperature. A frequency sweep over the range of 1-60 Hz was carried out from which the storage and loss moduli were extracted. The DMA measurements were performed at a low constant strain level of 0.10%. The average values of measurements on six samples from each configuration are reported for the DMA properties of the specimens.

Ultimate tensile strength and Young's modulus for the specimens were measured from tension tests utilizing an Instron® 4400R frame. The tensile tests were performed according to ASTM

D3039 / D3039M - 08 under constant cross head speed of 2 mm/min until failure occurred. The strain was measured using an extensometer (MTS, Inc.). A total of eight samples for each configuration were tested to determine the tensile properties. A 5200 Hitachi SEM operated at 5 keV was utilized to examine the samples.

5.3.2 *De-sized IM7 fibers*

The de-sized plain-weave SGP196 (IM7-GP) fabrics (6K filaments count in tow) were provided by Hexcel. Hexcel's de-sizing process is applied to fibers to remove the sizing chemical from the carbon fiber surface. The fabrics also retained Hexcel's PrimeTex™ ZB finishing. According to the manufacturer; Hexcel : "This finishing gives a more uniform spread where the filaments in each tow are spread out creating a thinner and more closed fabric that can give better mechanicals and less porosity in a composite as well as a uniform cosmetic appearance. PrimeTex™ ZB can also be used to lower the mass in a composite where lighter weight is the key characteristic." The fiber closure before and after the ZB process are 90% and 99%, respectively.

The same CNT growth procedure, described in chapter 4, was utilized, except for shortening the synthesis to 30 min growth duration for all configurations. However, to probe the effect of the growth time a sample with an extended growth period of an hour was also prepared. The addition of the 75 nm SiO₂ thermal barrier layer alters the interface between the polymer, CNTs, and the fiber. Therefore, samples with surface grown CNTs over SiO₂ coated fabrics as well as over the as is fibers were prepared. In addition, coarse and fine mesh templates were used to selectively sputter the nickel catalyst film on top of the fabrics. This enabled growth of a checkerboard pattern of CNTs over the fabrics. The two mesh discs employed are shown in Fig. 5.1. The

coarse mesh retained a thread size of 400 μ , opening size of 840 μ , and an open area of 46%. The fine mesh, however, possessed a thread size of 76 μ , an opening size of 140 μ , and an open area of 24%.

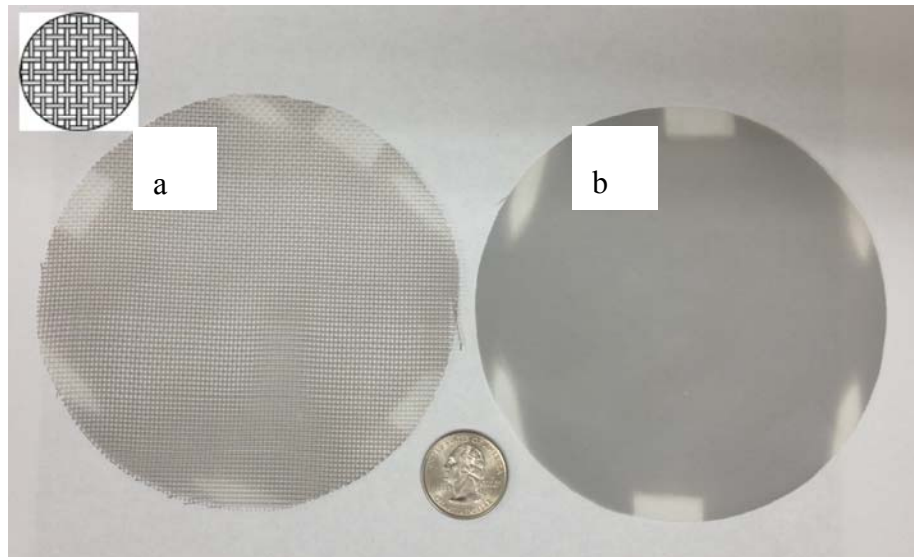


Fig. 5.1. Polyester mesh discs; a) thread size 400 μ , opening size 840 μ , and an open area of 46% and b) thread size 76 μ , opening size 140 μ , and an open area of 24%. Inset: mesh pattern showing the threads and open areas.

For the purpose of mechanical testing, a set of flat three-layer composite lamina of 12.5×12.5 cm² were manufactured using the fabrication process explained in chapter 3. Five-layer panels were fabricated for impact tests. The impact tests were followed utilizing the procedure described in chapter 3. The tensile tests were performed in the fiber direction (i.e. on-axis) and in a 45° angle from the fibers direction (i.e. off-axis).

5.4 Results and discussion of composites based on sized AS4 fibers

Mechanical testing results (sized AS4 fibers)

The stiffness of the two-lamina composites is governed by the carbon fiber's core and hence is less likely to be affected by the elevated temperatures of CCVD and GSD if an inert atmosphere is employed. However, the tensile strength is highly influenced by the quality of the surface of the carbon fibers and the goodness of the adhesion (uniform stress transfer) between matrix and fibers. Therefore, the ultimate tensile strength is expected to be affected by the coating, heat treatment, and CNT growth.

The morphology, length, and density of the grown CNTs are speculated to affect the polymer matrix infusion into the CNT layer and subsequently the interfacial bonding at the fiber/epoxy interface. Fig. 5.2 shows a cross sectional SEM micrograph of a carbon fiber covered with a dense layer of GSD-grown CNTs. The CNTs layer seems to be coherent and bonded to the surface of the fibers. However, to attain a good adhesion between the polymer/fiber it is very critical that the polymer matrix infuses into the dense CNT forest. The thickness of the layer (1 hr growth time) is almost 0.5 microns. The length of the grown CNTs can be controlled by the initial thickness of the nickel layer and the growth time.

Carbon nanotubes only grow on the sides of the woven carbon fabrics (ply interfaces in a composite lamina). However, they did not influence the polymer matrix penetration to the regions adjacent to the grown CNTs (see Fig. 5.3). As observed from the SEM micrographs of the cross sections of different samples, Fig. 5.4, the overall penetration of the matrix seems to be identical for all the samples. However, while grafting of CNTs was achieved with the minimal weight penalty, it affected the volume fractions of the composite panels. The volume fractions for different composite configurations are summarized in the

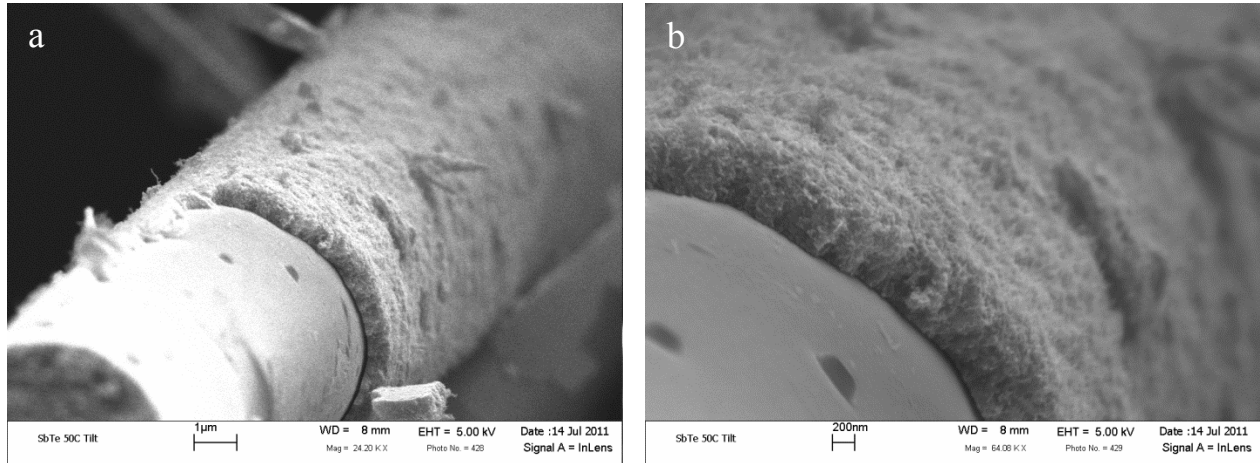


Fig. 5.2. Cross-sectional micrograph of a carbon fiber grafted with surface grown CNTs utilizing the GSD technique

Table 5.1. Fiber volume fractions for the specimens based on raw PAN-based carbon fabric (Raw), SiO₂ sputter-coated fabric (Sp), heat treated fabric (HT), SiO₂ sputter-coated then heat treated fabric (Sp+HT), and the samples with CNTs grown on their surfaces via GSD (GSD) and CCVD (CCVD).

Sample	V _f (%)
Raw	56
Heat treated (HT)	57
SiO ₂ sputter-coated (Sp)	55
SiO ₂ sputter-coated then heat treated (Sp + HT)	54
CNT grown with GSD (GSD)	49
CNT grown with CCVD (CCVD)	49

The tensile test results were, therefore, normalized with respect to the corresponding volume fractions according to the composites rule of mixture. Although, the rule of mixture does not provide the most accurate prediction of tensile properties, it is employed here to justify the comparison between the different samples and to provide a better contrast of the effects of the different surface treatments on the tensile properties. The results of the tension tests are summarized in Table 5.2.

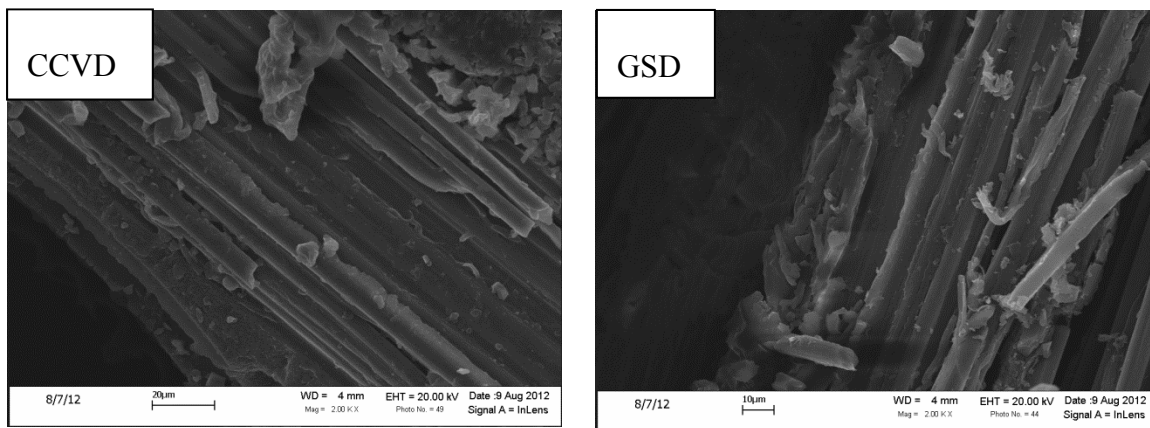


Fig. 5.3. polymer matrix penetration of the region adjacent to the CNTs for the composites based on GSD and CCVD methods.

The normalized results indicate that the stiffness of the composite was retained upon the exposure to high temperatures (i.e. 550 °C in N₂ atmosphere). This observation is manifested by the HT and the HT+Sp samples. The surface alteration via coating with SiO₂ and heat treatment or the presence of GSD-CNTs on the surface resulted in an increase in the stiffness (see Table 5.2). However, the sample with CCVD grown CNTs on SiO₂ layer exhibited a slight degradation of almost 4% in the stiffness of the corresponding composite. This degradation can be attributed

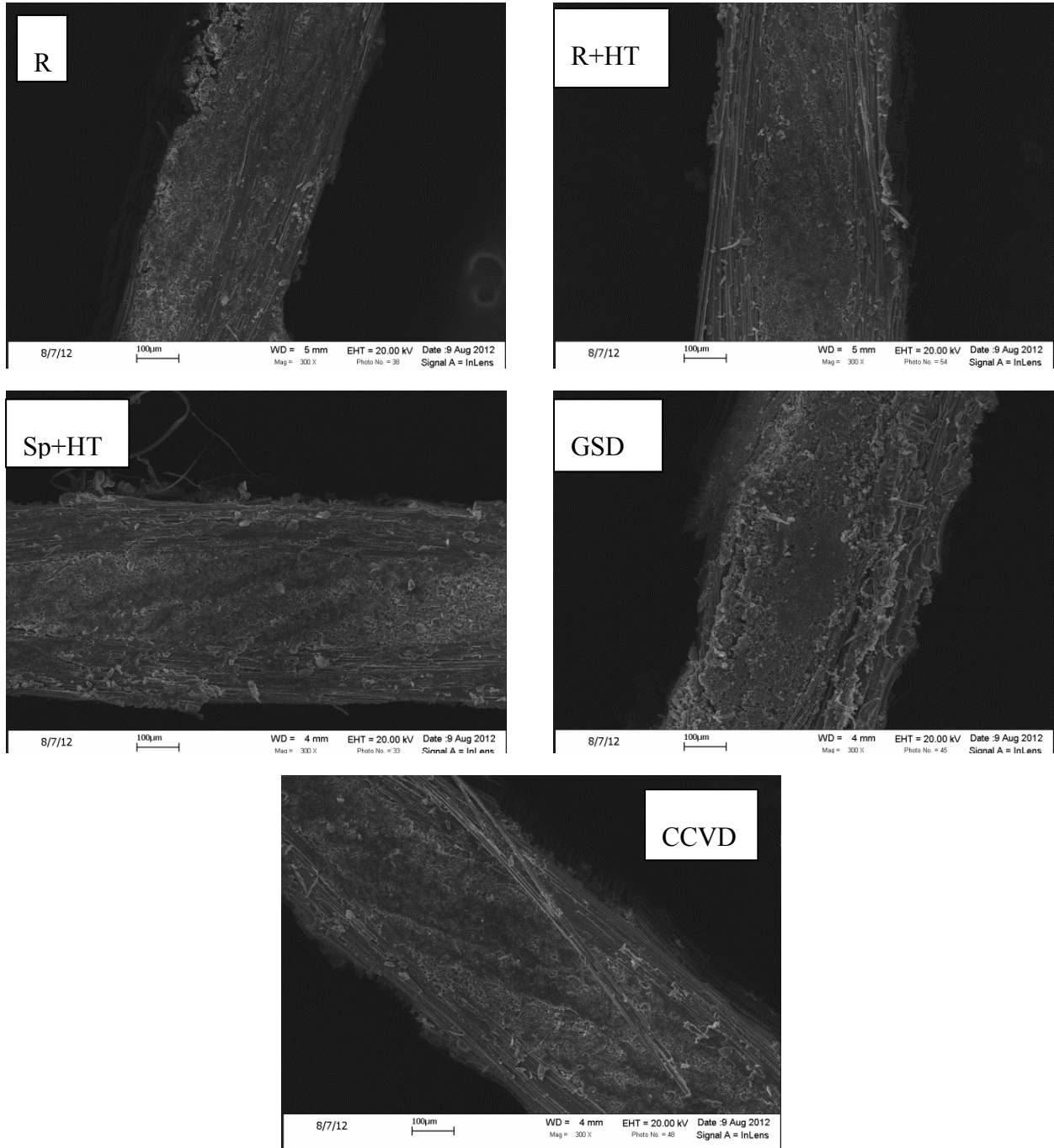


Fig. 5.4. The cross sections of all fabricated composite samples were investigated under scanning electron microscopy (SEM). The cross sectional images of all samples as well as magnified images for the GSD and CCVD samples are shown below. The SEM micrographs show the same level of matrix penetration for all samples.

to the higher temperature of the CCVD reaction that accelerates carbon diffusions and partially deteriorates the carbon fiber and -to a lesser extent- to the poor adhesion between the epoxy/fibers and CNT/fiber.

Heat treatment of the carbon fabric also leads to the removal of the sizing and thus alteration of the surface of the fibers. Removing the sizing through heat treatment resulted in an 8% reduction in the strength of the composite compared to the reference composite with the sizing intact; Table 5.2. The introduction of the SiO₂ layer (Sp sample) lessens the bonding between the epoxy and fibers and thus induces a slight reduction in the strength of the composite. The heat treatment of the sputter-coated fabrics (see the SP+HT sample) does not appear to influence the adhesion of fiber/matrix and the strength of the composites; the strength of the Sp and the Sp+HT composites were virtually identical. Grafting CNTs directly onto the fibers allows for placement of high volume fractions of un-agglomerated CNTs. This volume fraction is far larger than what can be effectively achieved when CNTs are pre-mixed with the epoxy matrix. It is speculated that the highly viscous matrix (viscosity of 950 cps) might not be efficient in fully impregnating the dense surface grown CNT forests. Conversely, the enhanced fiber/matrix adhesion due to the interactions between the surface grown CNTs and the polymer matrix yielded an improved stress transfer to the fibers compared to all other samples with modified surfaces (i.e. Sp, Sp+HT, and HT). The composite based on the GSD grown CNTs counterbalanced some of the undesired effects from the presence of the SiO₂ layer and heat treatment on the strength. While the strength of the GSD samples improved by 5% compared to the Sp+HT ones, it was still 3.5% lower than the strength of the reference samples. Nevertheless, the harsh thermal environment of CCVD (i.e. exposure to the temperature of 680 °C) causes drastic degradation of the fibers due to

temperature-accelerated diffusion of carbon which deteriorates the carbon fiber core and surface. Moreover, the surface of the fibers is malformed due to the presence of CNTs (possibly not fully attached to the fiber) on the surface of the SiO₂ coated carbon fibers. Test coupons based on FRPs with CCVD surface grown CNTs ruptured in a very brittle manner. A 70% decrease in the strength of the composites based on CCVD-CNTs can be primarily attributed to the severe degradation of the fiber surfaces due to the elevated synthesis temperatures. Among the tested samples only the SiO₂ coated (Sp) and SiO₂ coated/heat treated (Sp+HT) samples exhibited delamination during the tension tests.

Table 5.2. Tensile mechanical properties for the specimens based on raw PAN-based carbon fabric (Raw), SiO₂ sputter-coated fabric (Sp), heat treated fabric (HT), SiO₂ sputter-coated then heat treated fabric (Sp+HT), and the samples with CNTs grown on their surfaces via GSD (GSD) and CCVD (CCVD).

Fiber's Configuration	Young's Modulus (GPa)	Tensile Strength (MPa)
Raw	40.4±1.2	606±31
HT	41.4±0.9	556±44
Sp	40.6±3.6	547±42
Sp+HT	44.1±1.4	557±27
GSD	43.7±2.6	585±37
CCVD	38.9±4.8	184±10

The carbon fiber samples were weighed pre and post processing in the synthesis reactor. The measurements were repeated for the samples with SiO₂ coating only (Sp+HT sample was considered as the reference for calculating the weight of CNTs) and for the samples with SiO₂ coating and nickel catalyst (the ones that CNTs grow on later). Utilizing a digital scale with an

accuracy of ± 0.0001 g, we conclude that for both samples processed via GSD and CCVD, the weight fractions of the CNTs in the composite is less than 0.05 wt%.

The hand layup process that was used for fabrication of the panels does not effectively control the volume fractions of composites. However, the normalized tensile test results confirmed the hypothesis that the core of the fibers is unaffected by the elevated reaction temperatures of both GSD and CCVD. Among all the samples, the tensile strength of the panels fabricated from the CCVD processed fabrics degraded significantly. Thermally induced surface damage to the fiber surface and the weak interaction between the surface CNTs and polymer matrix are the main culprit for the mechanical weakening of the CCVD composite samples. The conclusion that can be drawn is that the CCVD technique allows for placement of higher quality CNTs (compared to GSD) at the price of significantly degraded mechanical properties.

The reduction of tensile properties of the GSD samples, table 2, is at worst 3.5 % for the strength. The CCVD yielded even more significant reductions of 4% and 70% for the modulus and the strength, respectively. The degradation of the composites properties due to thermal annealing of the base carbon fibers during CCVD was observed by several other groups. For example when utilizing CCVD for growing CNTs on the surface of IM7 carbon fibers (much stronger and denser than the AS4 fibers) at 750 °C for 1 hr, Qian et al. [131] reported a 15-25% reduction on the tensile strength. Zhang et al. [25] performed a CCVD to grow CNTs over T650 and IM7 carbon fibers and observed that the strength of the corresponding composite based on T650 fibers with grafted CNTs- compared to composite based on the raw fibers- drop by 46% when the growth temperatures was 800 °C. In contrast, under the same growth conditions the

composites based on IM7 carbon fibers with grafted CNTs exhibited a reduction by 70% of the original strength.

The DMA results over the frequency range of 1-60 Hz are shown in Fig. 5.5, Fig. 5.6, and Fig. 5.7, respectively. Clearly, the measured storage modulus for all composite samples exhibited a frequency-independent behavior. In theory, both the loss and storage moduli should be frequency-dependent for a viscous fluid or a viscoelastic material, which is typically manifested by a Deborah number; $De \leq 1.0$; ratio between the viscoelastic stress relaxation time and the time of observation via DMA [132]. The storage modulus changes as a function of the frequency to a higher degree in viscoelastic materials than in elastic ones. As the material becomes more elastic (through adding elastic filler such as high volume fraction carbon fiber and surface grown CNTs), the viscoelastic (time-dependent) behavior diminishes, and, the frequency-dependence of the storage modulus is vanished. Such observation was reported for carbon fiber composites with different fibers orientation [115] within a range of frequencies. The results for the storage moduli of different specimens, Fig. 6, as expected, confirmed those obtained from the tensile test.

The DMA results for the loss tangent and the corresponding loss modulus over the frequency range of 1-60 Hz are shown in Fig. 5.6 and Fig. 5.7, respectively. Unlike the storage modulus, the loss modulus and the loss tangent were highly frequency dependent, since they are driven by the material's viscoelastic behavior. Similar to this article's findings, room temperature loss tangent values of less than 0.1 were reported for carbon, Kevlar and glass fiber FRPs in flexure mode DMA [133]. In addition, the loss tangent of a PEEK/IM7 CFRP was also shown to depend on frequency over the 0.1-10 Hz range at room temperature [115].

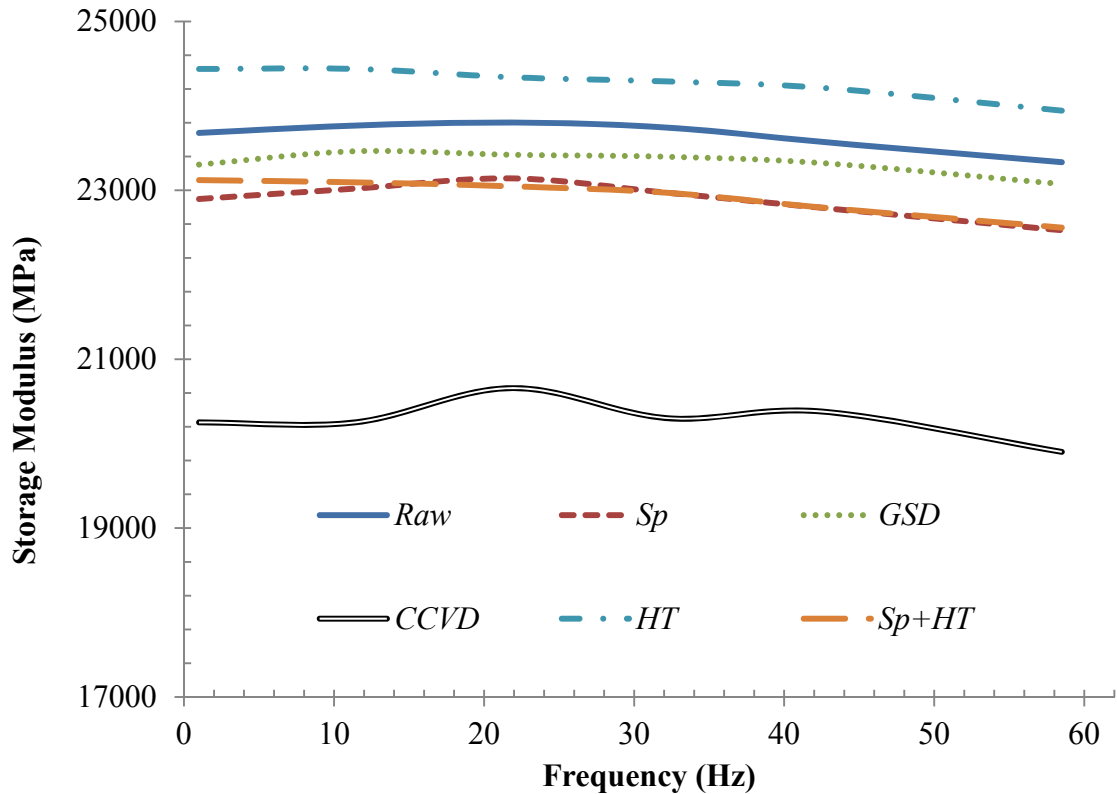


Fig. 5.5. The storage modulus for composites made out of Raw (reference raw fabric), HT (heat treated fabric), Sp (sputter-coated fabric), Sp+HT (sputter-coated and then heat treated fabric), GSD (sputter-coated sample with CNTs using the GSD method), and CCVD (sputter-coated sample with CNTs using the CCVD method).

Based on the loss tangent and the loss modulus measurements, Fig. 5.6 and Fig. 5.7, the addition of the hard SiO₂ film promoted the mechanisms by which the composite dissipates energy. The interface is the main source of difference in energy dissipation levels in the ceramic coated and raw specimens. Furthermore, altering the fiber surface via heat treatment of the raw fabric or via adding a ceramic coating does not affect the damping response of the composite. Through growing MWCNTs utilizing GSD on top of the PAN-based carbon fibers coated with SiO₂ films, the loss tangent of the produced composite increased significantly (e.g. 120% increase at 32 Hz compared to raw fiber based composite). On the contrary, the average loss tangent (over 1-60

Hz) of the composite sample with CCVD-grown CNTs has the lowest average value compared to all other samples (Fig. 5.6). Although, the loss tangent and modulus exhibit nonlinear frequency dependent behaviors, same frequency dependent pattern is observed for all of the samples exclusive of the one based on the fabric with CCVD surface grown CNTs. This variance can be ascribed to the extreme degeneracy of the fiber outer shells and structure owing to the intense CCVD temperatures; the carbon fiber abandoned the viscoelastic behavior.

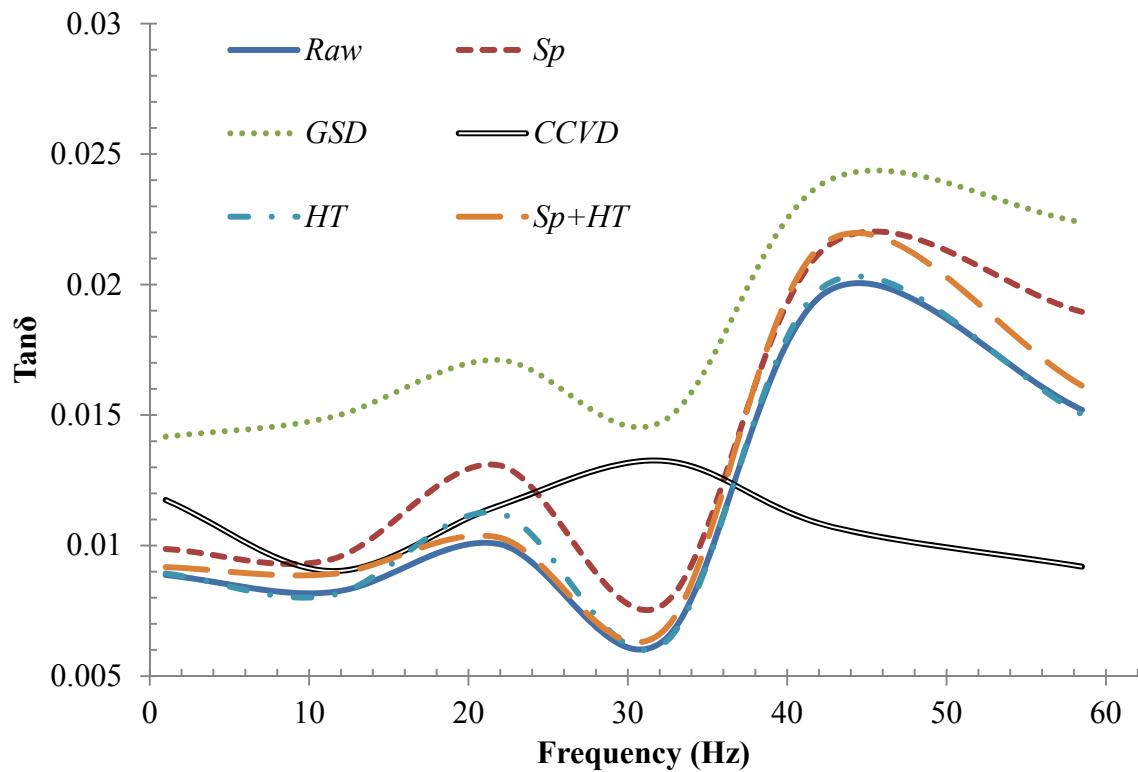


Fig. 5.6. The loss tangent for composites made out of Raw (reference raw fabric), HT (heat treated fabric), Sp (sputter-coated fabric), Sp+HT (sputter-coated and then heat treated fabric), GSD (sputter-coated sample with CNTs using the GSD method), and CCVD (sputter-coated sample with CNTs using the CCVD method).

The addition of the thin SiO₂ layer slightly increased the loss modulus of the raw fibers. Furthermore, the applied strain level (0.1 %) is too small to activate all the mechanisms of

energy dissipation via viscoplastic deformation at the CNT/epoxy interface [42, 88], yet the loss tangent of the hybrid composite has noticeably increased. Thus, one can conclude that partial activation of frictional sliding of nanotube/polymer along with the coating effect on the interface region are the two leading mechanisms that are responsible for the higher loss modulus of the hybrid composite. The higher temperature encountered during the CCVD process degraded the PAN-based carbon fibers and the net effect of CNT/epoxy sliding and mechanical degradation rendered a total decrease in loss tangent value of the composite using the CCVD-grown MWCNTs.

As there are currently no published literature regarding the damping behavior of composites comprising carbon fibers grafted with CNTs, the natural comparison of this work would be to the composites incorporating CNTs as additive to the matrix. For this family of composites, upon adding CNTs the storage modulus either does not change or improves slightly. However, these improvements are reported for much higher loading of the CNTs than that reported in our work (0.05 wt%). For example, Khan et al. [90] incorporated 1.0 wt % MWCNTs into an epoxy matrix then utilized it with prepregs of carbon fiber reinforced composites. The specimens were tested in both free and forced vibration modes. The free vibration test indicated that the damping ratio of the CFRP-CNT hybrid composites increased by 15% over the neat CFRP. Han and Chung [120] fabricated a composite based on FRP with 0.8 wt% MWCNTs and reported improvements on the storage modulus and the loss modulus of 48.8%, and 28%, respectively. However, they reported a 14% reduction in the loss tangent.

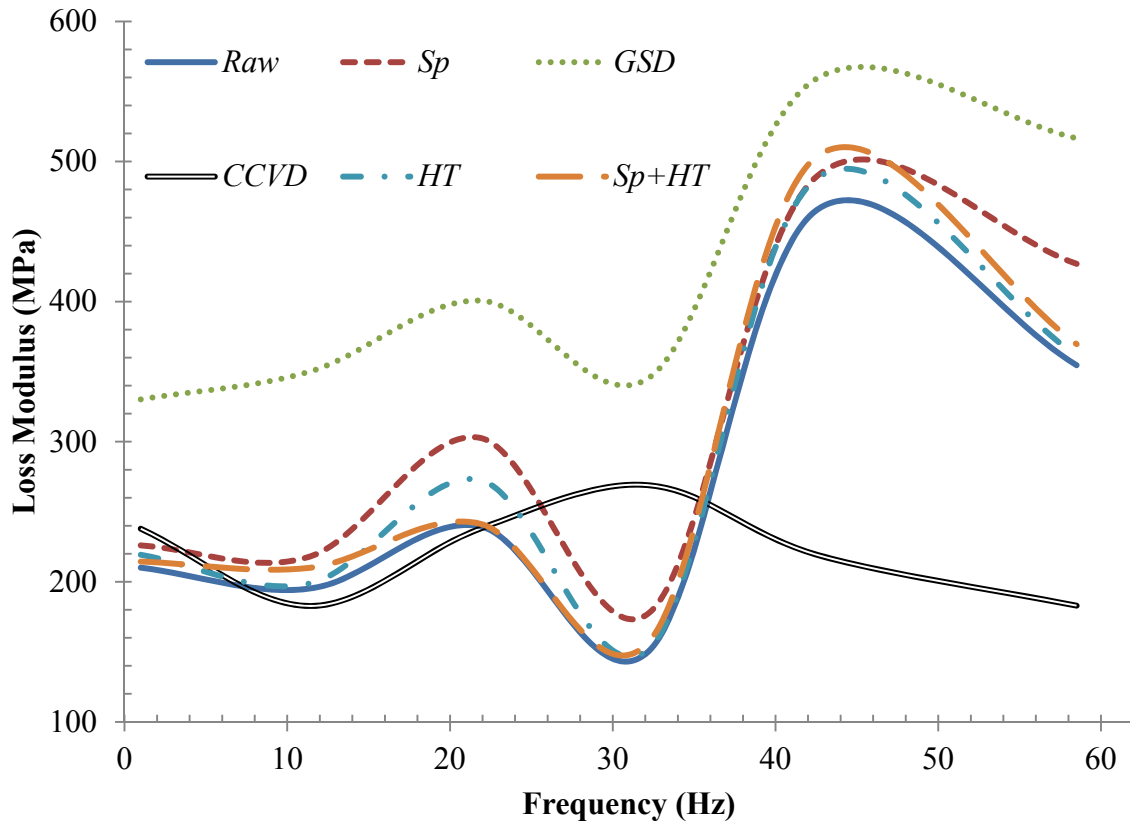


Fig. 5.7. Loss modulus measurements for composites made out of Raw (reference raw fabric), HT (heat treated fabric), Sp (sputter-coated fabric), Sp+HT (sputter-coated and then heat treated fabric), GSD (sputter-coated sample with CNTs using the GSD method), and CCVD (sputter-coated sample with CNTs using the CCVD method).

5.5 Results and discussion of composites based on the de-sized IM7 fibers

A thin layer of polymer sizing is usually applied to the surface of carbon fibers for better handling of the fibers, protecting the fiber from humid and oxidizing environments, and to enhance the adhesion between the fiber and matrix. Prior to deposition of CNTs via GSD or CCVD, a thin SiO₂ layer can be applied to the surface of the fibers to thermally shield them from the elevated temperatures of CNT growth and to prevent the diffusion of the carbon/catalyst particles. The interface of the fiber and the CNT layer is affected by the existence of the polymer

sizing and/or the SiO₂ thermal barrier. However, according to the micrographs of Fig. 5.8 there was no visual evidence of any effect on the CNT growth coverage and morphology for sized and de-sized IM7 fibers whether they were pre-sputtered with SiO₂ or not.

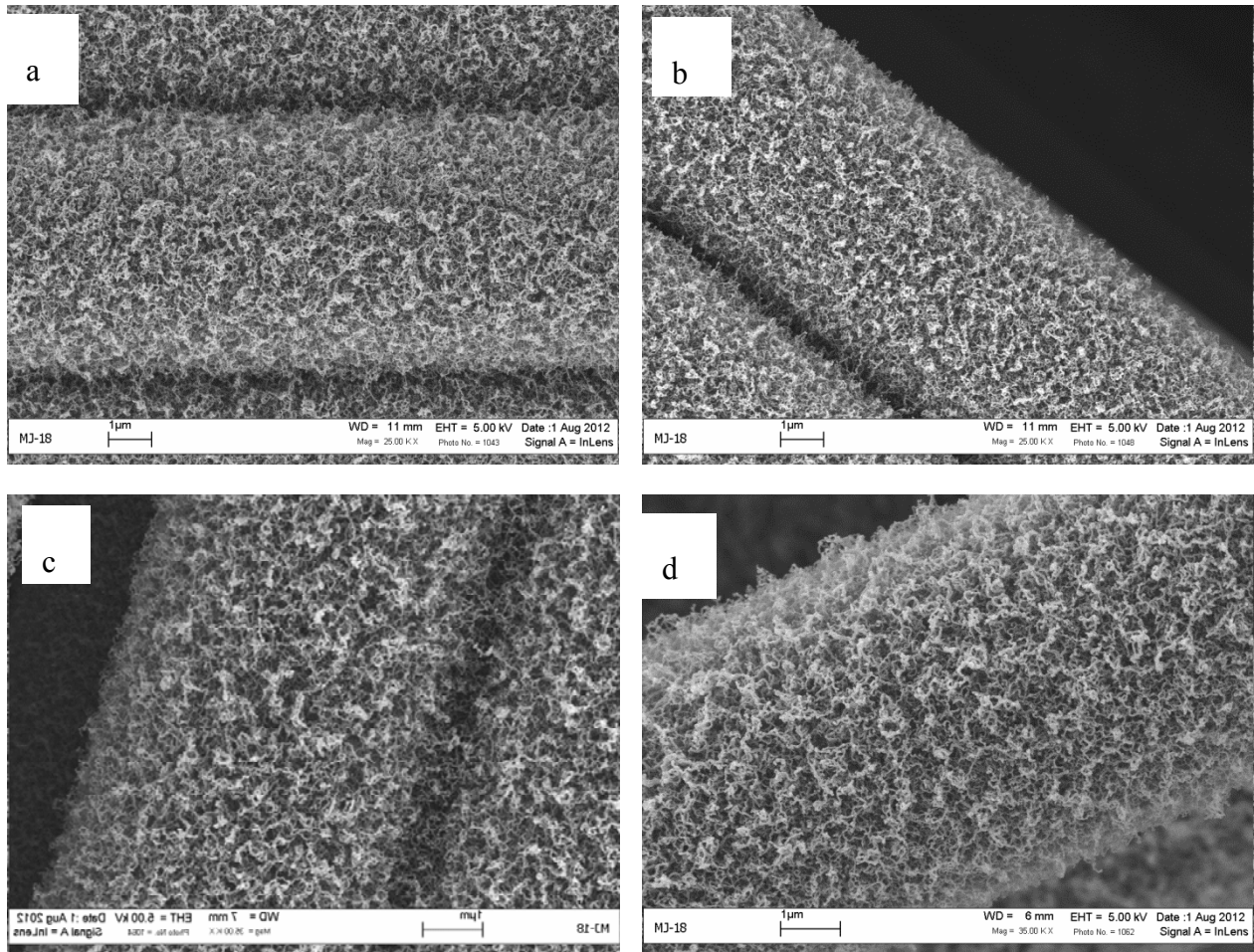


Fig. 5.8. SEM micrographs of GSD surface grown CNTs on (a) de-sized fibers, (b) sized fibers, (c) sized and SiO₂-coated fibers, and (d) de-size fibers

Fiber volume fraction and matrix penetration and in a CFRP in areas adjacent to the modified surfaces (sides of the fabrics) are likely to be affected by the altered interfaces. The impregnation of the fibers with the epoxy matrix at the lamina interfaces for the reference raw and GSD

samples are shown in Fig. 5.9. In addition, the fiber volume fractions were also almost not influenced by any of the surface modifications. Table 5.3 summarizes the fiber volume fractions for all different configurations that were the subject of this experiment. The slight variations in the fiber volume fraction are due to the fabrication method rather than any effect from the fiber surface modifications.

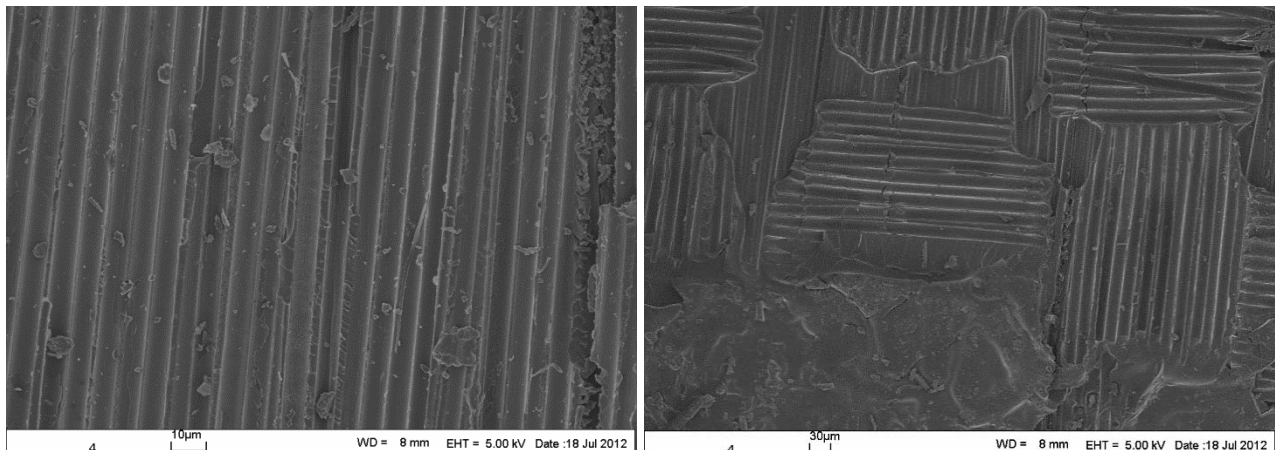


Fig. 5.9. Impregnation of surface fibers with the epoxy matrix for composites based on raw fibers (left) and fibers with surface grown CNTs (right)

The results of the tensile mechanical properties for different configurations modified fibers are plotted in Fig. 5.10 and Fig. 5.11. These results are normalized with respect to the corresponding fiber volume fraction values. Tensile properties for the woven composite systems are direction dependent. For example, the stiffness is controlled by the core structure of the fibers in the on-axis direction. However, their off-axis stiffness is influenced by the stiffened modified interfaces. All samples retain nearly identical Young's modulus in the on-axis direction. Therefore, it can be speculated that their fiber core structures, even after exposure to the elevated growth conditions, are unchanged. The off-axis stiffness results of Fig. 5.11 revealed that the high temperature of the growth marginally weakness the fiber/matrix interface resulting in an inclined stiffness value.

However, the surface grown CNTs stiffened the interface leading to a 12% increase in the off-axis Young's modulus of the GSD sample compared to the reference raw sample.

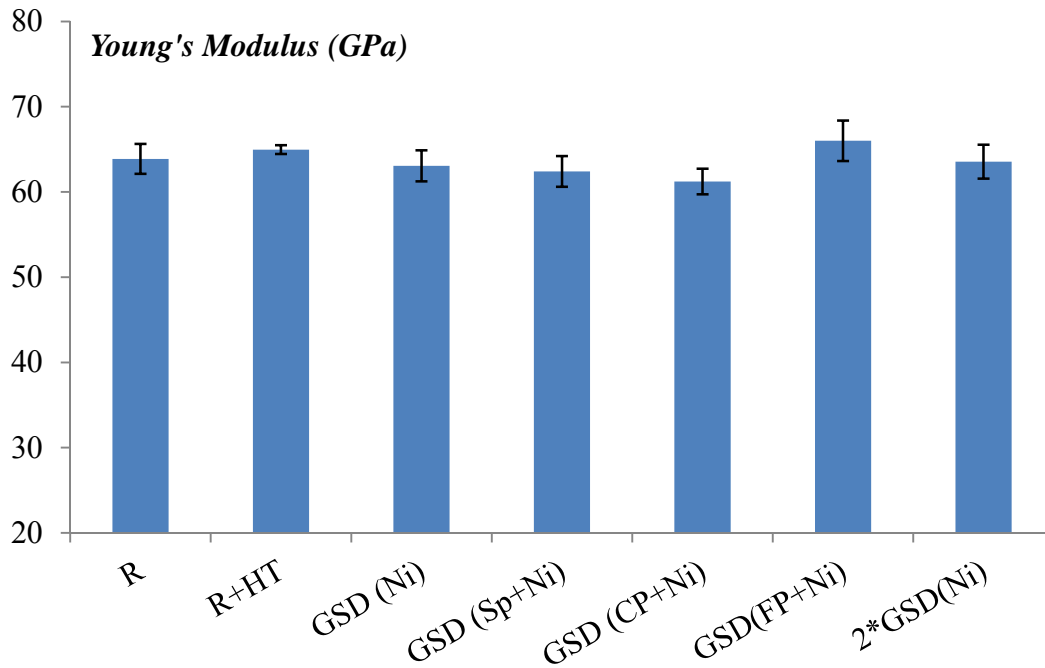
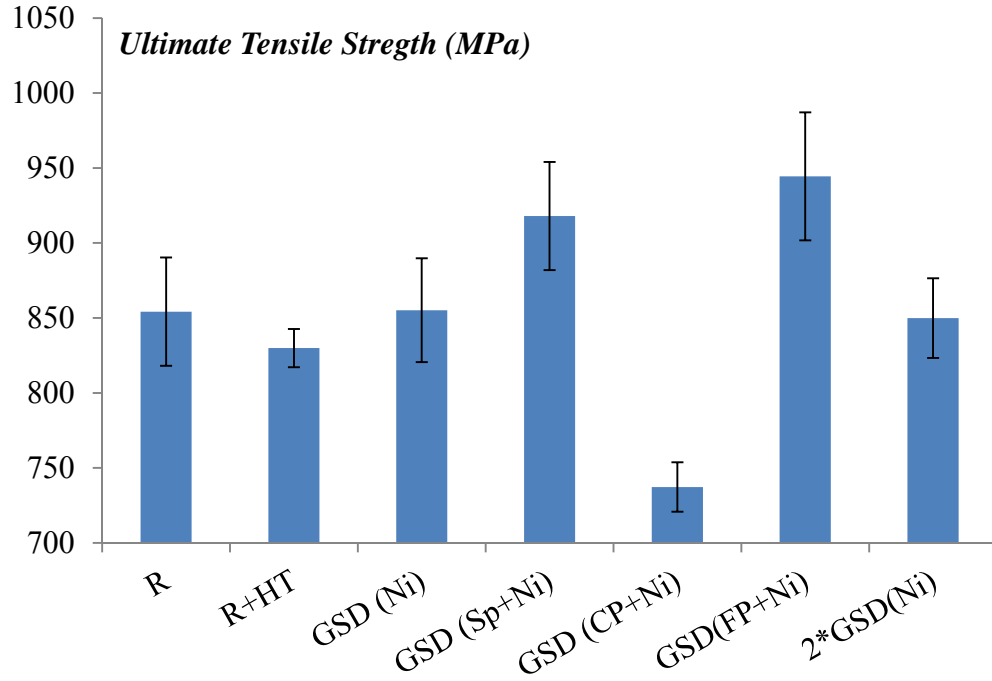
Table 5.3. Fiber volume fractions for composites based on raw (R) and heat treated (HT) fibers, fibers with surface grown CNTs via GSD (GSD(Ni)), fibers with predeposited SiO₂ coating and surface grown CNTs via GSD (GSD(Sp+Ni)), fibers with a coarse mesh (pattern) surface grown CNTs via GSD (GSD(CP+Ni)), fibers with a fine mesh (pattern) surface grown CNTs via GSD (GSD(FP+Ni)), and fibers with surface grown CNTs via GSD that were grown for an hour compared to the half hour growth time utilized in all other configurations (2*GSD(Ni)).

	RAW	HT	GSD (Ni)	GSD (Sp+Ni)	GSD (CP+Ni)	GSD (FPG+Ni)	2* GSD (Ni)
V _f (%)	62	62	63	64	66	62	61

One traditional weakness of the composites has been their ineffectiveness in uniformly transferring stresses to the fibers. These stresses are transferred through the matrix to the fibers and a strong bonding between the fiber and matrix is essential to achieve high strength levels. All the proposed surface modifications of this study alter the interface and consequently the strength of the fiber/matrix interface. For both on and off-axes tests, the ultimate strength for the samples based on heat treated fibers slightly decreased. The CNT layer however, compensated for this undesired decline in the strength and the strength of the samples based on the GSD grown fibers are identical to that of the reference raw samples in both on-axis and off-axis direction.

Growing CNTs on SiO₂ coated fibers resulted in an enhanced tensile strength and failure strain by 7% and 34% in the on-axis direction compared to the reference sample. This can be due to protection effect of the ceramic thin film and also its role in inhibiting diffusion of material into and from the surface of the fibers.

The mechanism of strengthening of the composites with the surface grown CNTs relies on a locking mechanism between the polymer and the CNTs and also stiffening of the interface (as a result of CNT enriched interface). Nevertheless, as it is observed in Fig. 5.2 and Fig. 5.8, the CNT layer is very dense and the impregnation of the epoxy into this compacted CNT layer is essential for improved mechanical properties. Various strategies as to grow the CNTs in a coarse and fine sized checkerboard pattern and also to vary the CNTs length by changing the growth time were sought. While increasing of the growth time (longer CNTs) and depositing the CNTs in a widely spaced pattern did not enhance the tensile properties, fine patterning of the CNT layer resulted in moderate tensile properties improvement; the failure strain and ultimate strength in the on-axis direction were improved by 17% and 12%, respectively, compared to the reference samples.



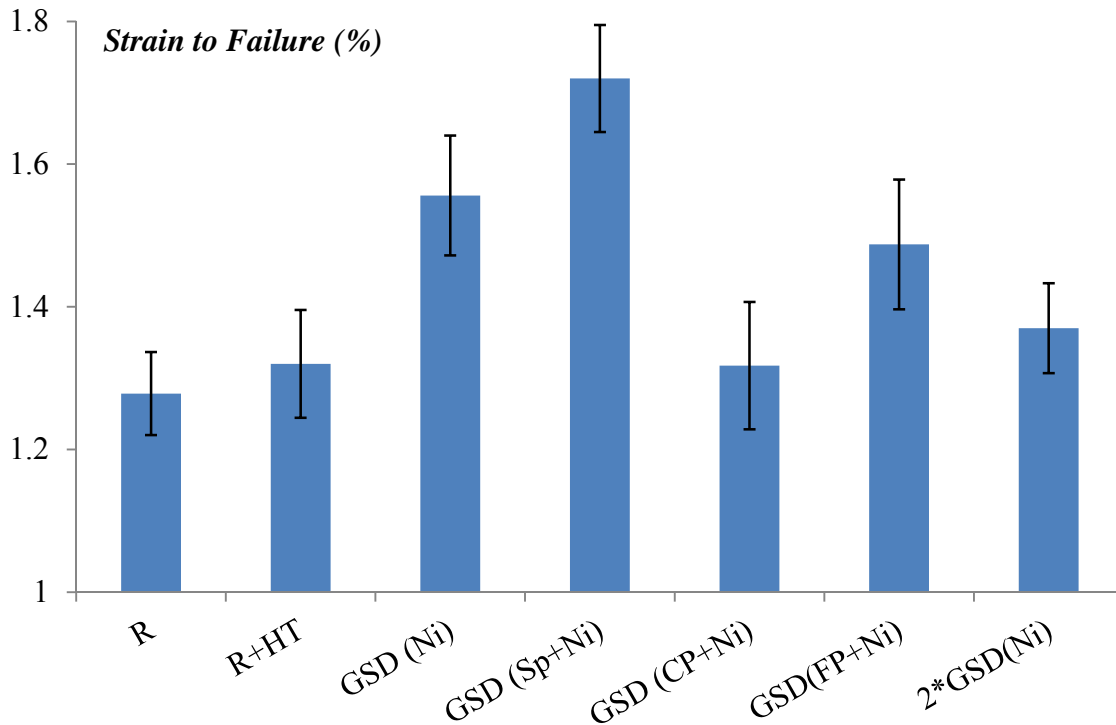


Fig. 5.10. On-axis tensile properties of the composites based on raw (R) and heat treated (HT) fibers, fibers with surface grown CNTs via GSD (GSD(Ni)), fibers with predeposited SiO₂ coating and surface grown CNTs via GSD (GSD(sp+Ni)), fibers with a coarse mesh (pattern) surface grown CNTs via GSD (GSD(CP+Ni)), fibers with a fine mesh (pattern) surface grown CNTs via GSD (GSD(FP+Ni)), and fibers with surface grown CNTs via GSD that were grown for an hour compared to the half hour growth time utilized in all other configurations (2*GSD(Ni)).

The addition the CNT layer in most configurations increased the strain to failure of the composite. It also improved the strength of the sample in the off-axis direction. Hence, it can be predicted that the samples containing GSD-grown CNTs possess higher toughness (energy under a stress-strain tensile curve). In addition, CNTs have shown to be capable of attenuating stress waves by slipping mechanisms at their interface with the polymer matrix. However, the stiffness of the fiber/polymer interface should be optimized for an efficient stress transfer and crack

resistance. Hence, it is very difficult to predict the impact behavior of the hybrid composites merely based on their quasi-static performance.

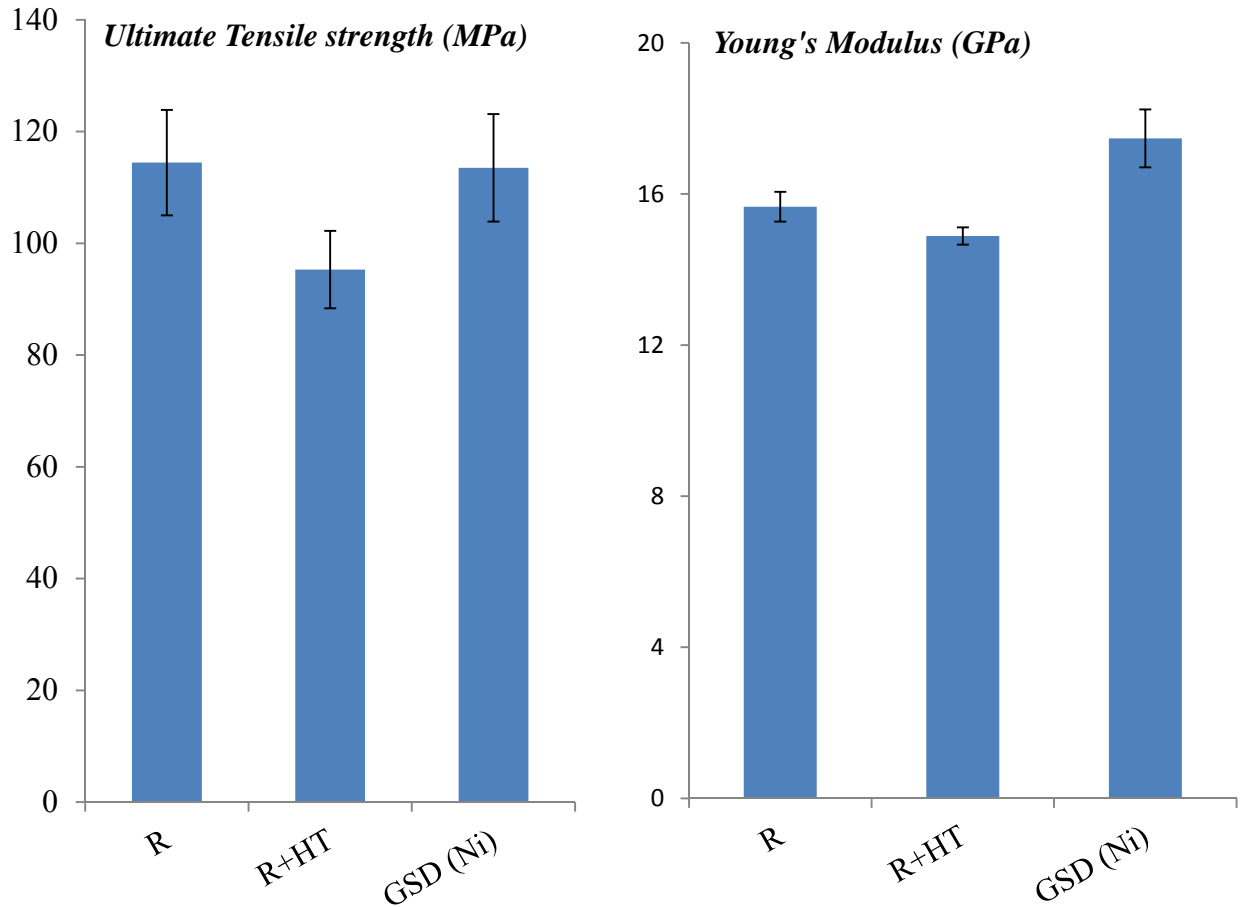


Fig. 5.11. Off-axis tensile properties of the composites based on raw (R) and heat treated (HT) fibers as well as fibers with surface grown CNTs via GSD (GSD); no SiO₂ was predeposited onto the fibers.

The incident and residual velocities of the transverse impact testing of the composites based on raw fabric and fabric with surface grown CNTs are summarized in Table 5.4. The impact

energies for the tests are also evaluated based on the impactor speed before and after the ballistic perforation. A 76% improvement in the absorbed energy of the plates was observed as a result of adding the CNTs to the surface of the fabrics. The improved interlaminar properties, strain to failure and toughness are some of the factors that contribute to this significantly enhanced impact resistance.

Table 5.4. Transverse impact incident and residual velocities and the calculated absorbed energy by the reference composite based on raw fabric and the hybrid composite based on fabric with surface grown CNTs via GSD (no SiO₂ layer was applied)

	Reference				Hybrid			
Incident velocity (m.s ⁻¹)	98.62	98.41	98.97	93.51	94.33	102.26	99.77	98.5
Residual velocity (m.s ⁻¹)	88.54	86.74	89.51	84.01	72.6	83.32	83.24	81.39
Absorbed impact energy (Joules)	7.55	8.64	7.13	6.75	14.51	14.06	12.10	12.31

5.6 Conclusions

The surface modification of the carbon fiber through heat treatment, coating with SiO₂ film, and growing MWCNTs via GSD or CCVD on the surface can affect, differently, both the static and dynamic behaviors of the composites based on these different fiber configurations. The tensile and dynamic mechanical analysis showed that composites using the GSD-grown CNTs

outperform those using the CCVD grown CNTs in terms of stiffness, tensile strength, and damping. The conclusion that can be drawn is that the CCVD technique allows for placement of higher quality CNTs (compared to GSD) at the price of significantly degraded mechanical properties. The tensile results indicated that the SiO₂ thin film protected the PAN-based carbon fiber against undesired diffusions and the temperatures utilized in GSD technique (550 °C), but were not capable of shielding the fibers at higher temperatures used in the CCVD method. In addition, these films were capable of promoting the energy dissipation mechanism by enhancing the loss tangent over that for raw fibers. Based on the DMA results for the composite incorporating the fiber/GSD-grown MWCNTs hybrids, the leading mechanisms for energy dissipation can be attributed to the frictional sliding of MWCNT/epoxy and to a lesser extent due to the stiff SiO₂ coating on the interface region. The ultimate strength and damping frequency dependent behavior of all specimens were similar, whereas the composite made out of CCVD-grown CNTs exhibited a very low tensile strength compared to the other samples and also an utterly dissimilar frequency dependent damping behavior. These discrepancies are owed to the changed core structure of the fibers due to the elevated CCVD temperatures.

The reductions in the strength encountered by the fibers via the GSD growth are not desirable and yet are negligible (only a 3.5 % reduction in strength compared to the reference samples). This trend was observed by the different groups who have utilized CCVD to grow CNTs on the surface of carbon fibers. However, the figure of merit for damping as manifested by the loss tangent and loss modulus showed significant improvements despite the weakening of the composite. The published literature indicates that investigations involving mixing of CNTs with the epoxy matrix achieved improved damping at much higher wt% of CNTs. Therefore, it is

believed that the GSD still needs further optimization in terms of the growth temperature and the shielding of the base fibers. However, the GSD is still providing promising results for vibration damping at minimal CNTs content of only 0.05 wt %.

Results of the mechanical tensile tests of CNT-modified IM7 de-sized FRPs provided valuable information on the use of protective ceramic layer, patterned growth CNTs and CNT length on the properties of the resulting composite. The GSD-CNT layer toughened interfaces and resulted in significant improvements over reference composites based on de-sized IM7 fibers.

Based on these results, further optimization of the growth time, patterning, and ceramic coating of the fibers is required to fully materialize the potential benefits of the GSD technique.

Chapter 6. Modeling of the Impact of Carbon Fiber Reinforced Panels Considering Impact Progressive Damage and Strain-Rate Effects

6.1 Overview

The finite element method (FEM) is the most used simulation tool for designing of complex structures. Emerging of massively parallel processor (MPP) computers with powerful computational capabilities has made viable the simulation of large-scale highly nonlinear problems. Simulating the response of FRPs under impact loads is crucial since the damage evaluation based on experimental work can be excessively expensive; if feasible. This chapter details an attempt to simulate the ballistic impact characteristics of a thin hybrid CFRP using explicit LS-DYNA FEM package. The MAT162 material model is utilized for modeling the composite response. This material model accounts for strain rate dependent behavior and progressive damage in the composite [134]. Input parameters to the MAT162 are either measured directly from simple quasi-static tests or calibrated based on more complex quasi-static shear punch tests (QSSPTs). The results of the numerical simulations are compared to the impact experiments performed on the CFRPs with identical geometries. Response of the CFRPs to a high velocity impact (100ms^{-1}) is discussed in terms of the impact absorbed energy sensitivity to different parameters used in the material model. This chapter entails, for the first time, FEM simulation of a thin CFRP using MAT162.

6.2 Introduction

It is rather costly to construct and test prototypes or full-scale structures for destructive mechanical evaluation. With the emerging of powerful massively parallel processor (MPP) computers, simulating the response of structures has led to significant cost savings and better understanding of the mechanical response of the structures. Due to their complex anisotropic structure, FRPs have been less investigated especially under realistic impact loadings. Different factors influence the ballistic performance of FRPs, namely; material properties, yarn architecture, impactor shape and velocity, far field boundary conditions and the interactions between the different lamina [135]. Several investigations were devoted to developing computational tools to simulate the composites behavior under impact loads[136-138]. Riccio and Tessitore [139] demonstrated the strong dependence of composites' behaviors on the loading conditions using nonlinear finite-element modeling. Batra and Hassan [137] adopted a continuum damage mechanics approach in their characterization of damage due to blast loading of unidirectional FRPs. Donadona et al. [138] successfully implemented and validated a 3D continuum damage mechanics finite element modeling approach for composite laminates subjected to low-velocity impact.

MAT162 is probably the most comprehensive material model ever developed (commercially) to simulate the progressive damage of FRPs. The damage modes accounted for in this material model are fiber failure due to crush, breakage and shear as well as matrix cracking and delamination. Strain rate-dependence is also accounted for in MAT162 [134]. The MAT162 was originally developed to simulate the QSSPT of thick fiberglass reinforced composites using flat cylindrical punches [140]. Thereafter, MAT162 has been used in different studies to simulate

both QSSPT [141] and impact [142] of thick fiberglass reinforced composites. However, most of the previous investigations usually borrow the GFRPs material parameters from the MAT162 developers and only calibrate few of them. In addition, due to the complicated procedures to calibrate the input material properties and the intensive required mechanical tests, MAT162 has not been employed for thin composites or composites reinforced with fibers other than fiberglass.

This chapter covers simulation of the high velocity transvers impact and perforation of FRPs utilizing an explicit 3-dimensional FEM code; LS-DYNA. Procedures to calibrate the damage softening parameters as well as the fiber crush and shear strength are also proposed and effectively implemented. As a case study, this chapter details the simulation of the mechanical behavior of a five-layers carbon fiber reinforced epoxy composite subjected to a transverse impact loading. Quasi-static mechanical tests are employed to extract various input parameters required for the composite's material model MAT162. The impact simulation results are compared to the experiments and a good correlation is observed. The sensitivity of the impact absorbed energy in light of the different parameters is discussed and some conclusions on failure modes and damage softening are drawn.

6.3 Experimental procedure

Five-layers plain weaved CFRPs of AS4 carbon fibers were fabricated following the procedures provided in in chapter 3. Tensile, compression, through thickness tension, and in-plane shear tests of the composite samples were performed. QSSPTs utilizing flat cylindrical and spherical punches were also performed on the composite coupons. The details of the experimental procedures and punch geometries are outlined in chapter 3.

In-plane shear modulus and strength were measured via double V-notched shear test (alternatively referred to as Isopescu shear test) following the ASTM D5379/D5379M-05 standards. The schematic of the test fixture and the dimensions of the sample are shown in Fig. 6.1. Since machining the samples induces edge cracks in the samples, multiple samples were sandwiched between two aluminum plates and the whole fixture was machined together to the desired shape of Fig. 6.1. To obtain the shear modulus, it is very crucial that the strain gauge covers the whole length between the two notches and, hence, the average shear strain between the two notches was measured employing a $\pm 45^\circ$ strain gages made by Micro-Measurements, Inc. (designation N2A-00-C032A-500/SP61). The strain gauges were mounted on the sample between the notches. Installation materials and procedure were implemented following the instruction provided by the manufacturer of the strain gages. The electrical resistance of each strain gage was 50 ohms and a half bridge circuit with two active gages was balanced in order to measure the difference between the strains of the two gages directly to find the shear strain.

Combined loading compression (CLC) test was performed in order to find the compressive properties of the composite samples following the ASTM D-6641 standard. Tabbed 25.4×125 mm test coupons were mounted in the fixture. Compressive load was applied on the fixture and the displacement of the upper grip of the fixture was measured via an extensometer as shown in Fig. 6.2.

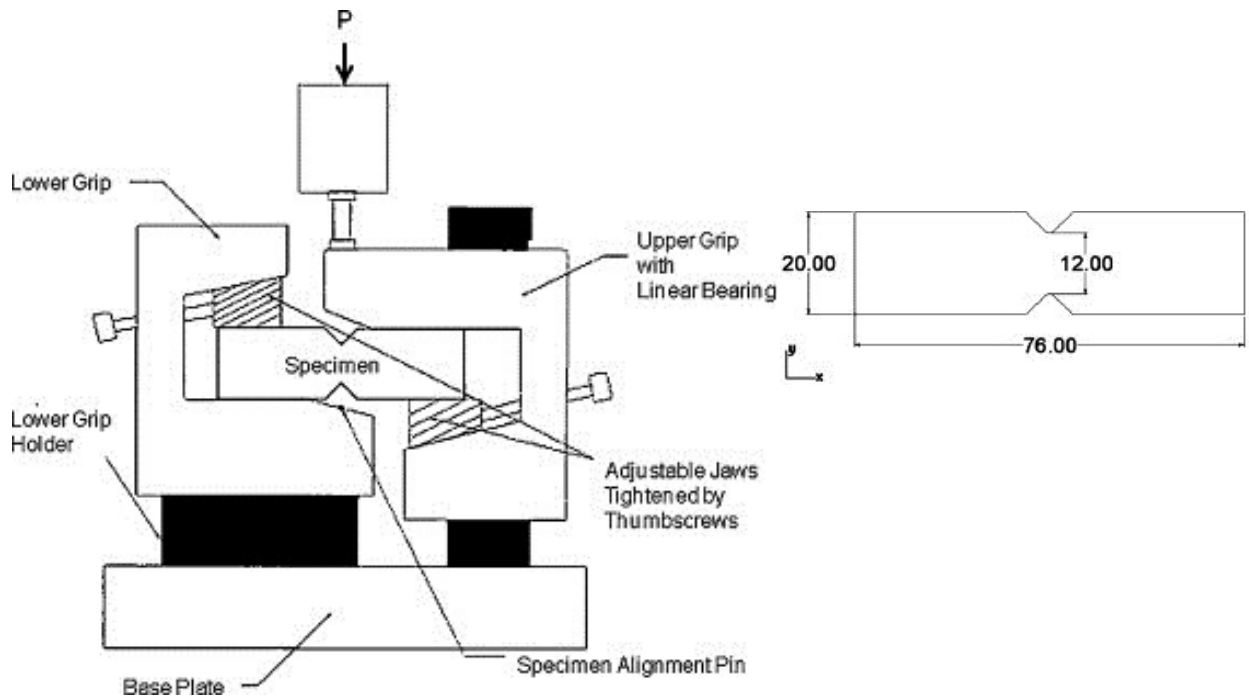


Fig. 6.1. Schematic of the test fixture [143] (left) and the sample dimensions (right) for double V-notched shear test. All dimensions are in mm.

A simple fixture was designed and manufactured for measuring the trough thickness tensile strength of the composite panels. The fixture consists of two aluminum cylinders of 32 mm diameter. The assembly of the fixture is shown in Fig. 6.3. The samples were cut using a circular drill bit and then mounted on the aluminum cylinder using the same epoxy used in the composite fabrication. The diameter of the samples was 30mm. Fig. 6.3 illustrates the circular hollow drill bit and the composite panel from which the samples were cut beside the mounted sample on the aluminum cylinder.



Fig. 6.2. Combined load compression (CLC) test fixture; to measure the displacements an extensometer was mounted on the ultra-rigid fixture.



Fig. 6.3. The Circular hollow drill bit and the cut samples (left) and the through thickness fixture and the sample mounted on one of the aluminum cylinders

All the above tests were performed utilizing an Instron 4400 testing frame and the displacements were measured using an MTS 25%-range extensometer.

6.4 FEM modeling

The model geometries were created and meshed using ANSYS LS-DYNA and pre-processed in Inventium Presys 2012 R2. MPP LS-DYNA 971 R6 explicit solver was employed for analyzing the impact, contact, and QSSPT simulations. LS-PrePost 3.1 was employed for post-processing of the binary and ASCII data files generated by the LS-DYNA.

Four different FEM models were created for the simulation purposes (see Fig. 6.4 and Fig. 6.6). Single integration point brick elements (ELFORM=1) were used for meshing of the composite plates. The impactor and punches were meshed employing rigid brick elements. The upper and lower holder parts of the QSSPT simulation were meshed using rigid shell BELYTSCHKO-TSAY elements (ELFORM=2).

Proper contact is essential for simulating the impact of laminated composites. For impact simulations LS-DYNA generally employs three contact types; namely: penalty formulation (SOFT=0), soft constraint formulation (SOFT=1) and segment-based contact (SOFT=2). The SOFT=1 type utilizes interface stiffness based on the nodal mass and the global time step size. This contact algorithm is recommended by the LS-DYNA developers for contacts where there is a wide variation in the bulk moduli of the two surfaces. Hence, the soft constraint formulation MPP formulation (varying SOFSCL=0.1-0.3) was utilized for all contact surfaces.

All the simulations presented in this chapter incorporate large deformations. To avoid the high computational cost of modeling the largely deformed elements, the concept of element's erosion

was used. In all simulations, an element was eroded when the fiber tensile failure was predicted in that element and its tensile strain was larger than 3 ($E_LIMIT = 3$). It is worth noting that when the strain in an element reaches the value of “3”, the damage model significantly degrades the element stiffness and thus the element erosion does not affect the overall response of the laminate. However, it is crucial that upon erosion of an element new contact surfaces are redefined for the remaining non-eroded elements. The `ERODING_SURFACE_TO_SURFACE` contacts were applied where erosion of the composite panel was to take place. Other surfaces with non-eroding elements were treated with the `ONE_WAY_SURFACE_TO_SURFACE` contacts.

To verify LS-DYNA’s MPP contact algorithm and choose the right element size, the Hertz’s contact between an elastic half-space and a sphere was simulated. The half-space was modeled as a large cube of $40 \times 40 \times 40 \text{ mm}^3$ and consisted of brick elements of $0.20.2 \times 0.2 \text{ mm}^3$ (see Fig. 6.4). Such brick element size is comparable with single laminate thicknesses and one fifth of the tow width. The geometric models and the boundary conditions were identical to those used in the experiments (see chapter 3 experimental section). As can be observed in Fig. 6.5, the numerical solution and the Hertz’s analytical solution are in good agreement. Therefore, the impact/punch areas were meshed using similar or smaller sized elements.

Since MAT 162 is developed to use single integration point elements, it is very critical to preserve hourglass energies in an acceptable range ($<10\%$ of the peak of internal energy in each simulation). This criterion could not be satisfied where large elements were used and thus $0.2 \times 0.2 \times 0.2 \text{ mm}^3$ or smaller sized elements were employed at critical regions.

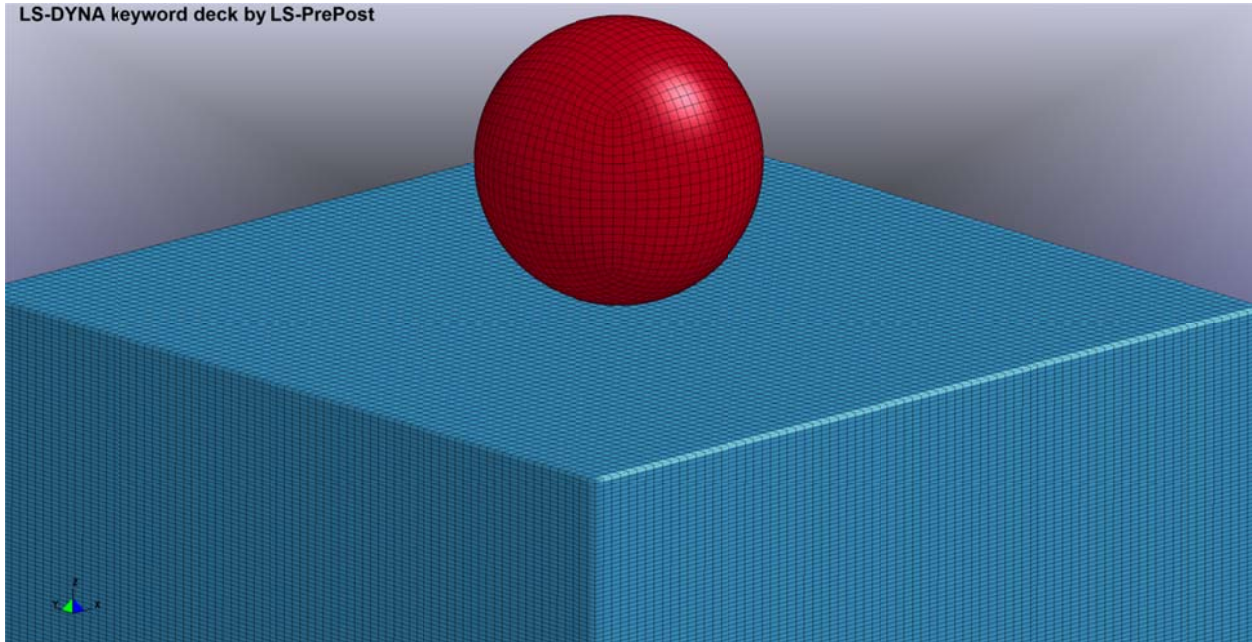


Fig. 6.4. FEM model for the Hertz contact verification problem

The FEM models for the QSSPTs and the transverse impact simulations are shown in Fig. 6.6. In order to reduce the computation time, a quarter symmetry model was used for the QSSPT simulations. The QSSPT models (Fig. 6.6-a and b) consisted of about 20,000 elements. The impact model (Fig. 6.6-c), however, retained about 200,000 elements. The top and bottom holders (only the top holders are observed in Fig. 6.6-a and b) were meshed using coarse shell elements. Equal size slave (impactor) and master (composite panel) elements usually give better contact results.

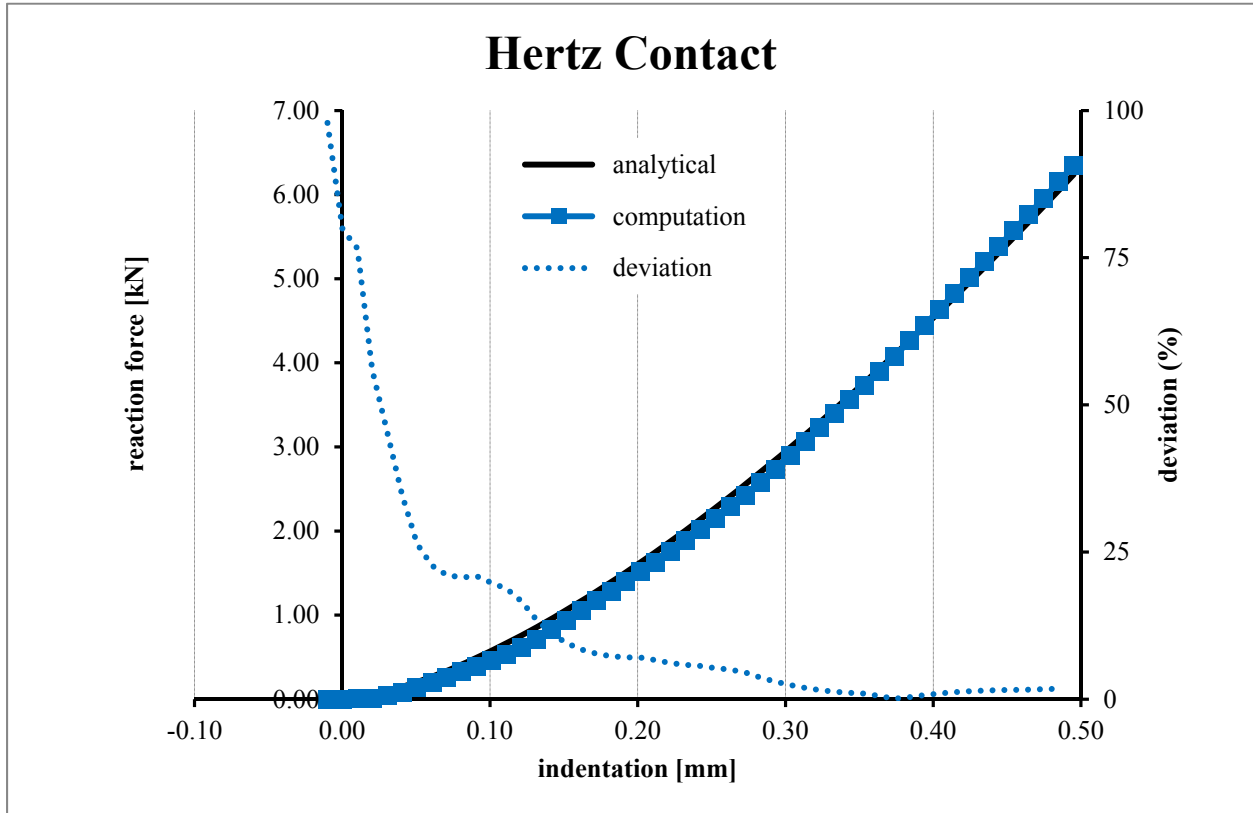


Fig. 6.5. Deviation of the numerical solution from the Hertz solution for the contact of a sphere with an elastic half-space

The indenter/impactor element sizes were very comparable to the element size of the plate at the impact/punch region. The mesh pattern and size for the holders were also identical to that of the plate. All FEM models maintained identical geometry, size and boundary conditions as the real experiments. Depending on the problem geometry and the anticipated mechanical response, adaptive meshing was used in all of the models; far from the impactor/composite contact, erosion, and at high stress gradient regions a larger mesh size was used.

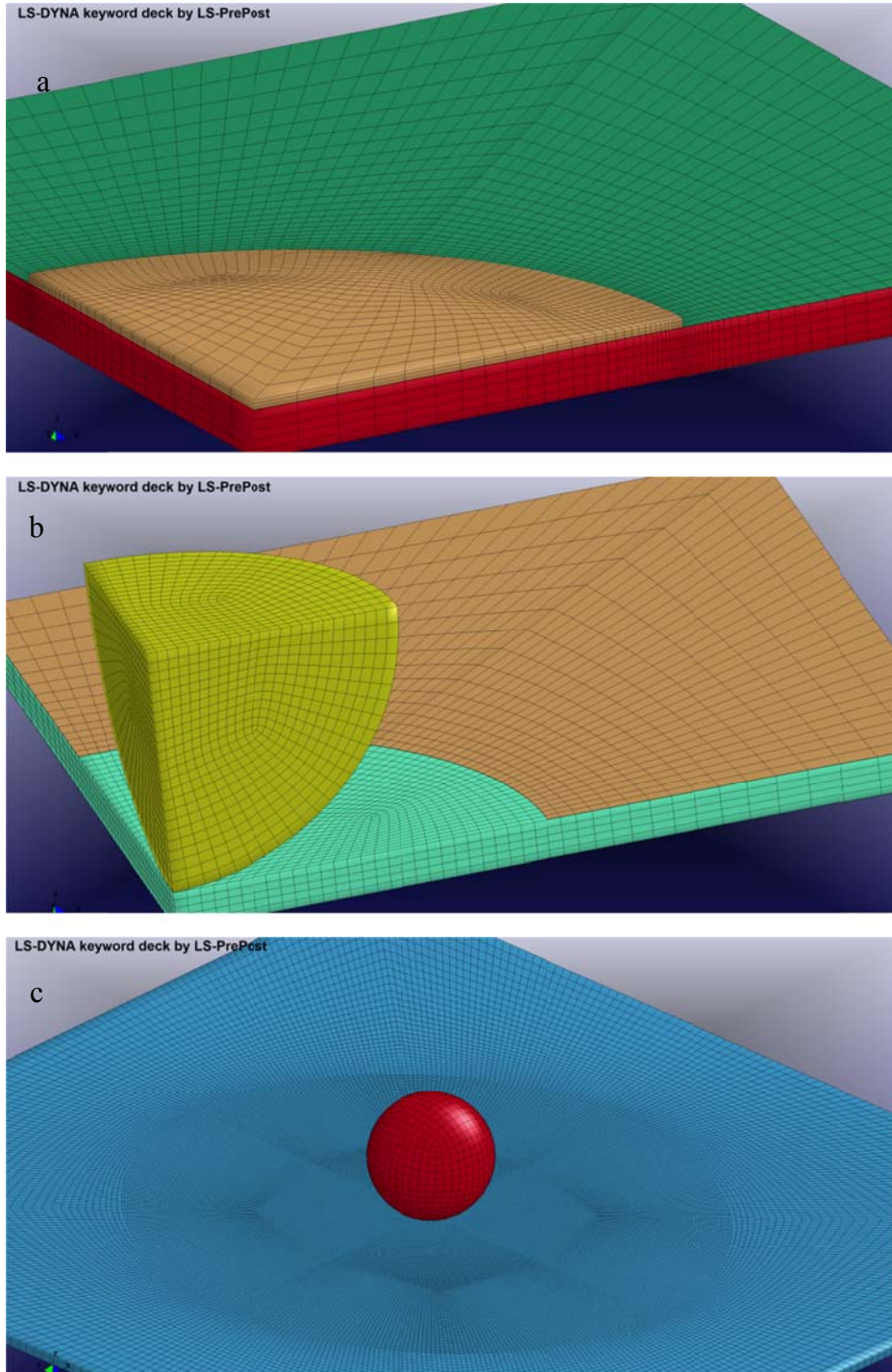


Fig. 6.6. FEM models for the a) cylindrical and b) spherical punches QSSPT and the c) transverse impact simulations

In a composite panel, the theoretical wave speed in the warp or weft directions is obtained via:

$$\bar{c} = \sqrt{\frac{E}{\rho}} \quad (6.1)$$

Where E is the composite Young's modulus in the warp or weft direction and ρ is the composite's mass density. For the finely meshed impact region (see Fig. 6.6-c) the relative difference between the numerical and theoretical wave speed was less than 5%. LS-DYNA's contact and numerical integration algorithms were checked using the Hertz contact verification simulation and wave speed comparison. However, all simulations were verified for the conservation of energy of the system. The total energy in a simulation is calculated as follows

$$Total\ Energy = IE + KE + HGE + SE + KE^{eroded} + IE^{eroded} \quad (6.2)$$

where the right hand side terms (from left to right) correspond to the internal energy, kinetic energy, hourglass energy, sliding energy, eroded kinetic energy and eroded internal energy, respectively. Very small hourglass energies (< 10% of the peak of the internal energy) and small positive sliding energies are required for a precise simulation [134]. Therefore, all the simulations were subject to verifying the hourglass energy and the total energy and the above mentioned criterion was satisfied in all cases. The energy components of the impact simulation are shown in Fig. 6.7. While the total energy remained almost constant; a very small hourglass energy is observed.

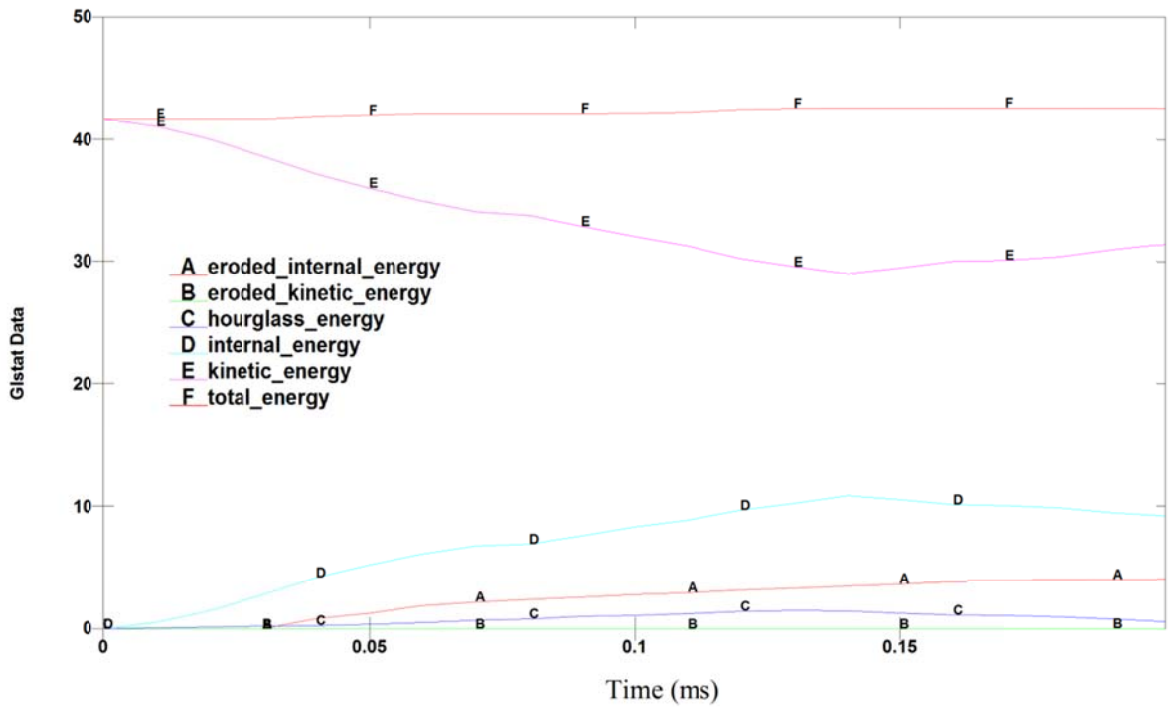


Fig. 6.7. Energy components evolution for the impact test; all energies are in joules.

While the explicit solver of LS-DYNA is very suitable for small period simulations such as impact, the quasi-static simulations are very expensive to solve with an explicit solver. The MAT162 does not support the implicit solvers of LSDYNA. However, time step sizes in the explicit scheme can be modified in quasi-static tests. The mass scaling was utilized here to increase the time step size in both spherical and flat cylindrical punch QSSPTs. An upper bound for the scaled density (i.e. mass scaling) was defined using a criterion where the longitudinal stress waves should at least travel the longest dimension of the panel by 1000 times in the time of the simulation.

6.5 MAT_COMPOSITE_MSC_DMG (MAT 162)

LS-DYNA material model 162 (*MAT_COMPOSITE_MSC*) is capable of capturing progressive damage and modeling the energy absorption in a plain weaved composite. The progressive damage model is adopted from the methodology that was first developed by Hashin [144] with a generalization to accommodate the effect of highly constrained pressures on the failure of composite. The MAT162 accounts for 5 failure modes: fiber failure under (1) tensile, (2) compression, or (3) pressure crush, (4) matrix failure and (5) delamination [134]. Material model 21 (*MAT_RIGID*) is used for the alloyed steel impactor and holders. For a plain-weave composite, MAT 162 requires 25 variables to fully capture its behavior under impact. This material model was assigned to the CFRP in all simulations. These variables were extracted from different experiments. The MAT 162 required material properties are listed in Table 6.1.

Hashin's failure criteria [142] for a unidirectional layer are generalized to capture the damage of a plain weave layer. The MAT162 material model is discussed in depth elsewhere [132, 143]. However, a brief description of the model and the different parameters involved in the model are described here for the sake of completeness. In all equations hereafter, “ r ” is the damage threshold for the corresponding damage failure.

The tension and shear fiber modes of damage for the fill and warp fiber is given by a quadratic interaction between the associated axial and through thickness shear strains

$$\left(\frac{E_a \langle \varepsilon_a \rangle}{S_{aT}}\right)^2 + \left(\frac{G_{ca} \varepsilon_{ca}}{S_{aFS}}\right)^2 - r^2 = 0 \quad (6.3)$$

Table 6.1. MAT162 input material properties for a plain weave CFRP

Density	ρ
Young's modulus	$E_a = E_b, E_c$
Shear modulus	$G_{ba}, G_{ca} = G_{cb}$
Poisson's ratio	$\nu_{ba}, \nu_{ca} = \nu_{cb}$
Tensile strength	$S_{aT} = S_{bT}, S_{cT}$
Compressive strength	$S_{aC} = S_{bC}$
Matrix shear strength	$S_{ab}, S_{bc} = S_{ca}$
Fiber shear strength	S_{FS}
Fiber crush strength	S_{FC}
Scale factor for residual compressive strength	$SFFC$
Element eroding parameters	$E_LIMT, EEXPN, ECRSH$
Scale factor for delamination criterion	S_d
Friction angle for matrix and delamination failure	ϕ
Limit damage parameter for elastic modulus reduction	$OMGMX$
Strain rate coefficient	$C_{rate1}, C_{rate2}, C_{rate3}, C_{rate4}$
Coefficient for strain softening property	$m_1=m_2, m_3, m_4$

The compressive fiber damage in the fill and warp directions is given by the maximum strain criterion. The effect of the through-thickness compressive strain and in-plane compressive damage are taken into account, as follows

$$\left(\frac{E_a \langle \varepsilon'_a \rangle}{S_{ac}}\right)^2 - r^2 = 0; \quad \varepsilon'_a = -\varepsilon_a - \langle -\varepsilon_c \rangle \frac{E_c}{E_a} \quad (6.4)$$

where S_{ac} is the axial compressive strength in the fill direction.

The high through-thickness compressive stresses generated during an impact of a layer by the projectile are taken into account using the following crush damage failure equation.

$$\left(\frac{E_c \langle -\varepsilon_c \rangle}{S_{FC}}\right)^2 - r^2 = 0 \quad (6.5)$$

While using the above equations the fiber damage can be effectively modeled, the matrix can be also damaged due to in-plane shear stresses without the occurrence of fiber damage. This damage mode is given by

$$\left(\frac{G_{ab} \varepsilon_{ab}}{S_{ab}}\right)^2 - r^2 = 0 \quad (6.6)$$

Delamination is another damage mode mainly due to matrix failure. Quadratic interaction of the transverse strains responsible for delamination of the laminate is assumed to have the following form

$$S_d^2 \left\{ \left(\frac{E_c \varepsilon_c}{S_{cT}}\right)^2 + \left(\frac{G_{bc} \varepsilon_{bc}}{S_{bc0} + S_{SRC}}\right)^2 + \left(\frac{G_{ca} \varepsilon_{ca}}{S_{ca0} + S_{SRC}}\right)^2 \right\} - r^2 = 0 \quad (6.7)$$

The onset and progression of damage are related to the stiffness losses in the material via damage variables $\bar{\omega}_i$ with $i=1, \dots, 6$. The compliance matrix is related to the damage variables according to [145]

$$[S] = \begin{bmatrix} \frac{1}{(1 - \bar{\omega}_1)E_a} & \frac{-\nu_{ba}}{E_b} & \frac{-\nu_{ca}}{E_c} & 0 & 0 & 0 \\ \frac{-\nu_{ba}}{E_a} & \frac{1}{(1 - \bar{\omega}_2)E_b} & \frac{-\nu_{cb}}{E_c} & 0 & 0 & 0 \\ \frac{-\nu_{ac}}{E_a} & \frac{-\nu_{bc}}{E_b} & \frac{1}{(1 - \bar{\omega}_3)E_c} & 0 & 0 & 0 \\ 0 & 0 & 0 & \frac{1}{(1 - \bar{\omega}_4)G_{ab}} & 0 & 0 \\ 0 & 0 & 0 & 0 & \frac{1}{(1 - \bar{\omega}_5)G_{bc}} & 0 \\ 0 & 0 & 0 & 0 & 0 & \frac{1}{(1 - \bar{\omega}_6)G_{ca}} \end{bmatrix} \quad (6.8)$$

The damage variables are calculated from the damage thresholds obtained via Eqs. (6.3)-(6.7) as follows

$$\bar{\omega}_i = 1 - \exp\left(\frac{1}{m_j}(1 - r_j^{m_j})\right) ; \quad r_j \geq 1 \quad (6.9)$$

The damage thresholds have an initial value of zero resulting in a zero value for the associated damage variable $\bar{\omega}$. After the damage is initiated and the damage threshold reaches a value of equal to or greater than unity, the corresponding moduli are reduced according to (6.8) and (6.9).

The MAT162 incorporates the effects of strain-rate on the strength and moduli by a logarithmic strain-dependent function in the form

$$\{E_{RT}\} = \{E_0\} \left(1 + \{C_{rate}\} \ln \frac{\{\dot{\epsilon}\}}{\dot{\epsilon}_0}\right) \text{ and } \{S_{RT}\} = \{S_0\} \left(1 + \{C_{rate}\} \ln \frac{\{\dot{\epsilon}\}}{\dot{\epsilon}_0}\right), \quad (6.10)$$

Where the “0” subscripted parameters correspond to the initial values of the parameter. The moduli, strain rate, and rate parameter tensors are given by Eq. (6.10). Other parameters are defined as

$$\{S\} = \begin{Bmatrix} S_{aT} \\ S_{aC} \\ S_{bT} \\ S_{bC} \\ S_{FC} \\ S_{FS} \end{Bmatrix}, \{E_{RT}\} = \begin{Bmatrix} E_a \\ E_b \\ E_c \\ G_{ab} \\ G_{bc} \\ G_{ca} \end{Bmatrix}, \{C_{rate}\} = \begin{Bmatrix} C_{rate2} \\ C_{rate2} \\ C_{rate4} \\ C_{rate3} \\ C_{rate3} \\ C_{rate3} \end{Bmatrix}, \{\dot{\epsilon}\} = \begin{Bmatrix} |\dot{\epsilon}_a| \\ |\dot{\epsilon}_b| \\ |\dot{\epsilon}_c| \\ |\dot{\epsilon}_{ab}| \\ |\dot{\epsilon}_{bc}| \\ |\dot{\epsilon}_{ca}| \end{Bmatrix} \quad (6.11)$$

The rate effects on both axial moduli are controlled by the parameter C_{rate2} , the through thickness modulus by C_{rate4} and the shear moduli by C_{rate3} .

6.6 Results and discussion

All the input parameters excluding the four damage parameters (m_1, \dots, m_4), fiber shear strength (S_{FS}), and fiber crush strength (S_{FC}) were either directly determined from the tensile, shear and compression tests or estimated. The outcome of the two QSSPTs and impact simulations were found to be somewhat insensitive to few of the MAT162 input parameters such as the scale factor for residual compressive strength (S_{FFC}), the scale factor for delamination criterion (S_d) and the friction angle for matrix and delamination failure (ϕ).

The calibration of the damage parameters and the shear and crush fiber strengths were performed by tuning the input parameters (m_1, \dots, m_4 , S_{SF} , and S_{FC}) and comparing of the simulation results (the QSSPTs) with the experiments to find the optimum values of the input parameters which

will lead to a minimal error between the experiment and the model. The peak load of the flat punch QSSPT and the load-displacement curve of the spherical punch QSSPT were optimized utilizing this trial and error approach. Table 6.2 summarizes the numerical and experimental values of the peak loads for the two QSSPTs. Considering the very complex nature of the simulations, the error values are satisfactory and the simulations are in good agreement with the experiments.

Table 6.2. The experimental and numerical peak loads of the QSSPTs and their corresponding errors

		Peak Load (KN)
Flat cylinder punch	Experiment	12.46
	FEM	11.72
	% error	6%
Hemispherical punch	Experiment	4.32
	FEM	4.27
	% error	1%

The damage modes and progression in the spherical punch-QSSPT are speculated to be similar to those for the impact test. The boundaries of the samples in the spherical punch-QSSPT are tightly clamped while the punch perforates the composite plate. In resemblance, the transverse impact only affects the area that is adjacent to the impactor striking region and the plate does not have enough time to elastically deform after it is hit with the impactor. Hence, both of these tests can be considered similar as they only act on a very local area while the surrounding plate does not move or interact. The load-displacement experimental curves for the spherical punch-QSSPT along with the FEM simulation results are plotted in Fig. 6.8. The good agreement between the

experiment and simulation reveals that the Mat162 is capable of both capturing the maximum loads and the linear and nonlinear behaviors of the composite under the test. The deviation of the simulation from the experiment after 0.45 mm displacement arises from the zero coefficients of friction that are used in the simulation. The frictional interaction of the punch with the broken fibers exerts an extra vertical force on the punch.

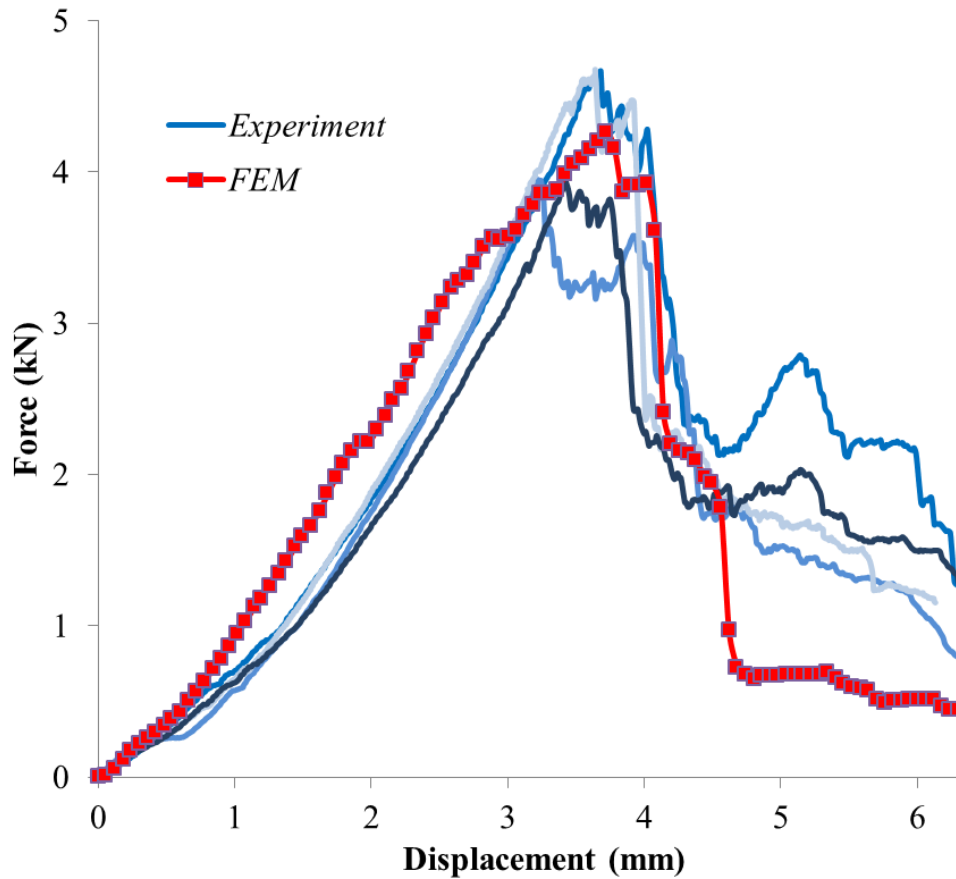


Fig. 6.8. Four representative QSSPT load-displacement curves and the FEM simulation results

The input parameters obtained from the QSSP simulations and the other quasi-static mechanical tests are tabulated in Table 6.3. The strain rate parameters were set to zero. Using these parameters the impact simulation was run and the absorbed impact energy for the simulated

impact was calculated. The absorbed energy for the experiment and simulation were found to be 11.1 and 14.4 joules, respectively. While a 30% error is present, the overestimation of the absorbed energy can be alleviated if appropriate strain-rate parameters are supplied to the simulation. Moreover, the failure modes of the composite after the impact simulation were identical to the perforated composites in the actual experiment.

Table 6.3. Employed input values for MAT162

<i>Parameter</i>	value	<i>Parameter</i>	value
P (kg/m^3)	1500	S_{FC} (MPa)	900
$E_a = E_b, E_c$ (GPa)	62.4,10	$SFFC$	0.3
$G_{ba}, G_{ca} = G_{cb}$ (GPa)	7, 5	$E_LIMIT, EEXPN, ECRSH$	3.0,3.0,0.3
$\nu_{ba}, \nu_{ca} = \nu_{cb}$	0.1,0.18	S_d	1.1
$S_{aT} = S_{bT}, S_{cT}$ (MPa)	824,50	ϕ	10
$S_{aC} = S_{bC}$ (MPa)	250	$OMGMX$	0.999
$S_{ab}, S_{bc} = S_{ca}$ (MPa)	80,60	$C_{rate1}, C_{rate2}, C_{rate3}, C_{rate4}$	0.0,0.0,0.0,0.0
S_{FS} (MPa)	120	$m_1 = m_2, m_3, m_4$	0.13,0.35,0.3

The sensitivity of the simulation results to different parameters was also examined. Among the two QSSPTs and impact simulations, the results of some simulations were found to be more sensitive to certain parameters than others. For example, the QSSPT using the flat cylindrical punch was almost insensitive to the changes in the strain softening property for fiber damage in fill and warp directions (m_1 and m_2). The absorbed impact energy is somewhat insensitive to m_4 values between 0.1 and 0.5 and S_{FS} values between 0.4 and 1.2 GPa. Interestingly, the peak load for the spherical-punch QSSPT was found to be inversely proportional to the S_{FS} over the 0.8-1.2

GPa range. While other relations between the behavior of the simulations and different input parameters could be derived, they are problem-specific. Moreover, the effects of input parameters on the simulation results were found to be highly nonlinear and interdependent on each other.

6.7 Conclusions

The capability of the MAT162 material model of LS-DYNA FEM software to simulate the QSSPT and impact of a thin CFRP was demonstrated in this chapter. A systematic approach was proposed and implemented to calibrate the input parameters of MAT162. While this material model has been generally employed to simulate thick fiberglass reinforced composites, it was able to capture the damage softening behavior and different failure modes of spherical punch QSSPT of the thin CFRP. However, the impact simulations, based on the calibrated parameters of the MAT162, overestimated the energy absorption of the CFRP subjected to a transverse impact. The MAT162 provided valuable information on different failure modes, damage initiation and sensitivity of the composite behavior to different mechanical properties. The proposed methodology to calibrate MAT162 parameters facilitates the use of this model for simulations utilizing different fiber reinforcements and composite thicknesses.

Chapter 7. Electromagnetic Interference (EMI) Shielding of Hybrid Fiberglass Reinforced Composites

7.1 Overview

Electromagnetic (EM) waves, such as electronic noise and radio-frequency interference can be regarded as an invisible electronic pollution which justifies a very active quest for effective electromagnetic interference (EMI) shielding materials. Highly conductive materials of adequate thickness and excellent electrical properties are the primary solutions to shield against EMI. Equipment cases and the basic structure of space aircraft and launch vehicles have traditionally been made of aluminum, steel and other electrically conductive metals. However, in recent years composite materials have been used for electronic equipment manufacturing because of their lightweight, high strength, and ease of fabrication. Despite these benefits, composite materials are not as electrically conductive as traditional metals, especially in terms of electrical grounding purposes and shielding. Therefore, extra effort must be taken to resolve these shortcomings. This chapter demonstrates a study on developing hybrid composites based on fiberglass with surface grown carbon nanotubes (CNTs) for EMI applications. The choice of fiberglass (rather than carbon fibers) is primarily because it naturally possesses poor electrical and thermal conductivities; hence, the use of GSD to grow CNTs over the glass fiber surface can significantly improve these conductivities. The fabrics were sputter-coated with a thin layer of SiO₂ thermal barrier prior to growing of the CNTs. The CNTs were grown on the surface of woven fiberglass fabrics utilizing GSD following the protocols outlined in chapter 4. Reference fabrics based on raw fiberglass fabric, SiO₂ coated fabric, and SiO₂ coated fabric which underwent the identical

heat treatment as the samples with CNTs were also prepared. Two -layers composite specimens based on different surface treated fiberglass fabrics were fabricated and their EMI shielding effectiveness (SE) were measured. The EMI SE of the hybrid CNT-fiberglass composites was shown to be 5-10 times of the reference samples. However, the tensile mechanical properties of the composites based on the different above mentioned fibers revealed significant degradation due to the elevated CNT growth temperature and the addition of coating layer and CNTs. To further probe the structure of the hybrid composites and the interconnectivity of the CNTs from one interface to another, sets of 20-layers composites based on different surface treated fabrics were also fabricated.

7.2 Introduction

The very fast development and proliferation of gigahertz electronic systems and telecommunication devices is responsible for the steadily increasing EMI pollution. In this regard, a large range of applications is concerned from commercial and scientific electronic instruments to antenna systems, communication instruments, and military electronic devices. In modern automobiles, the ever-increasing number of onboard electronics and microprocessor-controlled systems requires that all electronic sub-assemblies (ESA) in the vehicle meet stringent electromagnetic compatibility (EMC) requirements. Airbags, cruise controls, anti-lock braking systems, and other electronically controlled assemblies can be adversely affected by EMI and the vehicle operation can be critically compromised. Today, safety and reliability requirements mandate that all automotive onboard electronics must not emit EMI signals, and must be immune to external EMI signals. Magnetic shielding is often employed in hospitals, where devices, such as magnetic resonance imaging (MRI) equipment, generate powerful magnetic flux. Magnetic

shielding rooms are constructed to prevent this equipment from interfering with surrounding instruments or meters.

Shielding prevents coupling of undesired radiated electromagnetic energy into equipment otherwise susceptible to it. In an aircraft, for example, structural shielding effectiveness can range from 20 to 100 dB [146] which is not sufficient to protect antenna from undesired signals generated within the aircraft. Other difficult shielding situations involve equipment of extremely high sensitivity. Among these are the radio astronomy, GPS systems, missile guidance, and tracking systems for satellites and space systems.

7.2.1 EMI shielding theory

The shielding effect exerted by a uniform conductive sheet, is denoted as the synthesis of three kinds of losses, i.e., absorption, reflection, and multiple reflection losses. Generally the sum of these three terms is referred to as the SE normally expressed in dB. The analytical calculation of shielding effectiveness pertinent to a practical shielding configuration is invariably difficult [147]. The shielding depends on many factors such as; the electric properties and the thickness of the shielding material used, the type of field intensity, the frequency of the EM wave, the distance between the source and the receptors and the nature of discontinuities (if any) in the shield. The total shielding effectiveness can be described as

$$SE = A + R + M \quad (7.1)$$

Where A is the absorption loss (dB), or the attenuation due to transmission into a conductive sheet; R is the reflection loss (dB) between air and the conductive sheet surface; and M is the multiple reflection loss (dB) due to repeated reflection on both surfaces of the conductive sheet

as shown in Fig. 7.1. Absorption relies on the interaction between electric and/or magnetic dipoles with the electromagnetic radiation. A is calculated using specific electrical conductivity σ_r , and specific permeability μ_r as follows

$$A = 8.686 t_n \sqrt{\pi f \mu_r \sigma_r} \quad (7.2)$$

Where t_n is the thickness of the conductive sheet and f is the frequency (Hz). A is thus proportional to $\sqrt{\sigma_r \mu_r}$. Copper is usually considered as a reference material with σ_r and μ_r set equal to unity.

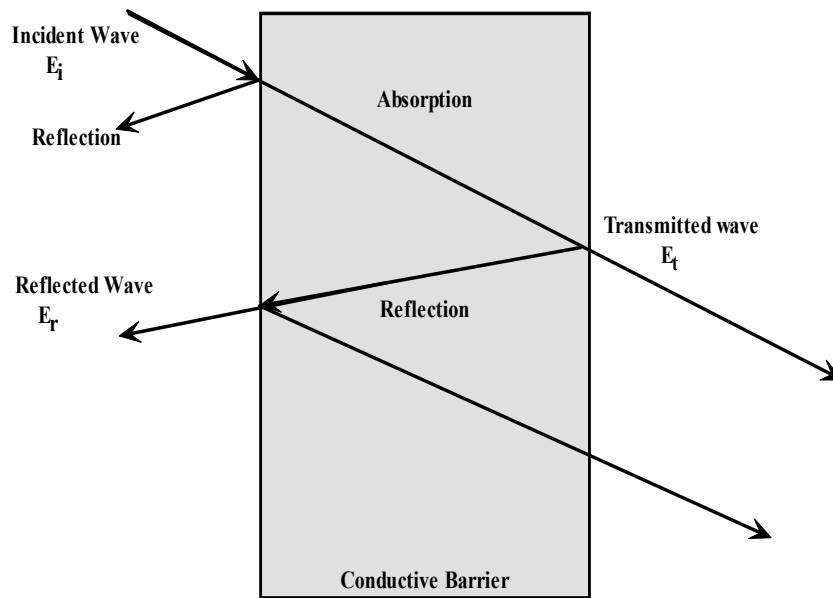


Fig. 7.1. Path of electromagnetic wave through a conductive shielding barrier

Shielding is usually dominated by reflection which relies on the interaction between mobile charge carriers in the shield material interacting with the electromagnetic fields in the radiation

[148, 149]. The reflection loss, R , is denoted using the parameter k , which is a ratio of the intrinsic impedance for a metallic body, Z_s , to that of specific impedance, Z_w

$$R = 20 \log \frac{(1+k)^2}{4k} = 20 \log \frac{(Z_w + Z_s)^2}{4Z_w Z_s} \quad (7.3)$$

As shown above, the reflection loss varies with the space impedance. Thus, its value differs between a near field and a far field. For instance, in a far field (in the case of plane wave), the reflection loss R is denoted by:

$$R = 108.2 - 10 \log \frac{f}{10^6} + 20 \log \sqrt{\sigma_r / \mu_r} \quad (7.4)$$

Thus, R is proportional to $\log \sqrt{\sigma_r / \mu_r}$. Even in a near field, a reflection loss can be denoted by a similar equation. For this reason, specific reflection loss, $k \sqrt{\sigma_r / \mu_r}$, is considered to be an index of the magnitude of the shielding effect with the specific reflection loss for copper being taken as unity, as was done for the specific absorption loss. The multiple reflection loss, M in dB, is calculated as follows

$$M = 20 \log \left[1 - \frac{(1-k)^2}{(1+k)^2} \right] \exp(-2t \sqrt{\pi \mu f \sigma}) \quad (7.5)$$

The multiple reflection loss value can be neglected when a thick conductive sheet is used or when a high frequency is applied, because its value becomes much smaller than that of the absorption loss. As the frequency of the incident electromagnetic radiation increases, reflection decreases and absorption increases. The absorption loss is proportional to the thickness of the

shield. Multiple reflections occur at several reflecting surfaces is the shield. A common example of this would be in a non-conducting material with a conducting filler [148].

7.2.2 *Materials for EMI shielding*

The EMI shielding materials should possess good electrical conductivity to minimize the penetration of waves into the material and low magnetic permeability to convert magnetic energy into heat. High conducting metals such as steel, copper, aluminum are well suited for many EMI shielding equipment [150]. The use of metals for EMI shielding has the disadvantages of limited physical flexibility, heavy weight, corrosion and difficulty of tuning the shielding efficiency.

With the substantial progress in preparation and processing methods, highly conductive polymers have become important materials to substitute metal cases. Intrinsically conducting polymers such as polyaniline (PAN) and polypyrrole (PPY) display, as some of their foremost properties, a high conductivity (σ) and dielectric constant (ϵ_r) combined with a very light weight, flexibility, corrosion resistance, and reasonably facile processability [151]. Due to these properties and their high conductance, they have recently evinced much interest in potential application such as EMI shielding screens, coatings or jackets for flexible conductors, and broadband microwave absorbers [152]. However, it is difficult to achieve an extremely high level of shielding efficiency by using conducting polymers only. Alternatively, the synthesis of conducting polymer-metal complexes has been proposed [153-155]. To enhance the shielding effectiveness with even lighter filler materials, carbon based materials were investigated as fillers for polymers used in EMI. For carbon based fillers such as graphite, carbon fibers, and carbon nanotubes (CNTs), EMI shielding effectiveness increases as a function of fill factor and filler aspect ratio [156]. Das et al., [157] evaluated the shielding effectiveness of carbon black and carbon fiber-

filled conductive rubber. They concluded that short carbon fiber-filled composites are more effective due to their fibrous nature than particulate-filled composites in providing higher EMI shielding from electromagnetic interference. In another study by Luo and Chung [156], carbon-matrix composite with continuous carbon-fibers (7 micrometers in diameter) was found to be an excellent EMI shielding material with shielding effectiveness of 124 dB, low surface impedance and high reflectivity in the frequency range from 0.3 MHz to 1.5 GHz. However, currently used composites require high filler to polymer ratio, which deteriorates the overall mechanical properties through deterioration of intrinsic matrix morphology [158]. A possible route to ameliorate the above problems, through using low filler volume fractions, is to incorporate carbon nanotubes (CNTs) in the composites.

CNTs are particularly fit for EMI shielding applications due to their extremely high aspect ratio, which increases EMI shielding effectiveness by increasing connectivity. Because a higher fill factor generally weakens a composite, CNTs can make structurally stronger shields by allowing for a low fill factor to achieve effective shielding. CNTs themselves also have excellent structural properties which can contribute to high structural strength EMI shields. EMI shielding is a promising application for carbon nanotubes (CNTs) and their composites. Kim et al. [159] synthesized composite films of multiwall carbon nanotubes (MWCNTs) and poly (methylmethacrylate) (PMMA) for electromagnetic interference shielding material. The electrical conductivity of the composite was improved by increasing the mass fraction of MWCNTs, yielding an increase in the shielding effectiveness (SE). The authors concluded that the highest SE of MWCNTs-PMMA composite is 27 dB. This level of shielding indicates commercial use for far field electromagnetic shielding. Li et al [160] fabricated single wall

carbon nanotubes (SWCNTs)/epoxy composite that contains 15% wt SWCNTs. EMI SE was tested in the frequency range of 10 MHz to 1.5 GHz, and was found to be 49 dB at 10 MHz and exhibiting 15-20 dB in the 500 MHz to 1.5 GHz ranges, respectively. Recently, Lee et al., [161, 162], concluded that the decrease of the shielding effectiveness of CNTs filled composite was due to the decrease of the nanotube aspect ratio. Li et al., [160] concluded that SWCNTs polymer composites with higher SWCNTs aspect ratio and better nanotube wall integrities enhances the EMI performance significantly. Carbon nanotubes with high aspect ratio have advantages in both electrical conductivity and specific surface area, so their shielding effectiveness is superior to general carbon fibers and carbon black. It was reported that the carbon nanofibers with coiled or helical conformation were effective fillers for EMI shielding and could absorb about 99% of the electromagnetic waves of GHz order [163].

Fiberglass is a particularly an effective material for use in structural composites (e.x. marine structures) because of its light weight, excellent physical properties and low cost (compared to carbon fibers) [164, 165]. Since fiberglass is not a good electrical conductor, it is not suitable for EMI shielding, but with the addition of CNTs a fiberglass composite can effectively shield EMI while retaining its structural properties.

There are several routes to incorporate CNTs into a fiberglass composite. In the conventional method, the CNTs are mixed in with the epoxy prior to curing using one of the many techniques which have been utilized in recent years [166]. This method of incorporating CNTs is typically the cheaper and more scalable route but it has several disadvantages. One of the most important problems with this approach is that increasing CNT content leads to agglomeration of CNTs in the bulk of the composite [72]. Another important problem with this method is that the CNTs

can be filtered during the FRP fabrication process, leading to non-homogenous matrix microstructure [167]. Alignment and dispersion are critical factors that are difficult to control experimentally using oft-repeated mixing methods. CNTs embedded in a polymeric matrix form aggregates of themselves that are not only poorly adhered to the matrix, but also concentrate stresses, compromising the effect of the CNTs as reinforcement. The uniformity of dispersion degrades as the aspect ratio, in particular as the length of CNTs, increases [160].

Alternatively, identical to what was proposed for the carbon fibers (chapters 4 and 5), to eliminate the dispersion problem, CNTs can be controlled-grown on the surface of the fiberglass. This chapter probes the EMI shielding effectiveness and electrical conductivity of an epoxy composite reinforced by woven fiberglass fabrics with CNTs grown radially from their surface. To better understand the behavior of the hybrid CNT-fiberglass composite electrical conductivity measurements in-plane and through thickness were performed.

7.3 Experimental methods

Fiberglass plain weave fabrics with an average diameter of 7 microns were obtained from BFG industries Inc. The CNT growth conditions were similar to those described in chapter 4, except for an extended growth time of two hr and a 4 nm thick layer of catalyst nickel film. For the purpose of EMI SE and electrical conductivity tests 2-layered and 20-layered composites were fabricated, respectively. The fabrication process and the epoxy matrix are identical to that described earlier in chapter 3. The samples were based on as is fabric (referred to as RAW henceforth), SiO₂ and Ni coated fabric that was exposed to the elevated CNT growth condition (HT), the SiO₂ and Ni coated fabric with surface grown CNTs (GSD). The fiber volume fractions for the 2 and 20 layered fiberglass composites were around 65% and 60%, respectively.

The thin 2-layered composites possessed an average thickness of 0.45 mm. The thick 20-layered composites that were employed for electrical conductivity measurements were diced into different sizes. To measure the through thickness resistance, $1 \times 1 \times 3$, $4 \times 4 \times 3$ mm³ and $10 \times 10 \times 3$ mm³ samples from different locations were diced. Narrow strips of $30 \times 3 \times 3$ mm³ were cut for in-plane measurements.

To contrast the effect of the surface modification (i.e. sputter-coating, heat treatment and growing CNTs) on the tensile mechanical properties, four 2-layered composites based on raw (Raw), SiO₂ and Ni sputtered (Sp), sputtered and heat treated (Sp+HT), and surface grown CNTs (GSD) fabrics were fabricated. The tensile coupon preparation and testing conditions were similar to that described in chapter 3.

The EMI SE was measured using a set-up consisting of an R&S®ZVA Vector Network Analyzer, two coaxial to waveguide adapters, and two waveguides. The sample was positioned between the waveguides and clamped down using four screws connecting the edges of the waveguides. The waveguides were calibrated for both the amplitude and phase before the actual measurements. The shielding was calculated from the ratio of the amplitudes of the transmitted wave to the incident one according to

$$SE = 20 \log \left[\frac{S_t}{S_i} \right] \quad (7.6)$$

where S_t and S_i are the amplitudes of the transmitted and incident EM waves, respectively.

The in-plane and through thickness electrical conductivities of the GFRPs were measured using a Keithley 4200 semiconductor characterization system. To eliminate the contact resistance effect,

the measurements were repeated for different length samples and the resistance values were measured by curve fitting to the resistance-length curves. Gold coated fibers with surface grown CNTs were investigated using a 5200 Hitachi scanning electron microscopy (SEM) unit operated at 5 KeV.

7.4 Results and discussion

The 2 hr CNT growth time (via GSD) with the use of the 4 nm nickel layer as the catalyst ensured deposition of a dense and long forests of CNTs over the fiberglass. As shown in Fig. 7.2 a uniform layer of radially grown CNTs covers the fiberglass. It is very crucial that the CNTs touch one another and form a continuous electron pathway to create an electrically conductive layer. The high magnification micrograph in Fig. 7.2 shows that the CNTs were both curled and bent, hence touching other CNTs.

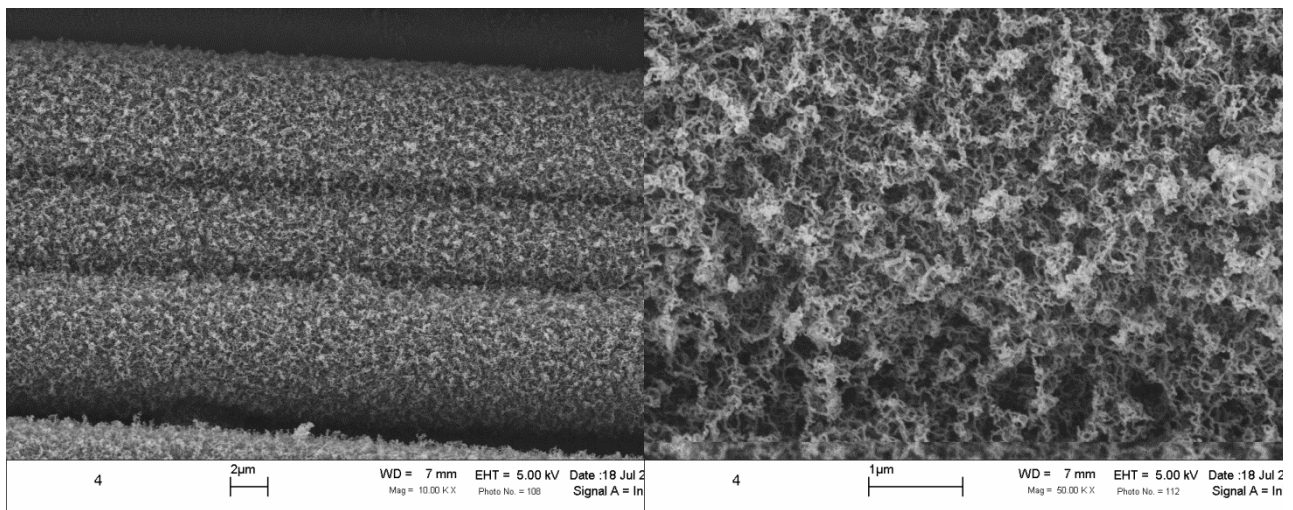


Fig. 7.2. The uniform aerial cover of the CNTs over the fiberglass at different magnifications

The EMI SEs for different samples are plotted in Fig. 7.3. The fiberglass and epoxy matrix were insulating and the SiO₂ and nickel layers did not affect the electrical properties of the composite. However, the surface grown CNTs resulted in an average SE increase of almost 1 dB over the measured frequency range compared to the other samples. Since the dB unit is in logarithmic scale, an order of magnitude increase in the EMI attenuation was observed. The insulator fiberglass layers sandwiching the CNTs do not contribute to the SE and the whole shielding effect emanates from the 2-3 microns long dense CNT layers on the surface of the fabrics.

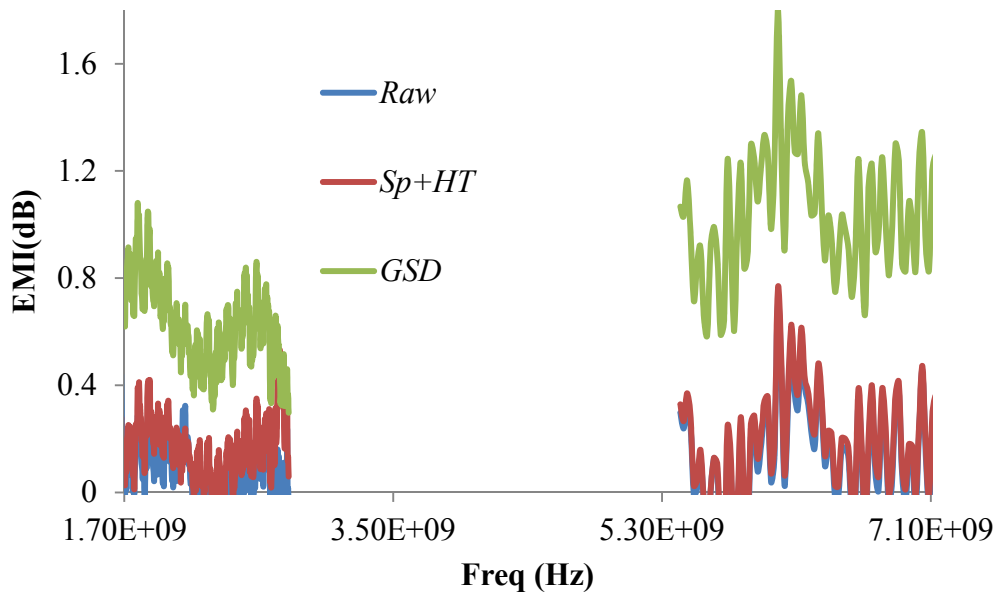


Fig. 7.3. EMI SE for different composite specimens

While both the electrical conductivity and the magnetic permeability contribute to the EMI SE, it is crucial to understand the effect of surface grown CNTs on the electrical properties of the composites along different directions. The hybrid composite retains a sandwiched structure of the fiberglass lamina and surface grown CNTs. To better understand electrical response of these sandwiched hybrid composites the 20-layered samples were tested for in-plane and through -

thickness electrical resistivity. The epoxy and fiberglass components of the composites are very insulating and usually possess resistance values too high ($\gg 10 \text{ G}\Omega$) to measure with even sensitive measurement devices [168]. As shown in Fig. 7.4 and Fig. 7.5, the electrical resistivity of the hybrid GRP composite with GSD surface grown CNTs was measured for different length samples in both the in-plane and through thickness directions. These samples attained $43 \text{ k}\Omega\cdot\text{cm}$ and $5.3 \text{ M}\Omega\cdot\text{cm}$ resistivity in the in-plane and through thickness directions, respectively. This behavior was expected since the CNTs form an electron pathway by touching one another in the in-plane direction. However, the grown CNTs are separated by the insulator fiberglass and epoxy lamina in the through thickness direction. Thus, it is less likely that a conducting pathway forms in this direction.

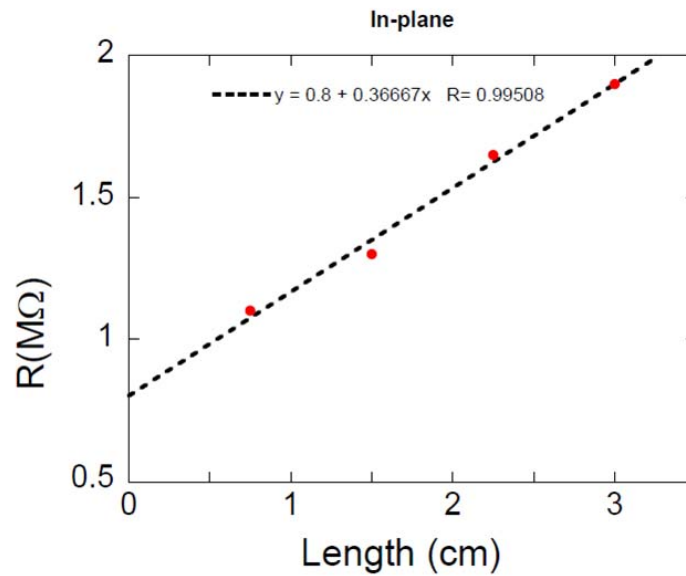


Fig. 7.4. In-plane electrical resistance versus the specimen length for the hybrid GRP-CNT composites

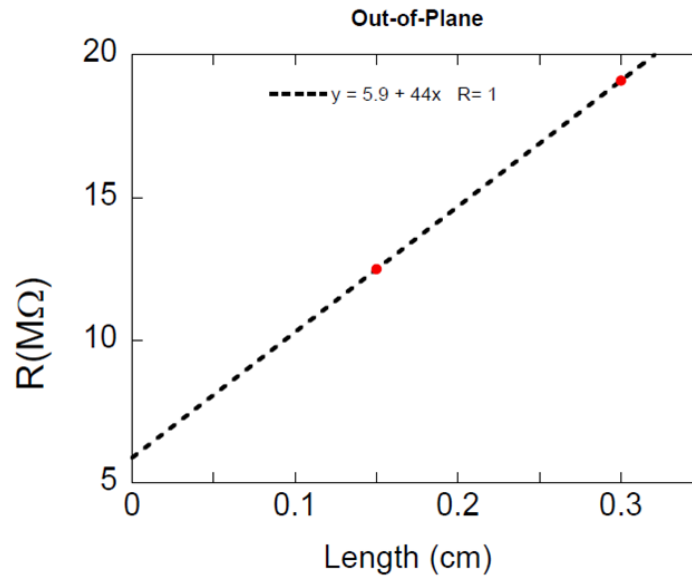


Fig. 7.5. Through thickness resistance versus the specimen length for the hybrid GRP-CNT composites

The tensile properties of the 2-layered fiberglass composite samples of different fiber surface treatments are plotted in Fig. 7.6. Similar to the carbon fiber reinforced composites the stiffness of the samples is dominated by the core of the reinforcing fibers (i.e. fiberglass here). The Young's moduli of all samples are identical, however, the strain to failure and ultimate strength of specimens based on modified fibers dropped compared to the reference configuration based on as is fibers. The thin sputtered layer of SiO₂ and Ni (overall ~80 nm thick) weakened the adhesion between the fibers and the epoxy matrix causing a sharp drop in both strength and strain to failure. Further decreasing of the interfacial bonding occurred as a result of exposure to elevated temperatures. Finally, while long grown CNTs are required to ensure a connected network (to increase the electrical conductivity), they resulted in further decline in both the strength and strain to failure. It is speculated that the high viscosity polymer matrix (950 cps)

does not impregnate the dense and long CNTs. Either short or dense or long and less compacted CNTs would increase the interfacial bonding between the fibers and matrix.

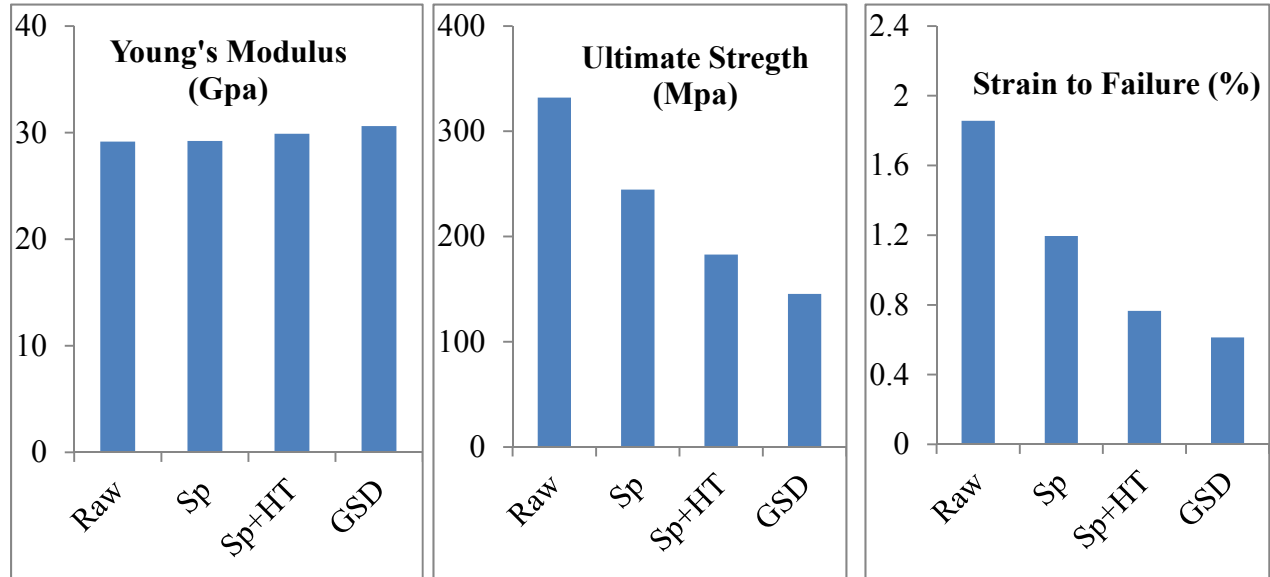


Fig. 7.6. Tensile mechanical properties of the samples based on raw (Raw), SiO₂ and Ni sputtered (Sp), SiO₂ and Ni sputtered and heat treated (Sp+HT), and surface grown CNTs (GSD) fabrics.

7.5 Conclusions

Fiberglass is known to be very vulnerable to high temperatures. Although, an inert atmosphere was used and the temperature was kept relatively low (i.e. 550 °C), the strength and the strain to failure of the composites significantly declined compared to the composites based on raw fiberglass. The two aforementioned properties are highly influence by the quality of the fiber surface and its adhesion to the matrix. However, the unaffected stiffness of the specimens revealed that there is no degradation to the fiber core. The surface grown CNTs utilizing GSD method increased both in-plane and through thickness electrical conductivity of the composite.

The in-plane resistivity was two orders of magnitude lower than the through thickness resistivity indicating a poor network percolation in the out-of-plane direction. Consequently, the EMI attenuation of the samples with surface grown CNTs was increased by an order of magnitude over the measured frequency range. While this work demonstrates the potential of the CNTs to enhance electrical properties of fiber reinforced composites, further optimization of the growth procedure is required to obtain electrically conductive composites with improved mechanical properties.

Chapter 8. Conclusions and Future Work

The effects of integrating CNTs into FRPs, mainly, on the mechanical performance of the corresponding hybrid were investigated in this dissertation. First, a conventional route, referred to as the mixing route, entails adding MWCNTs to the polymer phase of the composite via ultrasonic and shear mixing, was investigated. Instrumented indentation confirmed moderate improvements in stiffness, hardness, and viscoelastic performance of the MWCNT-epoxy system over the neat epoxy reference sample under different thermo-mechanical environments. In addition, utilizing the nanoimpact test, the nanocomposites based on CNTs, were assessed for the impact energy absorption and they exhibited superior properties compared to the reference neat epoxy samples.

A three-phase CFRP with a CNT enriched epoxy matrix was investigated in the next step for tensile, damping, and impact properties. Compared to the reference CFRP samples, the hybrid CFRPs comprising CNT enriched epoxy matrix showed minor improvements in the tensile properties. However, the damping performance and the impact energy absorption of the CFRP-CNTs hybrid composite improved by 26% and 21%, respectively. These enhancements were achieved at a minimal weight increase entailed by adding 2 wt% MWCNTs to the polymer matrix.

As an alternative to mixing the CNTs with the epoxy, a relatively low temperature synthesis technique; graphitic structures by design (GSD), was developed and proven to be capable of grafting high volume fractions of un-agglomerated CNTs (this cannot be achieved via the mixing

route) on carbon fibers. The quality and morphology of the CNTs deposited using these techniques were probed via different microscopy characterization techniques. The importance of the low temperature of the GSD to prevent fiber damage was later demonstrated through tensile mechanical tests. This novel method offers an opportunity to place CNTs in advantageous areas of the composite (e.g., at ply interface) where conventional fiber architectures are inadequate. Carbon fiber reinforced composites based on different surface-treated fibers, using different steps of the GSD technique, were investigated for tensile, damping, and impact properties and showed significant improvements compared to the reference CFRPs. For example, a 56% improvement in the damping and 70% enhancement in the impact energy absorption were observed.

While the work outlined in this dissertation embodies valuable information on the different hybrid composites systems, the primary novel contribution of this study is the development of the GSD and revealing its ability to significantly improve the damping and the impact resistance performance of the hybrid CFRP with surface grown CNTs via the GSD technique. The GSD weight penalty is far less than that of the mixing techniques where the CNTs account for less than 0.05% wt% of the composites.

In a complimentary study, the effect of surface grown CNTs on the electrical conductivity of a fiberglass reinforced composite and subsequently its EMI SE was investigated. Moderate improvements in both electrical conductivity and EMI shielding effectiveness of the hybrid GFRP were revealed.

Accordingly, GSD showed great promise for improving mechanical performance of the CFRPs and also for imparting extra functionalities, imposed by the unique properties of the CNTs, to the

conventional CFRPs. With the emergence of the CFRPs in aircrafts and airplanes, it is crucial to understand their behavior under ballistic impact phenomenon. Employing an advanced material model of the finite element code LS-DYNA, the impact behavior of a thin CFRP was simulated. This material model showed great potential for modeling of different composite systems including hybrid composites.

To fully benefit from the significant aptitude of the GSD grown CNTs, further optimization of this technique in terms of the CNTs growth length, deposition density and pattern as well as optimizing the thermal barrier coating material and thickness is required. The FEM simulation can be applied to the hybrid CFRPs to understand the CNT toughening and stiffening mechanisms. In addition, numerical optimization codes can be linked to the LS-DYNA output to more systematically calibrate the MAT162 parameters.

List of publications from the dissertation

Under review

1. **M. Tehrani**, M. Safdari, A. Y. Boroujeni, Z. Razavi, S.W. Case, K. Dahmen, H. Garmestani and M. Al-Haik, "Use of Surface Grown Carbon Nanotubes in Woven Carbon Fiber Reinforced Epoxy Composites for Structural Damping," *Nanotechnology*.

2. **M. Tehrani**, A. Y. Boroujeni, T. B. Hartman, T. P. Haugh, S. W. Case and M. S. Al-Haik, "Mechanical characterization and impact damage assessment of a woven carbon fiber reinforced carbon nanotube-epoxy composite," *Composites Science and Technology*.

Published

3. **M. Tehrani**, M. Safdari, M. Al-Haik, "Nanocharacterization of Creep Behavior of Multi Wall Carbon Nanotubes /Epoxy Nanocomposites," *International Journal of Plasticity*, 27(6): 887-901 (2011).

4. C. Luhrs, D. Garcia, **M. Tehrani**, M Al-Haik, M. Reda Taha and J. Phillips, "Generation of Carbon Nanofilaments on Carbon Fibers at 550oC," *Carbon*, 47: 3071-3078 (2009).

5. **M. Tehrani**, A. Y. Boroujeni, T. P. Haugh, T. B. Hartman, S. W. Case, M. S. Al-Haik, "Impact and Quasi-Static Mechanical Properties of a Carbon Fiber Reinforced Carbon Nanotube/Epoxy", IMECE2012-86396, ASME 2012 International Mechanical Engineering Congress & Exposition.

6. **M. Tehrani**, M.S. Al-Haik, Nanocharacterization of creep response of multiwall carbon, preprint, IUPAC, Blacksburg, 2012.

7. **M. Tehrani**, M. Safdari, S. Case and Marwan S. Al-Haik, "Using Multiscale Carbon Fiber / Carbon Nanotubes Composites for Damping Applications", CD Proceedings of ASME Conference on Smart Materials, Adaptive Structures and Intelligent Systems, Scottsdale, AZ, September 18-21, 2011.

References

- [1] Hyer MW. Stress analysis of fiber-reinforced composite materials: McGraw-Hill companies, Inc.; 1997.
- [2] Ronald F G. A review of recent research on mechanics of multifunctional composite materials and structures. *Composite Structures*. 2010;92(12):2793-810.
- [3] Qian H, Greenhalgh ES, Shaffer MSP, Bismarck A. Carbon nanotube-based hierarchical composites: a review. *Journal of Materials Chemistry*. 2010;20(23):4751-62.
- [4] Madhukar MS, Drzal LT. Fiber-Matrix Adhesion and Its Effect on Composite Mechanical-Properties .4. Mode-I and Mode-II Fracture-Toughness of Graphite Epoxy Composites. *Journal of Composite Materials*. 1992;26(7):936-68.
- [5] Chandra R, Singh SP, Gupta K. Damping studies in fiber-reinforced composites - a review. *Composite Structures*. 1999;46(1):41-51.
- [6] Iijima S. Helical Microtubules of Graphitic Carbon. *Nature*. 1991;354(6348):56-8.
- [7] Sinnott SB, Andrews R. Carbon nanotubes: Synthesis, properties, and applications *Critical Reviews in Solid State and Mat Science*. 2001;26(3):145-249.
- [8] Dresselhaus MS, Dresselhaus G, Charlier JC, Hernandez E. Electronic, thermal and mechanical properties of carbon nanotubes. *Philosophical Transactions of the Royal Society a-Mathematical Physical and Engineering Sciences*. 2004;362(1823):2065-98.
- [9] Baughman RH, Zakhidov AA, de Heer WA. Carbon nanotubes - the route toward applications. *Science*. 2002;297(5582):787-92.
- [10] Thostenson ET, Chou T-W. Aligned multi-walled carbon nanotube-reinforced composites: processing and mechanical characterization. *Journal of Physics D: Applied Physics*. 2002;35(16):L77.
- [11] Allaoui A, Bai S, Cheng HM, Bai JB. Mechanical and electrical properties of a MWNT/epoxy composite. *Composites Science and Technology*. 2002;62(15):1993-8.
- [12] Li YL, Kinloch IA, Windle AH. Direct spinning of carbon nanotube fibers from chemical vapor deposition synthesis. *Science*. 2004;304(5668):276-8.
- [13] Garmestani H, Al-Haik MS, Dahmen K, Tannenbaum R, Li DS, Sablin SS, et al. Polymer-mediated alignment of carbon nanotubes under high magnetic fields. *Advanced Materials*. 2003;15(22):1918-21.
- [14] Zeineldin R, Al-Haik M, Hudson LG. Role of Polyethylene Glycol Integrity in Specific Receptor Targeting of Carbon Nanotubes to Cancer Cells. *Nano Letters*. 2009;9(2):751-7.

- [15] Soliman, E., Al-Haik, M., Reda Taha, M.M. “On and off-axis tension behaviour of fiber reinforced polymer (FRP) composites incorporating multi-walled carbon nanotubes”, *Journal of Composite Materials*, In press, 2012 .
- [16] García EJ, Hart AJ, Wardl BL. Electrical and Thermal Properties of Hybrid Woven Composites Reinforced with Aligned Carbon Nanotubes. *AIAA Journal*. 2008;46(6):1405-12.
- [17] Otsuka K, Abe Y, Kanai N, Kobayashi Y, Takenaka S, Tanabe E. Synthesis of carbon nanotubes on Ni/carbon-fiber catalysts under mild conditions. *Carbon*. 2004;42(4):727-36.
- [18] Zhu S, Su C-H, Lehoczyk SL, Muntele I, Ila D. Carbon nanotube growth on carbon fibers. *Diamond and Related Materials*. 2003;12(10-11):1825-8.
- [19] Luhrs CC, Garcia D, Tehrani M, Al-Haik M, Taha MR, Phillips J. Generation of carbon nanofilaments on carbon fibers at 550 degrees C. *Carbon*. 2009;47(13):3071-8.
- [20] Al-Haik M, Luhrs CC, Reda Taha MM, Roy AK, Dai L, Phillips J, et al. Hybrid Carbon Fibers/Carbon Nanotubes Structures for Next Generation Polymeric Composites. *Journal of Nanotechnology*. 2010;2010.
- [21] Boskovic BO, Golovko VB, Cantoro M, al e. Low temperature synthesis of carbon nanofibres on carbon fibre matrices. *Carbon*. 2005;43 2643-8.
- [22] Chen X, Saito T, Kusunoki M, Motojima S. Three dimensional vapor growth mechanism of carbon microcoils. *J Mater Res*. 1999;14(11):4329 -36.
- [23] Garcia E, Wardle BL, deVillori RG, Wicks S, Ishiguro K, Yamamoto N, et al. Aligned Carbon Nanotube Reinforcement of Advanced Composite Ply Interfaces. 49th AIAA/ASME/ASCE/AHS/ASC Structures, Structural Dynamics, and Materials Conference Schaumburg, IL.
- [24] Phillips J, Luhrs C, Leseman ZC, Al-Haik M. Novel Graphitic Structures by Design. *Proceedings of ASME International Mechanical Engineering Congress and Exposition IMECE07*. Seattle, Washington, USA.
- [25] Zhang Q, Liu J, Sager R, Dai L, Baur J. Hierarchical composites of carbon nanotubes on carbon fiber: Influence of growth condition on fiber tensile properties. *Composites Science and Technology*. 2009;69: 594–601.
- [26] Westwood ME, Webster JD, Day RJ, Hayes FH, Taylor R. Oxidation protection for carbon fibre composites. *Journal of Materials Science*. 1996;31(6):1389-97.
- [27] Askari D, Ghasemi-Nejhad MN. Inter-laminar mechanical properties improvements in carbon nanotubes reinforced laminated nanocomposites. *Proceedings of the ASME 2011 International Mechanical Engineering Congress & Exposition*; p. IMECE2011-64283.

- [28] Wicks SS, de Villoria RG, Wardle BL. Interlaminar and intralaminar reinforcement of composite laminates with aligned carbon nanotubes. *Composites Science and Technology*. 2010;70(1):20-8.
- [29] Phillips J, Shiina T, Nemer M, Lester K. Graphitic Structures by Design. *Langmuir*. 2006;22(23):9694-703.
- [30] Veedu VP, Cao AY, Li XS, Ma KG, Soldano C, Kar S, et al. Multifunctional composites using reinforced laminae with carbon-nanotube forests. *Nature Materials*. 2006;5(6):457-62.
- [31] Li WH, Chen XH, Chen CS, Xu LS, Yang Z, Wang YG. Preparation and Shear properties of carbon nanotubes/poly (butyl methacrylate) hybrid material. *Polymer Composites*. 2008;29(9):972-7.
- [32] Selmi A, Friebel C, Doghri I, Hassis H. Prediction of the elastic properties of single walled carbon nanotubes reinforced polymers. *Composites Science and Technology*. 2007;67(10):2071-84.
- [33] Kao CC, Young RJ. Assessment of Interface Damage during the deformation of carbon nanotubes composites. *Journal of Materials Science*. 2010;45(6):1425-31.
- [34] Li CY, Wei TW. Multiscale modeling of compressive behaviour of carbon nanotube polymer composites. *Composites Science and Technology*. 2006;66(14):2409-14.
- [35] Bower C, Rosen R, Han J, Zhou O. Deformation of carbon nanotubes in nanotube polymer composite. *Applied Physics Letters*. 1999;74(22):3317-9.
- [36] Giraldo LF, Lopez BL, Bostow W. Effect of the type of carbon nanotubes on tribological properties of polyamide 6. *Polymer Engineering and Science*. 2009;49(5):896-902.
- [37] Wang C, Xue T, Dong B, Wang Z, Li HL. Polystyrene-acrylonitrile CNTs nanocomposites preparation and tribological behavior research. *Wear*. 2008;265(11-12):1923-6.
- [38] Sun LY, Gibson RF, Gordaninejad F, Suher J. Energy absorption capability of nanocomposites: A review. *Composites Science and Technology*. 2009;69(14):2392-409.
- [39] Shaffer MS, Windle AH. Fabrication and characterization of carbon nanotube/poly(vinyl alcohol) composite. *Advanced Materials*. 1999;11:937-41.
- [40] Gong X, Liu J, Baskaran S, Voise R, Young JS. Surfactant assisted processing of carbon nanotubes/polymer composites. *Chem mater*. 2000;12:1049-52.
- [41] Zhou X, Wang KW, Bakis CE. SPIE Intl Symp Smart Structures and Materials: damping Isolation Conference. San Deigo, CA; p. 18.
- [42] Suhr J, Koratkar NA, Koblinski P, Ajayan P. Viscoelasticity in carbon nanotube composites. *Nature Materials*. 2005;4(2):134-7.

- [43] Zhang W, Joshi A, Wang Z, Kane RS, Koratkar N. Creep mitigation in composites using carbon nanotubes additives. *Nanotechnology*. 2007;18.
- [44] Plaseied A, Fatemi A. Tensile creep and eformation modeling of vinyl ester polymer and its nanocomposites. *Journal of Reinforced Plastics and Composites*. 2009;28(14):1775-88.
- [45] Findley WN, Lai JS, Onaran K. Creep and relaxation of nonlinear viscoelastic materials: with an Introduction to Linear Viscoelasticity: Dover Publication; 1989.
- [46] Li K, Gao XL, Roy AK. Micromechanical modeling of Viscoelastic Properties of carbon nanotube reinforced polymer composites. *Mechanics of Advanced Materials and Structures*. 2006;13:317-28.
- [47] Tehrani M, Safdari M, Al-Haik MS. Nanocharacterization of creep behavior of multiwall carbon nanotubes/epoxy nanocomposite. *International Journal of Plasticity*. 2011;27(6):887-901.
- [48] Kalcioglu ZI, Qu M, Strawhecker KE, Shazly T, Edelman E, VanLandingham MR, et al. Dynamic impact indentation of hydrated biological tissues and tissue surrogate gels. *Philosophical Magazine*. 2011;91(7-9):1339-55.
- [49] Beake BD, Goodes SR, Smith JF, Gao F. Nanoscale repetitive impact testing of polymer films. *J Mater Res*. 2004;19(1):237-47.
- [50] Fischer-Cripps AC. *Nanoindentation*
New York: Springer-Verlag. ; 2002.
- [51] Paiva MC, Zhou B, Fernando KAS, Lin Y, Kennedy JM, Sun YP. Mechanical and morphological characterization of polymer-carbon nanocomposites from functionalized carbon nanotubes. *Carbon*. 2004;42(14):2849-54.
- [52] Dutta AK, Penumadu D, Files B. Nanoindentation testing for evaluating modulus and hardness of single-walled carbon nanotube-reinforced epoxy composites. *Journal of Materials Research*. 2004;19(1):158-64.
- [53] Oliver WC, Pharr GM. An improved technique for determining hardness and elastic modulus using load and displacement sensing indentation experiments. *J Mater Res*. 1992; 7:1564-83.
- [54] Chudoba T, Richter F. Investigation of creep behaviour under load during indentation experiments and its influence on hardness and modulus results. *Surface and Coatings Technology*. 2001;148:191-8.
- [55] Ting TCT. The contact stresses between a rigid indenter and a viscoelastic half-space. *J Appl Mech*. 1966;88:845.
- [56] Tweedie CA, Vlieta KJV. Contact creep compliance of viscoelastic materials via nanoindentation. *J Mater Res*. 2006;21(6).

- [57] VanLandingham MR, Chang N-K, Drzal PL, White CC, Chang S-H. Viscoelastic Characterization of Polymers Using Instrumented Indentation. I. Quasi-Static Testing. *Journal of Polymer Science Part B: Polymer Physics*. 2005;43:1794–811.
- [58] Lu H, Wang B, Ma J, Huang G, Viswanathan H. Measurement of Creep Compliance of Solid Polymers by Nanoindentation. *Mechanics of Time-Dependent Materials* 2003;7:189-207.
- [59] Yang S, Zhang Y-W, Zeng K. Analysis of nanoindentation creep for polymeric materials. *J Appl Phys*. 2004;95:3655.
- [60] Juliano TF, VanLandingham MR, Tweedie CA, Van Vliet KJ. Multiscale creep compliance of epoxy networks at elevated temperatures. *Exp Mech*. 2007;47(1):99-105.
- [61] Beake BD, Smith JF. Nano-impact testing-an effective tool for assessing the resistance of advanced wear-resistant coatings to fatigue failure and delamination. *Surf Coat Technol*. 2004;188:594-8.
- [62] Al-Haik MS, Garmestani H, Savran A. Explicit and Implicit Viscoplastic Models for Polymeric Composite. *International Journal of Plasticity*. 2004;20:1875-907.
- [63] Al-Haik MS, Hussaini MY, Garmestani H. Prediction of nonlinear viscoelastic behavior of polymeric composites using an artificial neural network. *International Journal of Plasticity*. 2006;22(7):1367-92.
- [64] Smith JFZ, S. High temperature nanoscale mechanical property measurements *Surface Engineering*. 2000;143-146.
- [65] Beake BDaS, James F. High-temperature nanoindentation testing of fused silica and other materials *Philosophical Magazine A*, 82:10, . *Philosophical Magazine* 2002;82:2179 — 86.
- [66] Camponeschi E, Vance R, Al-Haik M, Garmestani H, Tannenbaum R. Properties of carbon nanotube–polymer composites aligned in a magnetic field. *Carbon*. 2007;45:2037-46.
- [67] Gray A, Orecchia D, Beake BD. Nanoindentation of advanced polymers under non-ambient conditions: Creep modelling and tan Delta. *Journal of Nanoscience and Nanotechnology*. 2009;9(7):4514-9.
- [68] Al-Haik MS, Garmestani H, Li DS, Hussaini MY, Sablin SS, Tannenbaum R, et al. Mechanical Properties of Magnetically Oriented Epoxy. *Journal of Polymer Science Part B: Polymer Physics*. 2004;42:1586-600.
- [69] Yang J, Zhang Z, Friedrich K, Schlarb AK. Creep Resistant Polymer Nanocomposites Reinforced with Multiwalled Carbon Nanotubes. *Macromolar Rapid Communications*. 2007;28:955-61.

- [70] GanB M, Satapathy BK, Thunga M, Weidisch R, Potschke P, Janke A. Temperature Dependence of Creep Behavior of PP-MWNT Nanocomposites. *Macromolecular Rapid Communication*. 2007;28:1624-33.
- [71] Trabelsi W, Michel L, Othomene R. Effects of Stitching on Delamination of Satin Weave Carbon-Epoxy Laminates Under Mode I, Mode II and Mixed-Mode I/II Loadings. *Applied Composite Materials*. 2010;17(6):575-95.
- [72] Khan SU, J-K K. Impact and Delamination Failure of Multiscale Carbon Nanotube-Fiber Reinforced Polymer Composites: A Review. *International Journal of Aeronautical and Space Sciences*. 2011;12(2):115-33.
- [73] Gu BH, Li YL. Ballistic perforation of conically cylindrical steel projectile into three-dimensional braided composites. *Aiaa J*. 2005;43(2):426-34.
- [74] Chung DDL. Structural composite materials tailored for damping. *Journal of Alloys and Compounds*. 2003;355(1-2):216-23.
- [75] Aksoy A, Carlsson LA. INTERLAMINAR SHEAR FRACTURE OF INTERLEAVED GRAPHITE EPOXY COMPOSITES. *Composites Science and Technology*. 1992;43(1):55-69.
- [76] Vlasveld DPN, Bersee HEN, Picken SJ. Nanocomposite matrix for increased fibre composite strength. *Polymer*. 2005;46(23):10269-78.
- [77] Hudnut SW, Chung DDL. Use of submicron diameter carbon filaments for reinforcement between continuous carbon-fiber layers in a polymer-matrix composite. *Carbon*. 1995;33(11):1627-31.
- [78] Joshi SC, Dikshit V. Enhancing interlaminar fracture characteristics of woven CFRP prepreg composites through CNT dispersion. *Journal of Composite Materials*. 2012;46(6):665-75.
- [79] An Q, Rider AN, Thostenson ET. Electrophoretic deposition of carbon nanotubes onto carbon-fiber fabric for production of carbon/epoxy composites with improved mechanical properties. *Carbon*. 2012;50(11):4130-43.
- [80] Warriar A, Godara A, Rochez O, Mezzo L, Luizi F, Gorbatiikh L, et al. The effect of adding carbon nanotubes to glass/epoxy composites in the fibre sizing and/or the matrix. *Composites Part a-Applied Science and Manufacturing*. 2010;41(4):532-8.
- [81] Solirnan EM, Sheyka MP, Taha MR. Low-velocity impact of thin woven carbon fabric composites incorporating multi-walled carbon nanotubes. *International Journal of Impact Engineering*. 2012;47:39-47.
- [82] Inam F, Wong DY, Kuwata M, Peijs T. Multiscale Hybrid Micro-Nanocomposites Based on Carbon Nanotubes and Carbon Fibers. *Journal of Nanomaterials*. 2010.

- [83] Kostopoulos V, Baltopoulos A, Karapappas P, Vavouliotis A, Paipetis A. Impact and after-impact properties of carbon fibre reinforced composites enhanced with multi-wall carbon nanotubes. *Composites Science and Technology*. 2010;70(4):553-63.
- [84] Safdari M, Al-Haik MS. Optimization of stress wave propagation in a multilayered elastic/viscoelastic hybrid composite based on carbon fibers/carbon nanotubes. *Polymer Composites*. 2012;33(2):196-206.
- [85] Grujicic M, Bell WC, Biggers SB, Koudela KL, Tarter JF, Cheeseman BA. The effect of a carbon-nanotube forest-mat strike face on the ballistic-protection performance of E-glass reinforced poly-vinyl-ester-epoxy composite armour. *Proceedings of the Institution of Mechanical Engineers Part L-Journal of Materials-Design and Applications*. 2008;222(L1):15-27.
- [86] Grujicic M, Bell WC, Thompson LL, Koudela KL, Cheeseman BA. Ballistic-protection performance of carbon-nanotube-doped poly-vinyl-ester-epoxy matrix composite armor reinforced with E-glass fiber mats. *Materials Science and Engineering a-Structural Materials Properties Microstructure and Processing*. 2008;479(1-2):10-22.
- [87] Ajayan PM, Suhr J, Koratkar N. Utilizing interfaces in carbon nanotube reinforced polymer composites for structural damping. *Journal of Materials Science*. 2006;41(23):7824-9.
- [88] Koratkar NA, Suhr J, Joshi A, Kane RS, Schadler LS, Ajayan PM, et al. Characterizing energy dissipation in single-walled carbon nanotube polycarbonate composites. *Applied Physics Letters*. 2005;87(6):063102.
- [89] Venkatanarayanan PS, Stanley AJ. Intermediate velocity bullet impact response of laminated glass fiber reinforced hybrid (HEP) resin carbon nano composite. *Aerosp Sci Technol* 2011; doi: 10.1016/j.ast.2011.05.007.
- [90] Khan SU, Li CY, Siddiqui NA, Kim J-K. Vibration damping characteristics of carbon fiber-reinforced composites containing multi-walled carbon nanotubes. *Composites Science and Technology*. 2011;71(12):1486-94.
- [91] Suhr J, Koratkar N. Energy dissipation in carbon nanotube composites: a review. *Journal of Materials Science*. 2008;43(13):4370-82.
- [92] Sun CT, Potti SV. A simple model to predict residual velocities of thick composite laminates subjected to high velocity impact. *International Journal of Impact Engineering*. 1996;18(3):339-53.
- [93] Potti SV, Sun CT. Prediction of impact induced penetration and delamination in thick composite laminates. *International Journal of Impact Engineering*. 1997;19(1):31-48.
- [94] Jen0 ST, Jing HS, Chung C. PREDICTING THE BALLISTIC LIMIT FOR PLAIN WOVEN GLASS EPOXY COMPOSITE LAMINATE. *International Journal of Impact Engineering*. 1994;15(4):451-64.

- [95] Abrate S. *Impact on Composite Structures*. Cambridge, UK: Cambridge University Press.; 1998.
- [96] Lopresto V, Melito V, Leone C, Caprino G. Effect of stitches on the impact behaviour of graphite/epoxy composites. *Composites Science and Technology*. 2006;66:206-14.
- [97] Bibo GA, Hogg PJ. Review: the role of reinforcement architecture on impact damage mechanisms and post-impact compression behavior. *J Mater Sci*. 1996;31(1115-1137).
- [98] Hartman TB, Allen DW, Case SW. Failure of Spectra Shield UHMWPE Composite Due to Low Velocity Hard Body Impact. *SAMPE*. 2010.
- [99] Taha MMR, Shrive NG. Enhancing fracture toughness of high-performance carbon fiber cement composites. *Aci Materials Journal*. 2001;98(2):168-78.
- [100] SF Z, E M, OR Y. Indirect estimation of fiber/polymer bond strength and interfacial friction from maximum load values recorded in the microbond and pull-out tests. Part 1: local bond strength. *J of Adhesion Sc & Tech*. 2002;16:1171-200.
- [101] Li D, Zhang XF, Sui G, Wu DH, Liang J, Yi XS. Toughness improvement of epoxy by incorporating carbon nanotubes into the resin. *Journal of Materials Science Letters*. 2003;22(11):791-3.
- [102] Xia Z, Curtin WA, Sheldon BW. Fracture toughness of highly ordered carbon nanotube/alumina nanocomposites. *Journal of Engineering Materials and Technology-Transactions of the Asme*. 2004;126(3):238-44.
- [103] Gojny FH, Wichmann MHG, Kopke U, Fiedler B, Schulte K. Carbon nanotube-reinforced epoxy-compo sites: enhanced stiffness and fracture toughness at low nanotube content. *Composites Science and Technology*. 2004;64(15):2363-71.
- [104] Xia Z, Riester L, Curtin WA, Li H, Sheldon BW, Liang J, et al. Direct observation of toughening mechanisms in carbon nanotube ceramic matrix composites. *Acta Materialia*. 2004;52(4):931-44.
- [105] Makris TD, Giorgi R, Lisi N, Pilloni L, Salernitano E, De Riccardis MF, et al. Carbon nanotube growth on PAN- and pitch-based carbon fibres by HFCVD. *Fullerenes Nanotubes and Carbon Nanostructures*. 2005;13:383-92.
- [106] Qu L, Zhao Y, Dai L. Carbon microfibers sheathed with aligned carbon nanotubes: Towards multidimensional, multicomponent, and multifunctional nanomaterials. *Small*. 2006;2(8-9):1052-9.
- [107] Phillips J, Leseman ZC, Cordaro J, Luhrs CC, Al-Haik M. Graphitic structures by design. Paper. No. IMECE2007-42977. *Proceedings of 2007 ASME International Mechanical Engineering Congress and Exposition, WA Seattle (USA) 2007*.

- [108] Downs WB, Baker RTK. MODIFICATION OF THE SURFACE-PROPERTIES OF CARBON-FIBERS VIA THE CATALYTIC GROWTH OF CARBON NANOFIBERS. *Journal of Materials Research*. 1995;10(3):625-33.
- [109] Downs WB, Baker RTK. NOVEL CARBON FIBER-CARBON FILAMENT STRUCTURES. *Carbon*. 1991;29(8):1173-9.
- [110] Feih S, Mouritz AP. Tensile properties of carbon fibres and carbon fibre-polymer composites in fire. *Composites Part a-Applied Science and Manufacturing*. 2012;43(5):765-72.
- [111] Dupuis A. The catalyst in the CCVD of carbon nanotubes—a review. *Progress in Materials Science*. 2005;50(8):929-61.
- [112] Keszler AM, Nemes L, Ahmad SR, Fang X. Characterisation of carbon nanotube materials by Raman spectroscopy and microscopy— a case study of multiwalled and singlewalled samples. *Journal of Optoelectronics and Advanced Materials*. 2004;6(4):1269 - 74.
- [113] Fitzer E. PAN-based carbon fibers-present state and trend of the technology from the viewpoint of possibilities and limits to influence and to control the fiber properties by the process parameters. *Carbon*. 1989; 27(5):621 -45.
- [114] Jorio A, Pimenta MA, Filho AGS, Saito R, Dresselhaus G, Dresselhaus MS. Characterizing carbon nanotube samples with resonance Raman scattering. *New Journal of Physics*. 2003;5(1):139.
- [115] Melo JDD, Radford DW. Time and temperature dependence of the viscoelastic properties of CFRP by dynamic mechanical analysis. *Composite Structures*. 2005;70(2):240-53.
- [116] Crema LB, Castellani A, Drago U. Damping characteristics of fabric and laminated kevlar composites. *Composites*. 1989;20(6):593-6.
- [117] Saravanos DA, Chamis CC. Unified micromechanics of damping for unidirectional and off-axis fiber composites. *Journal of Composites Technology & Research*. 1990;12(1):31-40.
- [118] Kaliske M, Rothert H. Damping characterization of unidirectional fiber-reinforced polymer composites. *Composites Engineering*. 1995;5(5):551-67.
- [119] Chandra R, Singh SP, Gupta K. Micromechanical damping models for fiber-reinforced composites: a comparative study. *Composites Part a-Applied Science and Manufacturing*. 2002;33(6):787-96.
- [120] Han SJ, Chung DDL. Mechanical energy dissipation using carbon fiber polymer-matrix structural composites with filler incorporation. *Journal of Materials Science*. 2012;47(5):2434-53.
- [121] Ci L, Suhr J, Pushparaj V, Zhang X, Ajayan PM. Continuous carbon nanotube reinforced composites. *Nano Letters*. 2008;8(9):2762-6.

- [122] Kim SY, Tanimoto T, Uchino K, Nam CH, Nam S, Lee WI. Effects of PZT particle-enhanced ply interfaces on the vibration damping behavior of CFRP composites. *Composites Part a-Applied Science and Manufacturing*. 2011;42(10):1477-82.
- [123] Tanimoto T. A new vibration damping CFRP material with interlayers of dispersed piezoelectric ceramic particles. *Composites Science and Technology*. 2007;67(2):213-21.
- [124] Dutra RCL, Soares BG, Campos EA, Silva JLG. Hybrid composites based on polypropylene and carbon fiber and epoxy matrix. *Polymer*. 2000;41(10):3841-9.
- [125] Zhou X, Shin E, Wang KW, Bakis CE. Interfacial Damping Characteristics of Carbon Nanotube Based Composites. *Compos Sci Technol*. 2004;64(15):2425-37.
- [126] Suhr J, Zhang W, Ajayan PM, Koratkar NA. Temperature-activated interfacial friction damping in carbon nanotube polymer composites. *Nano Letters*. 2006;6(2):219-23.
- [127] Auad ML, Mosiewicki MA, Uzunpinar C, Williams RJJ. Single-wall carbon nanotubes/epoxy elastomers exhibiting high damping capacity in an extended temperature range. *Composites Science and Technology*. 2009;69(7-8):1088-92.
- [128] Rajoria H, Jalili N. Passive vibration damping enhancement using carbon nanotube-epoxy reinforced composites. *Composites Science and Technology*. 2005;65(14):2079-93.
- [129] Buldum A, Lu JP. Atomic scale sliding and rolling of carbon nanotubes. *Physical Review Letters*. 1999;83(24):5050-3.
- [130] Yap H, Lakes R, Carpick R. Negative stiffness and enhanced damping of individual multiwalled carbon nanotubes. *Physical Review B*. 2008;77(4):045423-7.
- [131] Qian H, Bismarck A, Greenhalgh ES, Shaffer MSP. Carbon nanotube grafted carbon fibres: A study of wetting and fibre fragmentation. *Composites Part a-Applied Science and Manufacturing*. 2010;41(9):1107-14.
- [132] Menard KP. *Dynamic Mechanical Analysis: A Practical Introduction*. Boca Raton, Florida CRC Press LLC; 2000.
- [133] Melo JDD, Radford DW. Viscoelastic characterization of transversely isotropic composite laminae. *Journal of Composite Materials*. 2003;37(2):129-45.
- [134] LS-DYNA Theoretical Manual, version 950, Livermore Software Tech. Corp., March 2006.
- [135] Cheeseman BA, Bogetti TA. Ballistic impact into fabric and compliant composite laminates. *Composite Structures*. 2003;61(1-2):161-73.
- [136] Morozov EV, Sylantiev SA, Evseev EG. Impact damage tolerance of laminated composite helicopter blades. *Composite Structures*. 2003;62(3-4):367-71.

- [137] Batra RC, Hassan NM. Blast resistance of unidirectional fiber reinforced composites. *Composites Part B: Engineering*. 2008;39(3):513-36.
- [138] Donadona MV, Lannuccib L, Falzonb BG, Hodgkinsonb JM, deAlmeidaa SF. A progressive failure model for composite laminates subjected to low velocity impact damage. *Computers & Structures*. 2008;86,(11-12):1232-52.
- [139] Riccio A, Tessitore N. Influence of loading conditions on the impact damage resistance of composite panels. *Computers & Structures*. 2005;83(28-30):2306-17.
- [140] Yen CF. Ballistic Impact Modeling of Composite Materials 7th International LS-DYNA Users Conference; p. 6.15-6.26.
- [141] Xiao JR, Gama BA, Gillespie JW, Jr. Progressive damage and delamination in plain weave S-2 glass/SC-15 composites under quasi-static punch-shear loading. *Composite Structures*. 2007;78(2):182-96.
- [142] Deka LJ, Bartus SD, Vaidya UK. Multi-site impact response of S2-glass/epoxy composite laminates. *Composites Science and Technology*. 2009;69(6):725-35.
- [143] Kim KJ, Yang DY, Yoon JW. Microstructural evolution and its effect on mechanical properties of commercially pure aluminum deformed by ECAE (Equal Channel Angular Extrusion) via routes A and C. *Materials Science and Engineering a-Structural Materials Properties Microstructure and Processing*. 2010;527(29-30):7927-30.
- [144] Hashin Z. Failure Criteria for Unidirectional Fiber Composites. *Journal of Applied Mechanics-Transactions of the Asme*. 1980;47(2):329-34.
- [145] Matzenmiller A, Lubliner J, Taylor RL. A constitutive model for anisotropic damage in fiber-composites. *Mechanics of Materials*. 1995;20(2):125-52.
- [146] Schulz RB, Plantz VC, Brush DR. Shielding theory and practice. *IEEE Trans On Electromagnetic Compatibility*. 1998;30(3).
- [147] Bridges E, Miller DA, Schulz RB. Comparison of shielding calculations. *IEEE Transactions on Electromagnetic Compatibility*. 1968;10 (1).
- [148] Chung DDL. Materials for electromagnetic interference shielding. *J Mater Eng Perform*. 2000;9(3):350-4.
- [149] Pande S, Singh B, Mathur R, Dhama T, Saini P, Dhawan S. Improved Electromagnetic Interference Shielding Properties of MWCNT-PMMA Composites Using Layered Structures. *Nanoscale research letters*. 2009;4(4):327-34.
- [150] Yasufuku S. Technical progress of EMI Shielding Materials in Japan. *EEE Electrical Insulation Magazine*. 1990;16(6).
- [151] Colaneri NF, Shacklette LW. EMI Shielding Measurements of Conductive Polymer Blends. *Ieee Transactions on Instrumentation and Measurement*. 1992;41(2):291-7.

- [152] Joo J, Oblakowski Z, Du G, Pouget JP, Oh EJ, Wiesinger JM, et al. Microwave Dielectric Response of Mesoscopic Metallic Regions and the Intrinsic Metallic State of Polyaniline. *Physical Review B*. 1994;49(4):2977-80.
- [153] Shinagawa S, Kumagai Y, Urabe K. Conductive papers containing metallized polyester fibers for electromagnetic interference shielding. *Journal of Porous Materials*. 1999;6(3):185-90.
- [154] Huang CJ, Chang TC. Studies on the electromagnetic interference shielding effectiveness of metallized PVAc-AgNO₃/PET conductive films. *Journal of Applied Polymer Science*. 2004;91(1):270-3.
- [155] Manners I. Materials science - Putting metals into polymers. *Science*. 2001;294(5547):1664-6.
- [156] Luo XC, Chung DDL. Electromagnetic interference shielding using continuous carbon-fiber carbon-matrix and polymer-matrix composites. *Composites Part B-Engineering*. 1999;30(3):227-31.
- [157] Das NC, Chaki TK, Khastgir D, Chakraborty A. Electromagnetic interference shielding effectiveness of conductive carbon black and carbon fiber-filled composites based on rubber and rubber blends. *Advances in Polymer Technology*. 2001;20(3):226-36.
- [158] Park SH, Thielemann P, Asbeck P, Bandaru PR. Enhanced dielectric constants and shielding effectiveness of, uniformly dispersed, functionalized carbon nanotube composites. *Applied Physics Letters*. 2009;94(24).
- [159] Kim HM, Kim K, Lee CY, Joo J, Cho SJ, Yoon HS, et al. Electrical conductivity and electromagnetic interference shielding of multiwalled carbon nanotube composites containing Fe catalyst. *Applied Physics Letters*. 2004;84(4):589-91.
- [160] Li N, Huang Y, Du F, He X, Lin X, Gao H, et al. Electromagnetic Interference (EMI) Shielding of Single-Walled Carbon Nanotube Epoxy Composites. *Nano Letters*. 2006;6(6).
- [161] Lee BO, Woo WJ, Kim MS. EMI Shielding Effectiveness of Carbon Nanofiber Filled Poly (vinyl alcohol) Coating Materials. *Macromol Mater Eng*. 2001;286.
- [162] Lee BO, Woo WJ, Park HS, Hahm HS, Wu JP, Kim MS. Influence of aspect ratio and skin effect on EMI shielding of coating materials fabricated with carbon nanofiber/PVDF. *Journal of Materials Science*. 2002;37(9):1839-43.
- [163] Chen XQ, Saito T, Kusunoki M, Motojima S. Three-dimensional vapor growth mechanism of carbon microcoils. *Journal of Materials Research*. 1999;14(11):4329-36.
- [164] Zinck P, Mader E, Gerard JF. Role of silane coupling agent and polymeric film former for tailoring glass fiber sizings from tensile strength measurements. *Journal of Materials Science*. 2001;36(21):5245-52.

- [165] Ellyin F, Maser R. Environmental effects on the mechanical properties of glass-fiber epoxy composite tubular specimens. *Compos Sci Technol*. 2004;64(12):1863-74.
- [166] Ma P-C, Siddiqui NA, Marom G, Kim J-K. Dispersion and functionalization of carbon nanotubes for polymer-based nanocomposites: A review. *Composites Part A: Applied Science and Manufacturing*. 2010;41(10):1345-67.
- [167] Green KJ, Dean DR, Vaidya UK, Nyairo E. Multiscale fiber reinforced composites based on a carbon nanofiber/epoxy nanophased polymer matrix: Synthesis, mechanical, and thermomechanical behavior. *Composites Part A: Applied Science and Manufacturing*. 2009;40(9):1470-5.
- [168] Choi ES, Brooks JS, Eaton DL, Al-Haik MS, Hussaini MY, Garmestani H, et al. Enhancement of thermal and electrical properties of carbon nanotube polymer composites by magnetic field processing. *Journal of Applied Physics*. 2003;94(9):6034-9.